



universität
wien

Masterarbeit

Numerical Simulations of Hyperfine Transitions in Antihydrogen

verfasst von

Bernadette Kolbinger, BSc

angestrebter akademischer Grad

Master of Science (MSc)

Wien, 2014

Studienkennzahl lt. Studienblatt: A 066 876
Studienrichtung lt. Studienblatt: Masterstudium Physik
Betreut von: Prof. Dr. Eberhard Widmann

Zusammenfassung

Im Standardmodell der Teilchenphysik gilt die CPT Symmetrie als fundamental. Um diese Annahme zu testen, verwirklicht die ASACUSA (Atomic Spectroscopy And Collisions Using Slow Antiprotons) Collaboration ein Rabi ähnliches Experiment um die Hyperfeinstruktur von Antiwasserstoff im Grundzustand mit hoher Präzision zu messen. Der Vergleich der Übergangsfrequenzen von Wasserstoff und Antiwasserstoff erlaubt einen direkten Test des CPT theorems im Rahmen der Standardmodellerweiterung.

Das Spektrometer ist aus einer Quelle, einer Mikrowellen Kavität, einem Sextupol Magneten und einem Detektor aufgebaut.

In dieser Arbeit wird die Implementation und Ergebnisse der numerischen Simulation von Hyperfeinübergängen von Antiwasserstoff/Wasserstoff im Grundzustand präsentiert und diskutiert.

Der Einfluss von Temperatur und Verteilung des Teilchenstrahls, Inhomogenitäten des statisches Magnetfelds in der Kavität, Leistung der Kavität und Teilchenzahl auf die Resonanzspektra wird untersucht. Methoden zur Bestimmung der Übergangsfrequenz bei Abwesenheit eines magnetisches Felds werden diskutiert und verglichen.

Abstract

In order to test CPT symmetry which, by the standard model of particle physics, is considered to be an invariant the ASACUSA (Atomic Spectroscopy And Collisions Using Slow Antiprotons) collaboration realizes a Rabi like experiment to measure the hyperfine splitting of antihydrogen in the ground state with very high precision. Comparing the transition frequencies of hydrogen and antihydrogen allows a direct test of CPT within the framework of the Standard Model Extension.

The ASACUSA spectrometer line is built up of a source, a spin flip inducing microwave cavity, a spin analyzing sextupole magnet and a detector.

In this thesis, implementation and results of numerical simulation of hyperfine transitions of antihydrogen/hydrogen in the groundstate within the ASACUSA setup are presented and discussed.

Effects of beam temperature und distribution, inhomogeneities of the static magnetic field inside the cavity, cavity power and partice statistics have been studied. Methods of obtaining the transition frequency at zero magnetic field have been discussed and compared.

Contents

| | | |
|----------|---|-----------|
| 1 | Introduction | 1 |
| 2 | Theoretical Background | 2 |
| 2.1 | Hyperfine Structure of Hydrogen | 2 |
| 2.2 | Limits of the Standard Model | 3 |
| 2.3 | CPT Symmetry | 4 |
| 2.4 | The Standard Model Extension | 5 |
| 2.4.1 | Antihydrogen Spectroscopy and the Standard Model Extension | 6 |
| 3 | Experimental Setup | 10 |
| 3.1 | The Rabi Experiment | 10 |
| 3.2 | Hyperfine Spectroscopy of Antihydrogen | 11 |
| 3.2.1 | The Production of Antihydrogen | 12 |
| 3.2.2 | The Spin-flip Cavity and the Spin Analyzing Sextupole Magnet | 14 |
| 3.2.3 | The Antihydrogen Detector | 17 |
| 4 | Simulation of the GSHFS Transitions of H/$\bar{\text{H}}$ | 19 |
| 4.1 | Introduction - Interaction of atoms with a magnetic field . . . | 19 |
| 4.1.1 | The Two Level Atom | 20 |
| 4.1.2 | Density matrices | 22 |
| 4.2 | Solving the optical Bloch equations numerically | 23 |
| 4.3 | Geometry and Setup Implementation | 26 |
| 4.4 | Implementation of the Magnetic Fields | 32 |
| 4.4.1 | The Oscillating Magnetic Field | 32 |
| 4.4.2 | The Static Magnetic Field | 37 |
| 4.5 | Simulation Results | 39 |
| 4.5.1 | Fitting the Scans | 39 |
| 4.5.2 | Dependence on Beam Temperature | 40 |
| 4.5.3 | Dependence on Cavity Power | 47 |

Contents

| | | |
|----------|--|-----------|
| 4.5.4 | Dependence on Inhomogeneity of the Static Magnetic Field | 51 |
| 4.5.5 | Dependence on Statistics | 58 |
| 4.5.6 | Transition Frequency at Zero Magnetic Field | 68 |
| 5 | Summary and Outlook | 74 |
| 6 | Appendix | 76 |
| 6.1 | Fit Results: Dependence on Temperature | 76 |
| 6.2 | Fit Results: Dependence on Cavity Power | 80 |
| 6.3 | Fit Results: Dependence on Inhomogeneity | 81 |
| 6.4 | Fit Results: Dependence on Statistics | 83 |
| 6.5 | Fit Results: Extrapolation to Zero Field | 87 |

1 Introduction

Several grand milestones in physics are historically connected to studies of the hydrogen atom - as the simplest of all atoms, it has played an important role in testing theories and understanding atomic structure.

The discovery of the spectral lines of hydrogen lead to Bohr's model, giving a first rough description. Later, with gained experimental resolution, the fine structure of hydrogen was discovered and explained by Dirac's theory [1][2] resulting in his famous equation describing free spin 1/2 particles:

$$\left(i\gamma^\mu \frac{\partial}{\partial x_\mu} - m\right)\psi = 0 \quad (1.1)$$

where x denotes the four vector of space and time, γ the Dirac matrices, m the mass of the particle and ψ a spinor wave function. Although his equation contains two kind of solutions - ones with positive energies and the others with negative energy which at first glance seemed to be a flaw at that time.

But this lead to the idea of antimatter which was first experimentally detected in cosmic rays by Anderson in 1932.

Also, after experiments by Rabi, Lamb etc. a discrepancy to Dirac's theory was found - the experimentally determined hyperfine structure in the ground state differed from that predicted by theory.

An attempt to solve this contradiction ended up in the development of the renormalization method and Feynman diagrams which are now vital in particle physics [3]. With this, also the Lamb shift and the anomaly of the magnetic moment of the electron could be described.

The necessity for physics beyond the standard model grew with time and discoveries which cannot be explained by the standard model were made like neutrino oscillations, dark matter, dark energy and of course the cosmological asymmetry of matter and antimatter.

The hydrogen atom is one of the best known systems in physics. The first creation of antihydrogen in 1996 [4] and its later production in quantity in 2002 [5] strongly suggested to compare the properties of these two atoms - what could be better suited to help solve the important questions left unanswered by the standard model than good old hydrogen and his antimatter brother?

2 Theoretical Background

2.1 Hyperfine Structure of Hydrogen

The hyperfine structure of the spectral lines is a result of the coupling of \vec{J} , the total angular momentum of the electron, and the total angular momentum of the proton \vec{I} to the total angular momentum of the system: $\vec{F} = \vec{J} + \vec{I}$. In case of the 1s groundstate of hydrogen, the interaction between the proton and electron spin leads to a singlet state with $F = 0$ and a triplet state with $F = 1$ and $M = -1, 0, 1$, see figure 2.1.

Without an external magnetic field, the transition frequency between these two levels is [6][7]:

$$\nu_{HF} = 1420405751.7667 \pm 0.0009 \text{ Hz} \quad (2.1)$$

which is one of the most accurately measured quantities .

In a magnetic field however, the degenerated $F = 1$ level splits up, see figure 2.2, and the energies of all four states shift. Therefore, in the presence of an external magnetic field not only one but several transitions can be observed in the hydrogen atom.

Regarding their behaviour in an inhomogeneous magnetic field, these states can be classified into low- and high-field seeking states (LFS and HFS).

The energy of the atom in a B-field shifts according to $\Delta E = -\vec{\mu}\vec{B}$ and the magnetic moment will align parallel ((F,M_F) = (1,1) and (0,0)) or antiparallel ((F,M_F) = (1,-1) and (1,0)) to the B-field. If now a field gradient is added,

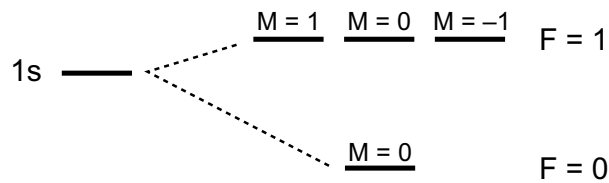


Figure 2.1: The splitting of the 1s level of hydrogen due to the electron and proton spin interaction.

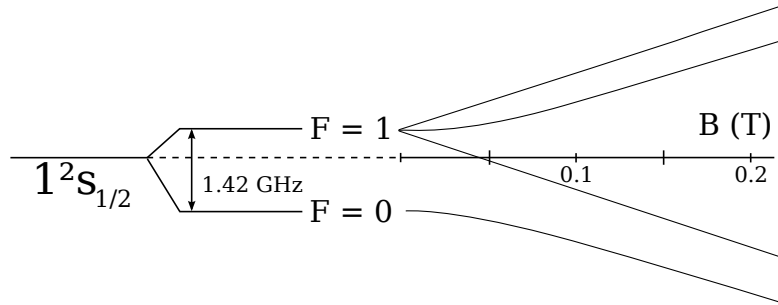


Figure 2.2: Hyperfine splitting and Breit-Rabi diagram. Splitting of the hyperfine niveaus in an external magnetic field.

| | LFS states | HFS states |
|------------------|---------------|---------------|
| H | (1,1), (1,0) | (1,-1), (0,0) |
| $\bar{\text{H}}$ | (1,-1), (1,0) | (1,1), (0,0) |

Table 2.1: Overview of low field seeking and high field seeking states in hydrogen and antihydrogen.

the atoms with parallel magnetic moment will tend to move toward higher field regions where they will have lower energies. For the states $(F, M_F) = (1, -1)$ and $(1, 0)$ the opposite is true.

Note, that the order of levels is different for hydrogen and antihydrogen. An overview is given in table 2.1.

2.2 Limits of the Standard Model

Particles and their interactions are well described by the standard model - but only at the currently accessible energy scales i.e. starting at the electroweak scale m_W and being small compared to the Planck mass $M_P (= \sqrt{\hbar c/G} \simeq 10^{19}$ GeV) [8]. At energies in the order of M_P though, the standard model is no

longer able to describe nature properly since gravity is not included [9].

In this energy region, the standard model is expected to be superseded by a more fundamental theory that connects quantum theory and gravitation consistently [10].

Accelerators of today cannot reach the Planck scale - but low energy manifestations of this underlying theory may exist which are suppressed at 'common' energies.

Though these effects will be very small due to the energy difference between the low energy scale and the Planck scale and only high precision experiments might be able to detect them [9][10].

One of these manifestations of the underlying theory might be the violation of the CPT symmetry, a fundamental symmetry embedded in the standard model.

2.3 CPT Symmetry

The CPT theorem states that the discrete symmetry of CPT (**C**harge, **P**arity and **T**ime) is an exact symmetry i.e. an invariance for all local quantum field theories with Lorentz symmetry assuming pointlike particles e.g. the standard model or quantum electrodynamics (QED).

It predicts that the properties of particles and antiparticles must be identical (mass, lifetime) or equal but opposite (charge and magnetic moment). Therefore, the CPT theorem also says that atoms and their antiparticles have the same characteristic spectrum. If any difference would be found experimentally, this would hint at effects coming from beyond the standard model [11].

Since the hyperfine transition frequency of hydrogen is one of the best known properties of matter - up to a precision of 10^{-12} [12] - a possible experiment to test CPT symmetry is the hyperfine spectroscopy of antihydrogen with precision equal to that in the hydrogen case.

A summary of precisions from different experiments testing CPT using particle antiparticle comparison is shown in figure 2.4. Currently, the test with the highest relative precision is the K/\bar{K} mass measurement with a relative precision $\Delta m/m \approx 10^{-18}$ which corresponds to an absolute precision of 10^5 Hz.

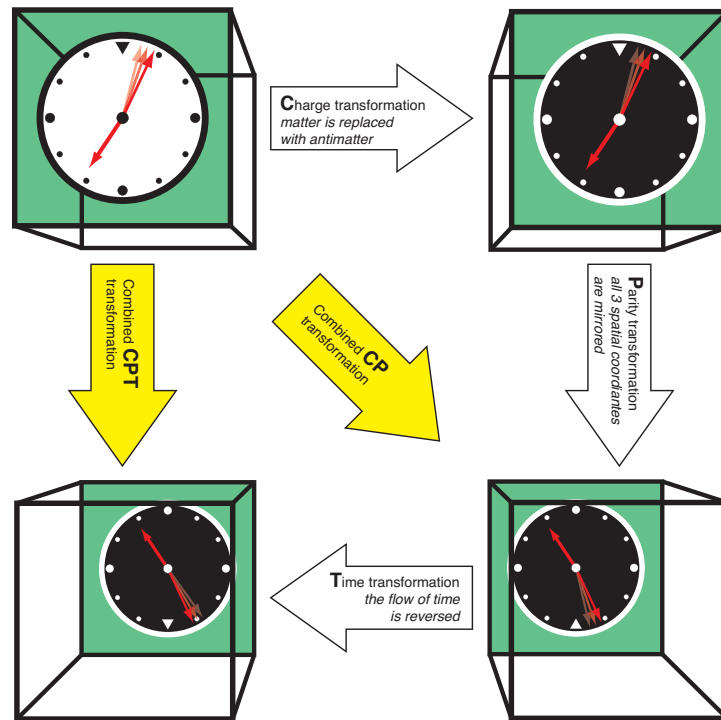


Figure 2.3: Illustration of C, P, T, CP and CPT symmetry (picture by Bertalan Juhasz).

A relative accuracy of the measurement of the antihydrogen groundstate hyperfine splitting frequency (\bar{H} GS-HFS) of 10^{-4} could already compete with the Kaon test, since its absolute precision would be $1 \text{ GHz} \times 10^{-4} = 10^5 \text{ Hz}$.

In order to make cross comparisons of the CPT tests which measure different quantities easier, it is beneficial to use a common theoretical framework [14].

One of them is the Extension of the Standard Model (SME) which will be discussed in the next section.

2.4 The Standard Model Extension

Since Lorentz and CPT symmetry are embedded in the standard model, no predictions can be made by this model on how breaking of these symmetries might take place [15].

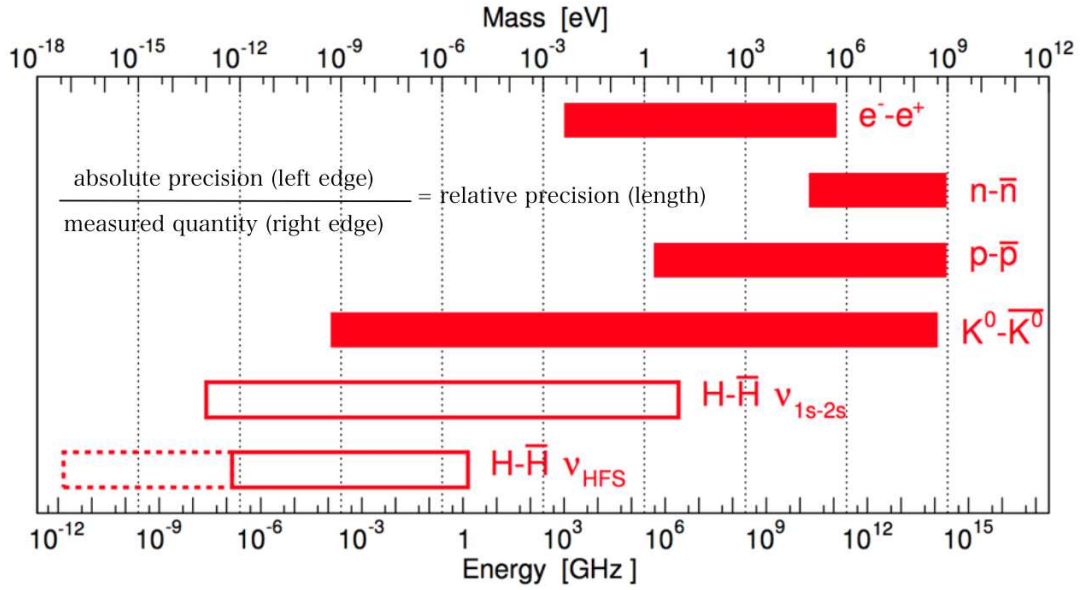


Figure 2.4: Summary of relative (length of the red bars) and absolute (left edge of the bar) precisions of different CPT symmetry testing experiments. The dotted line of the $H-\bar{H} \nu_{HFS}$ bar symbolizes the precision possible for the maser. (picture adapted from [13])

However, Don Colladay and Alan Kostelecký have developed an Extension of the Standard Model [16] which is a more general and fundamental model and combines the standard model and general relativity. It allows microscopic CPT and Lorentz symmetry violating effects and is compatible with established quantum field theory and also experimental constraints.

2.4.1 Antihydrogen Spectroscopy and the Standard Model Extension

Taking a look at free H/\bar{H} , according to the SME additional terms due to symmetry violation appear in the Lagrangian and therefore to a modified Dirac equation [10]:

$$(i\gamma^\mu D_\mu - m_e - a_\mu^e \gamma^\mu - b_\mu^e \gamma_5 \gamma^\mu - \frac{1}{2} H_{\mu\nu}^e \sigma^{\mu\nu} + i c_{\mu\nu}^e \gamma^\mu D^\nu + i d_{\mu\nu}^e \gamma_5 \gamma^\mu D^\nu) \psi = 0 \quad (2.2)$$

here ψ is a four-component electron field describing an electron with mass m_e , the Dirac matrices γ , $iD_\mu \equiv i\partial_\mu - qA_\mu$ with the electromagnetic four potential $A^\mu = (|e|/4\pi r, 0)$. All in units of $\hbar = c = 1$.

Lorentz symmetry breaking is incorporated by a set of coefficients - terms with a_μ^e and b_μ^e also violate CPT, whereas $H_{\mu\nu}^e$, $c_{\mu\nu}^e$ and $d_{\mu\nu}^e$ conserve CPT.

This coefficients are expected to be small and need to be determined or constrained by experiments.

In order to study the effects of the Standard Model Extension on free H and \bar{H} spectra, perturbation theory in relativistic quantum mechanics is used [10]. This is justified because of the assumed small size of the coupling coefficients.

The unperturbated H and \bar{H} Hamiltonians are identical, so are all perturbative terms which appear due to conventional QFT calculations. Therefore, their eigenenergies and spectra are identical as well.

Though including the Lorentz and CPT symmetry breaking coefficients of the SME, a calculation of the spectra of hydrogen and antihydrogen leads to energy shifts of their levels.

For the 1s and the 2s levels of hydrogen, the perturbative result for the energy corrections for a basis state $|m_J, m_I\rangle$ is [10]:

$$\Delta E^H(m_J, m_I) = a_0^e + a_0^p - c_{00} m_e - c_{00}^p m_p \quad (2.3)$$

$$+ (-b_3^e + d_{30}^e m_e + H_{12}^e) \frac{m_J}{|m_J|} \quad (2.4)$$

$$+ (-b_3^p + d_{30}^p m_p + H_{12}^p) \frac{m_I}{|m_I|} \quad (2.5)$$

where m_p is the proton/antiproton mass, m_e the electron/positron mass and m_J and m_I the projections of the angular momenta \vec{J} and \vec{I} on the z-axis. In the case of antihydrogen, a , d and H reverse sign.

For the hyperfine levels of hydrogen, the SME gives the following results for the energy shifts [10][9]:

$$\Delta E_{(1,1)}^H = -b_3^e - b_3^p + d_{30}^e m_e + d_{30}^p m_p + H_{12}^e + H_{12}^p \quad (2.6)$$

$$\Delta E_{(1,0)}^H = -\cos 2\theta(b_3^e - b_3^p - d_{30}^e m_e + d_{30}^p m_p - H_{12}^e + H_{12}^p) \quad (2.7)$$

$$\Delta E_{(1,-1)}^H = -\Delta E_{(1,1)}^H \quad (2.8)$$

$$\Delta E_{(0,0)}^H = -\Delta E_{(1,0)}^H \quad (2.9)$$

where (1,1), (1,0) etc. denote the different states (F,M) and $\cos \theta$ is the spin mixing parameter of the (0,0) and (1,0) states and depends on the principal quantum number and the B field.

Measuring the hyperfine transition frequency of antihydrogen and hydrogen provides a direct test of CPT symmetry since the energies are directly connected to the CPT violating coefficients.

Note, that the coefficients in the SME Lagrangian have the dimension of energy, therefore one has to compare absolute values of energies and not relative ones as it is done in the neutral Kaon system.

If the atoms move in an external magnetic field, the hyperfine niveaus will split up according to the Breit-Rabi formula [17]:

$$E_{(1,1)} = \frac{1}{4}E_0 - \frac{1}{2}(g_J + g_I)\mu_B B + \Delta E_{(1,1)} \quad (2.10)$$

$$E_{(1,0)} = -\frac{1}{4}E_0 + \frac{1}{2}E_0\sqrt{1+x^2} + \Delta E_{(1,0)} \quad (2.11)$$

$$E_{(1,-1)} = \frac{1}{4}E_0 - \frac{1}{2}(g_J + g_I)\mu_B B - \Delta E_{(1,1)} \quad (2.12)$$

$$E_{(0,0)} = -\frac{1}{4}E_0 - \frac{1}{2}E_0\sqrt{1+x^2} - \Delta E_{(1,0)} \quad (2.13)$$

where $x = B/B_0$ and $B_0 = 2\pi\nu_{HF}/((g_J - g_I)\mu_B)$ with $g_J = -2.0023193043718$ [18] and $g_I = 0.003042064412$ [18] (both in units of μ_B).

Taking a closer look at equation 2.6 etc. reveals that if we set the spin mixing parameter to zero which corresponds to zero B-field, then we can see that the energy shifts of the states (1,1) and (1,-1) do not vanish and are equal in amount but opposite in sign - so the $F = 1$ degeneracy is lifted [9], see figure 2.5.

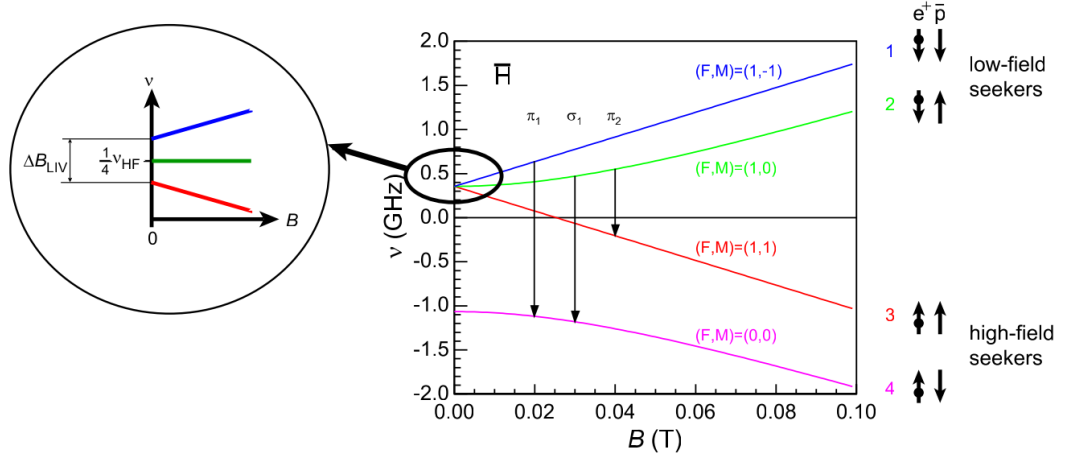


Figure 2.5: *Right*: Breit-Rabi diagram [19]. Splitting of the hyperfine niveaus in an external magnetic field, alignment in high fields of the spins of e^+ and \bar{p} and suitable transitions between the levels for a spin state analyzing experiment. *Left*: Lifted degeneracy of the $F = 1$ hyperfine level according to the SME.

So in this scenario CPT symmetry breaking would arise as anomlies in the hyperfine niveaus of the system while studying the spin states of the atoms of the beam. Using the different behaviour of low- and high-field seekers in an inhomogenous magnetic field, one can differentiate between the states after inducing a spin-flip from a LFS to a HFS state and vice versa. The following transitions are suitable for detecting hyperfine structure anomalies [19]:

$$\sigma_1 : (1, 0) \rightarrow (0, 0) : \quad \nu_{\sigma_1} = \nu_0 \sqrt{1 + x^2} + \frac{2\Delta E_{(1,0)}}{h} \quad (2.14)$$

$$\pi_1 : (1, -1) \rightarrow (0, 0) : \quad \nu_{\pi_1} = \frac{1}{2}\nu_0 - \frac{1}{2}(g_J + g_I)\mu_B B/h + \frac{1}{2}\nu_0 \sqrt{1 + x^2} + \frac{\Delta E_{(1,1)} + \Delta E_{(1,0)}}{h} \quad (2.15)$$

$$\pi_2 : (1, 0) \rightarrow (1, 1) : \quad \nu_{\pi_2} = \frac{1}{2}\nu_0(\sqrt{1 + x^2} - 1) - \frac{1}{2}(g_J + g_I)\mu_B B/h + \frac{\Delta E_{(1,0)} - \Delta E_{(1,1)}}{h} \quad (2.16)$$

3 Experimental Setup

3.1 The Rabi Experiment

The ASACUSA experiment to determine the hyperfine structure of antihydrogen is based on an experiment first proposed in 1938 by I. Rabi which was the first application of the magnetic resonance principle. The setup of this experiment can be seen in figure 3.1.

The atomic beam passes through an inhomogeneous magnetic field region where one spin state will be selected - this behaviour was already discovered by O. Stern and W. Gerlach in 1922 [21].

Afterwards, the beam will pass a region with a radio frequency field superimposed with a homogeneous field.

Depending on the frequency of the oscillating field, the beam is then either focused by a second inhomogeneous field region or deflected if the oscillating field had induced a spin flip. With the molecular beam magnetic resonance technique, the frequency of the oscillating field is kept constant while the strength of the superimposed homogeneous magnetic field is varied. Monitoring the counts at the detector allows to measure the transition frequencies with high precision.

For a π pulse we get for a single velocity beam a single line with a full width

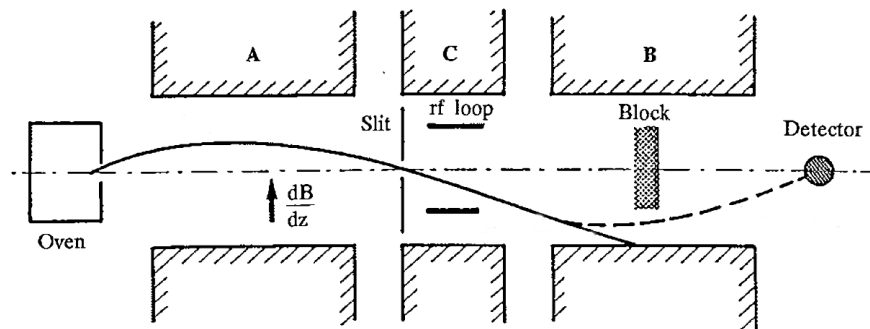


Figure 3.1: Setup of the Rabi experiment [20].

at half maximum (FWHM) [22]:

$$f = \frac{0.799}{T} \quad (3.1)$$

with the time T the particle spent in the RF-field. For a beam with a Maxwell-Boltzmann distributed velocity, we get a FWHM f of [22]:

$$f = 1.073 \frac{v_m}{L} \quad (3.2)$$

with L being the length of the path the particle flies through the oscillating field region and v_m being the most probable velocity of the Maxwell-Boltzmann distribution.

In the cavity used for the ASACUSA experiment the resonance spectra will not be a single peak, but have a double peak structure due to the field distribution of the microwave field, see for example figure 3.6. Since the standing wave inside the cavity is a superposition of a wave traveling in beam direction and a wave moving backwards, the structure of the spectrum can also be thought of as a Doppler splitting [23]. Hence, the peak splitting is proportional to the velocity of the particles in the beam. A table with calculated FWHM for both the monovelocity and the Maxwell-Boltzmann distributed velocity beam as well as FWHM and peak separation of the simulated spectra can be found in the Appendix.

3.2 Hyperfine Spectroscopy of Antihydrogen

One of the goals of the ASACUSA collaboration (**A**tomic **S**pectroscopy **A**nd **C**ollisions **U**sing **S**low **A**ntiprotons) is to test the CPT symmetry by measuring the ground-state hyperfine structure of antihydrogen using a Rabi-like experimental setup. A sketch of the spectrometer line can be seen in figure 3.2. In principle, the experiment is composed of four stages:

1. the production of antihydrogen using a so-called CUSP trap,
2. the induction of hyperfine transitions using a microwave cavity,
3. the analysis of spins using a sextupole magnet

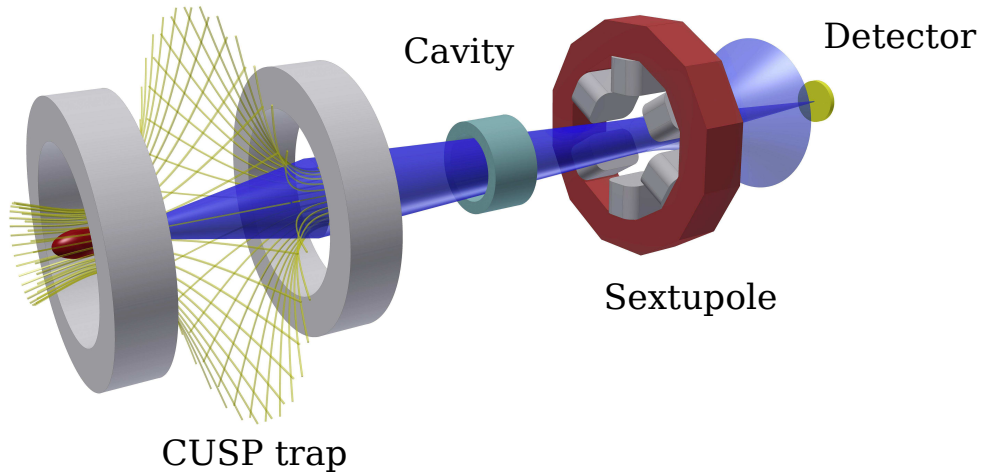


Figure 3.2: Schematic drawing of the experimental setup.

4. and the detection of antihydrogen.

In the following, the different parts of the experiment will be discussed.

3.2.1 The Production of Antihydrogen

Antiprotons \bar{p} and positrons e^+ which are the constituents of antihydrogen are first collected in Penning traps before injected into the CUSP trap where the mixing takes place.

The \bar{p} are produced at the PS (**P**roton **S**ynchrotron) at CERN where a proton beam is shot at an iridium target and the reaction $p + p \rightarrow p + p + p + \bar{p}$ takes place.

The antiprotons are slowed down by the AD (**A**ntiproton **D**ecelerator) to ≈ 5.4 MeV and, after leaving the ring, further decelerated by the RQFD (**R**adio **F**requency **Q**uadrupole **D**ecelerator) to approximately 115 keV [24].

Then they are accumulated in the Musashi trap. The positrons are provided by a ^{22}Na source via β^+ -decay and collected in a Penning trap.

The synthesis of a spin-polarized antihydrogen beam takes place in the so-called CUSP trap. It consists of a pair of superconducting Anti-Helmholtz coils and multi-ring electrodes (MRE) (stack of electrodes) [25]. The magnetic

3 Experimental Setup

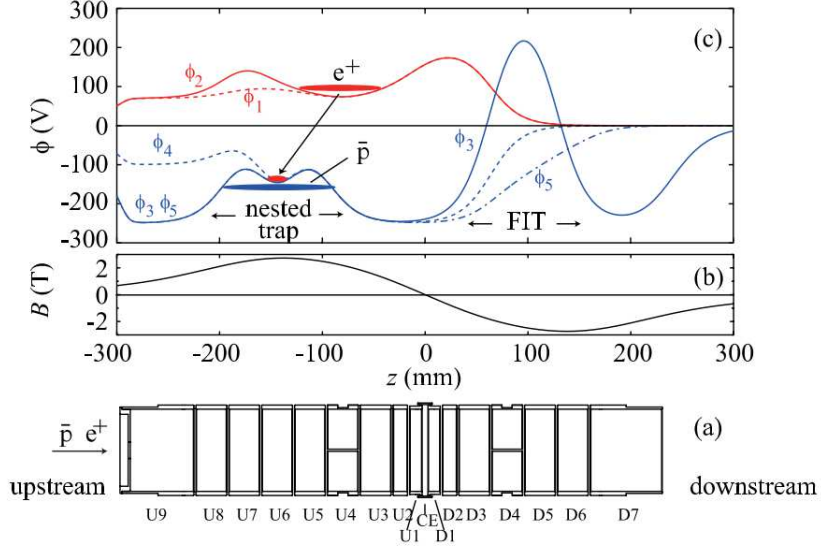


Figure 3.3: Potentials, magnetic field and MRE of the cusp trap [25].

field and the different potentials produced by the MRE, which are necessary to produce antihydrogen, are shown in figure 3.3.

The positrons are injected into the MRE providing the potential ϕ_1 . Directly afterwards, the field configuration is changed to ϕ_2 to keep the positrons trapped inside the CUSP. They are cooled and compressed while the potential is slowly changed to the nested trap potential ϕ_3 . Then, using the configuration ϕ_4 , the antiprotons are injected and the potential is immediately changed back to ϕ_3 . The positron and antiproton plasma mix and antihydrogen is formed either via radiative or three-body recombination.

Since \bar{H} is neutral, it is not affected by the trapping potential and leaves the MRE field isotropically. Some of the produced \bar{H} are collected in the field ionizing trap (FIT) which can only be passed by antihydrogen atoms in certain quantum states depending on the field strength of the FIT (principal quantum number ≈ 45 [25]), all others are ionized.

The magnetic field of the CUSP trap (see figure 3.3 and 3.2) provided by the Anti-Helmholtz coils is inhomogeneous shaped in a way that high-field seekers will be defocused as they leave the CUSP trap and low field seekers

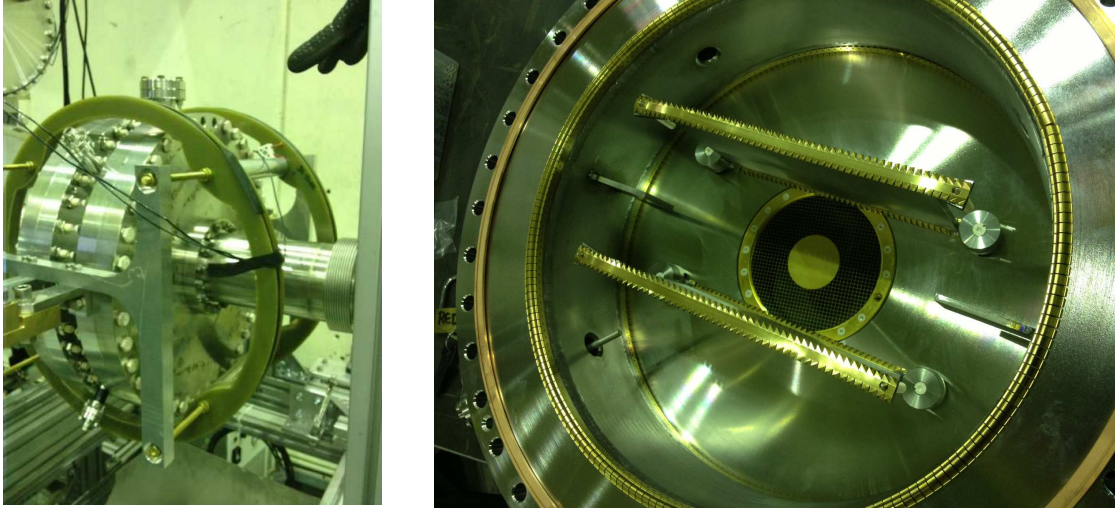


Figure 3.4: *Left*: Cavity with two flanges and the Helmholtz coils (yellow support structure) *Right*: One flange removed so one can see the inside of the cavity with resonator stripline, wings and entrance/exit opening for the beam with mesh and beamstopper.

will be focused. Therefore, a (partially) polarized antihydrogen beam exits the CUSP trap.

3.2.2 The Spin-flip Cavity and the Spin Analyzing Sextupole Magnet

The microwave cavity is shown in figure 3.4. The oscillating magnetic field which induces the spin flips in the atoms is generated by a double stripline resonator which is placed inside a cylindrical vacuum tank.

Figure 3.5 shows the field distribution of the microwave field. One can see that it is very homogeneous in the plane orthogonal to the beam and has a sinusoidal distribution in beam direction - the field is zero at the center of the cavity and has maxima at the front and the back walls. As a consequence of this, the frequency scan of a transition will have a double peak structure - when the frequency of the oscillating field is on resonance, the effects of the

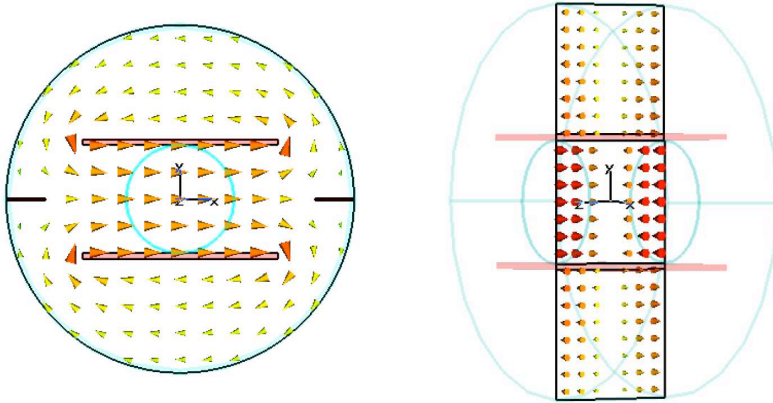


Figure 3.5: Field distribution of the oscillating magnetic field in the x-y plane (left) and the y-z plane (right) [26].

two regions will cancel each other and one gets zero signal on resonance [23]. This can be seen in figure 3.6.

In our cavity, two kinds of transitions are possible - the σ_1 and the π_1 - depending on the angle between the oscillating magnetic field and the static magnetic field provided by Helmholtz coils. For the σ_1 transition, the two B-fields need to be parallel whereas for the π_1 transition they have to be orthogonal to each other.

In the experiment, a small static magnetic field is used. In this case, the transition frequency of σ_1 has a second order dependence on the external field and the π_1 transition is with a linear dependence very sensitive to the homogeneity of the external field [27]. Therefore in order to keep the homogeneity as high as possible, a shielding is used to block stray fields of e.g. the CUSP trap but also the earth magnetic field and perturbations from other experiments.

There are now two possible ways to determine the transition frequency at zero static magnetic field:

1. by measuring the resonance frequency of the σ_1 transition at different external B-fields and then doing an extrapolation to zero field using the Breit-Rabi formula.

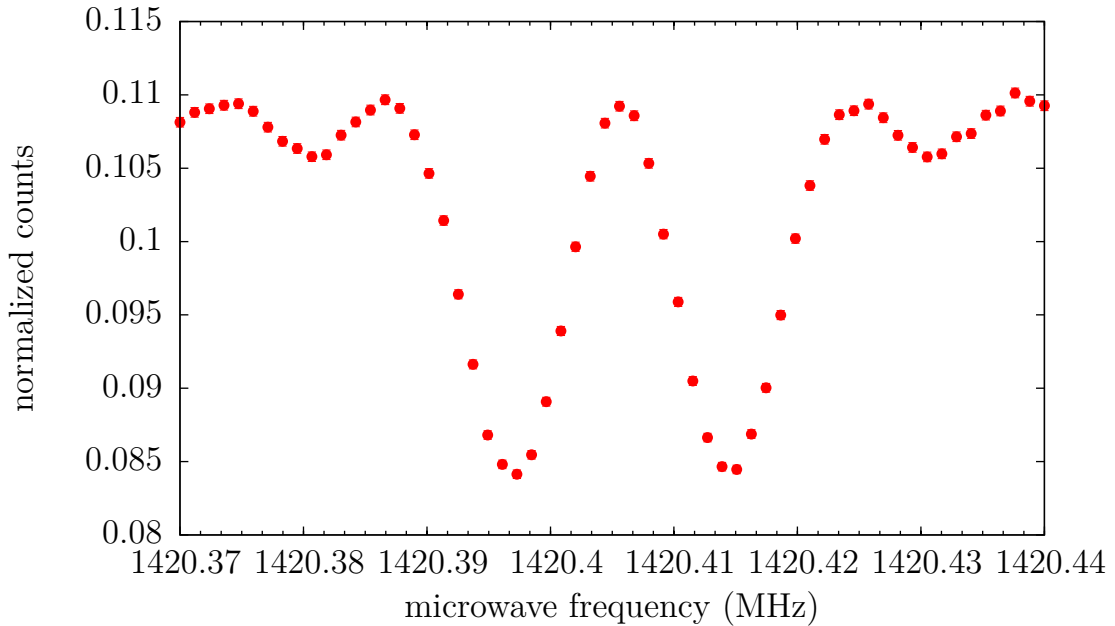


Figure 3.6: Transition at 0 magnetic field using 10^6 monoenergetic (0.01 eV) antihydrogen atoms per scan point, 70% LFS and 30% HFS, y-axis: normalized counts (hits at the detector over number of particles produced at source), x-axis: frequency (MHz). For more informations see chapter 4.3.

2. or by doing a resonance scan for both the σ_1 and π_1 transition and using the transition frequencies and equations 2.14.

For more on this, see chapter 4.5.6. According to simulations, the second method leads to a higher precision (factor of ≈ 1.12 , see chapter 4.5.6) compared to the first possibility, though, a higher homogeneity is required because of the sensitivity of the π_1 transition.

Depending on the choice of method, the alignment of the Helmholtz coils needs to be changed due to the dependence of the angle between the two fields of the transitions. If one chooses scenario two which is favoured since it would lead to a more sensitive CPT test, then an angle of 45° is needed, in order to measure both transitions.

The vacuum chamber of the cavity has two openings to allow the beam to enter and exit. They are covered with meshes in order to close the resonator

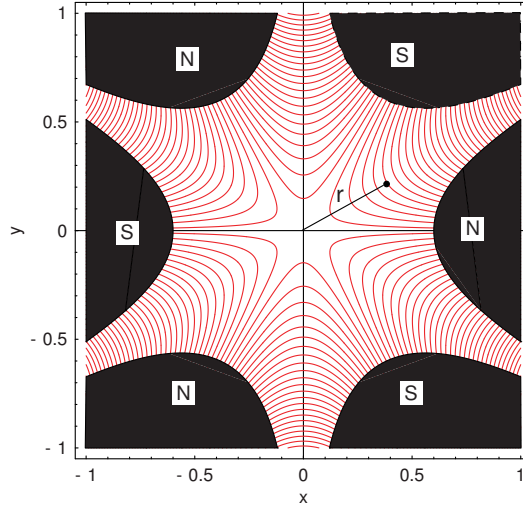


Figure 3.7: Sketch of the x-y cross section of the sextupole magnet, red lines symbolize magnetic field lines. The beam direction is perpendicular to the x-y plane [19].

for the oscillating field and are also equipped with a beam stopper to cut out the middle part of the beam. This is important, since the \vec{H} in the center cannot be analyzed by the sextupole which has zero field in the center (see figure 3.7).

3.2.3 The Antihydrogen Detector

At the end of the spectrometer line a detector is needed in order to monitor events. When detecting antihydrogen, one comes across the following challenge: the production rate is much lower than in hydrogen experiments and lower than the rate of cosmic rays and their electromagnetic showers. Also, upstream annihilations will contribute to the background. So a high antihydrogen detection efficiency is needed.

The detector for the HBAR HFS experiment (called **C**ompact **P**ion **T**racking **D**etector (CPT detector)) will be consisting of a BGO detector and a two layer hodoscope made out of scintillators [24]. In figure 3.8, one can see the detector with only one layer of hodoscope before the upcoming upgrade. When an

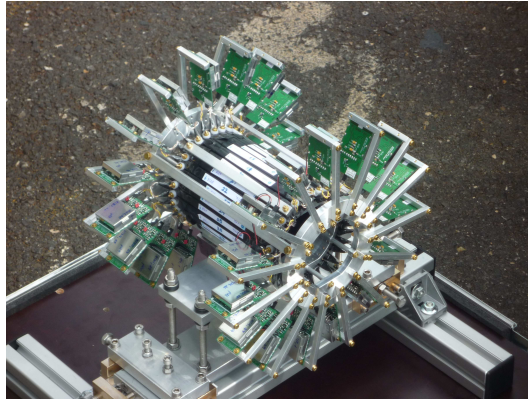


Figure 3.8: The **C**ompact **P**ion **T**racking **D**etector (CPT Detector).

antihydrogen atom collides with the BGO, the annihilation products which are mainly Pions will deposit energy on the BGO and in the hodoscopes. The signal from the scintillator bars of the hodoscope will be converted to an electrical signal by SiPM (**S**ilicon **P**hoto**M**ultiplier) detectors.

The identification of antihydrogen events will be done by studying the tracks in the detector using a Hough analysis as well as information on the energy deposit on the central BGO detector.

4 Simulation of the GSHFS Transitions of H/ $\bar{\text{H}}$

4.1 Introduction - Interaction of atoms with a magnetic field

In order to determine the evolution of the state of the atom with time in a radiation field, one must solve the time-dependent Schrödinger equation:

$$i\hbar \frac{\partial \psi(\mathbf{r}, t)}{\partial t} = \hat{H} \psi(\mathbf{r}, t) \quad (4.1)$$

where \hat{H} is the Hamiltonian of the system, the state ψ given by $|\psi(t)\rangle = \sum_i |i\rangle c_i(t)$ with the base states $|i\rangle$ and the amplitudes $c_i(t) = \langle i | \psi \rangle$ to find the state ψ in one of the base states i at time t . By knowing how the coefficients $c_i(t)$ vary with time, we know how the $\psi(t)$ evolve with time.

In case of an unperturbed system e.g. an isolated atom, we have solutions for the time-dependent Schrödinger equation [33]:

$$\psi_n(r, t) = e^{-i\frac{E_n}{\hbar}t} |n\rangle, \quad \hat{H}_0 |n\rangle = E_n |n\rangle \quad (4.2)$$

If the system interacts with a field, the total Hamiltonian of the system is given by:

$$\hat{H}_{total} = \hat{H}_0 + \hat{H}_I \quad (4.3)$$

with the Hamiltonian of the unperturbed system \hat{H}_0 and the interaction Hamiltonian \hat{H}_I .

At first we will consider a simple atom with two non degenerate levels E_0 and E_1 and use a semi classical approach, where we will use the quantummechanical description for the states from above and describe the field classically.

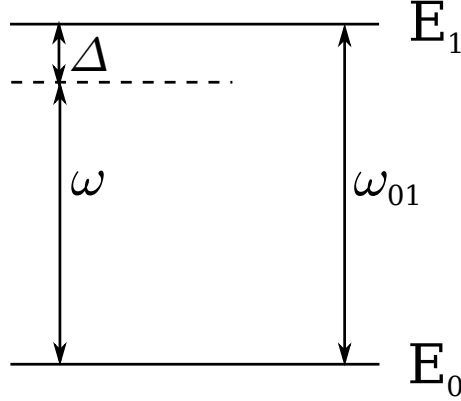


Figure 4.1: The two level system with states $|0\rangle$ and $|1\rangle$ and energies E_0 and E_1 , the transition frequency ω_{01} , the frequency of the oscillating field ω and the detuning Δ .

4.1.1 The Two Level Atom

It is worth considering the case of an atom with only two levels since, if the frequency of the field is near the transition frequency of these two levels, only the two atomic states of interest are involved in the process [34].

For the two level system with states $|0\rangle$ and $|1\rangle$ and energies E_0 and E_1 (see figure 4.1), we have the wave function $\psi(r, t) = c_0(t)\psi_0(r, t) + c_1(t)\psi_1(r, t)$ with $|c_0(t)|^2 + |c_1(t)|^2 = 1$ and a transition frequency of $\omega_{01} = \frac{E_1 - E_0}{\hbar}$.

After inserting this into the Schrödinger equation (and some algebra), we get the following equations for the coefficients $c_i(t)$:

$$i \frac{dc_0(t)}{dt} = c_0(t) \langle 0 | \hat{H} | 0 \rangle + c_1(t) e^{-i\omega_{01}t} \langle 0 | \hat{H} | 1 \rangle \quad (4.4)$$

$$i \frac{dc_1(t)}{dt} = c_0(t) e^{i\omega_{01}t} \langle 1 | \hat{H} | 0 \rangle + c_1(t) \langle 1 | \hat{H} | 1 \rangle \quad (4.5)$$

where $\langle i | \hat{H} | j \rangle$ denote the matrix elements of \hat{H} .

If the atom is now exposed to an oscillating magnetic field:

$$\vec{B}(t) = \vec{B}_1 \cos \omega t \quad (4.6)$$

with the field amplitude B_1 and the frequency ω , the atom interacts with the magnetic field via its magnetic moment and \hat{H}_I is given by [35]:

$$\hat{H}_I = \vec{\mu}\vec{B}(t) = \vec{\mu}\vec{B}_1 \cos \omega t \quad (4.7)$$

where μ denotes the magnetic transition moment between the two states. With this, we can write the matrix elements of the interaction Hamiltonian:

$$\langle i|\hat{H}_I|i\rangle = 0 \quad (4.8)$$

$$\langle i|\hat{H}_I|j\rangle = B_1\mu_{ij} \cos \omega t \quad (4.9)$$

where $\mu_{ij} = \langle i|\mu|j\rangle$ is the magnetic transition moment between the two states i and j (see 4.4.1 for an example).

Furthermore, we define the Rabi frequency [36]:

$$\Omega_R = \frac{\mu_{ij}B_1}{\hbar} \quad (4.10)$$

which characterizes the atom-field interaction strength. The equations 4.4 become [36]:

$$i\frac{dc_0(t)}{dt} = \omega_0c_0(t) + \Omega_Rc_1(t) \cos \omega t e^{-i\omega_0t} \quad (4.11)$$

$$i\frac{dc_1(t)}{dt} = \omega_1c_1(t) + \Omega_R^*c_0(t) \cos \omega t e^{i\omega_0t} \quad (4.12)$$

using $\cos \omega t = \frac{1}{2}(e^{i\omega t} + e^{-i\omega t})$ and the approximation $|\omega - \omega_0| \ll \omega$ for frequencies ω close to the transitions frequency (rotating wave approximation [35]) and the initial conditions $|c_0(t)|^2 = 1$ and $|c_1(t)|^2 = 0$, we get the following result at resonance $\omega = \omega_0$:

$$|c_0(t)|^2 = \cos^2(\Omega_R t/2) \quad (4.13)$$

$$|c_1(t)|^2 = \sin^2(\Omega_R t/2) \quad (4.14)$$

which describe the probabilities of finding the atom in the ground or the excited state after being in a radiation field for a time t .

4.1.2 Density matrices

Since we are actually interested in the probabilities $|c_i(t)|^2$ rather than $c_1(t)$, it is more convenient to use the density matrix formalism. The time evolution of the density matrix is given by the von Neumann equation [37]:

$$\frac{d\hat{\rho}}{dt} = \frac{i}{\hbar}[\hat{\rho}, \hat{H}] \quad (4.15)$$

where $\hat{\rho}$ is the density operator for a state and given by: $\hat{\rho} = |\psi\rangle\langle\psi|$ and may be written as a matrix e.g. for the two level atom:

$$\hat{\rho} = \begin{pmatrix} c_0 \\ c_1 \end{pmatrix} \begin{pmatrix} c_0^* & c_1^* \end{pmatrix} = \begin{pmatrix} |c_0|^2 & c_0 c_1^* \\ c_1 c_0^* & |c_1|^2 \end{pmatrix} = \begin{pmatrix} \rho_{00} & \rho_{01} \\ \rho_{10} & \rho_{11} \end{pmatrix} \quad (4.16)$$

with $\rho_{00} + \rho_{11} = 1$.

The meaning of the matrix elements of the operator $\hat{\rho}$ is the following: The diagonal matrix elements are the square of the probability amplitude to be in a certain state - so they give us the probability of finding the atom in this state. The off-diagonal elements are called coherences and express the interference between states [37].

In order to describe mixed states, we write [34]: $\sum_k p_k |\psi_k\rangle\langle\psi_k| = \sum_k p_k \rho_k$ with the probability p_k of the system being in state ψ_k .

With $d\rho_{ij}/dt = c_i(t)(dc_j^*(t)/dt) + (dc_j(t)/dt)c_i^*(t)$, equations 4.11 and again the rotating wave approximation, we get the optical Bloch equations for the density matrix elements of the two level system [36]:

$$\frac{d\rho_{11}}{dt} = -\frac{d\rho_{00}}{dt} = -i\frac{\Omega_R}{2}(e^{i(\omega_{01}-\omega)t}\rho_{01} - e^{-i(\omega_{01}-\omega)t}\rho_{10}) \quad (4.17)$$

$$\frac{d\rho_{01}}{dt} = \frac{d\rho_{10}^*}{dt} = i\frac{\Omega_R}{2}e^{-i(\omega_{01}-\omega)t}(\rho_{00} - \rho_{11}) \quad (4.18)$$

by substituting $\rho'_{01} = e^{i(\omega_{01}-\omega)t}$ and $\rho'_{10} = e^{-i(\omega_{01}-\omega)t}$, the equations simply become [36]:

$$\frac{d\rho'_{11}}{dt} = -\frac{d\rho'_{00}}{dt} = -i\frac{\Omega_R}{2}(\rho'_{01} - \rho'_{10}) \quad (4.19)$$

$$\frac{d\rho'_{01}}{dt} = \frac{d\rho'^*_{10}}{dt} = i\frac{\Omega_R}{2}(\rho'_{00} - \rho'_{11}) + i(\omega_0 - \omega)\rho'_{01} \quad (4.20)$$

with $\rho'_{ii} = \rho_{ii}$.

Analogous, the optical Bloch equations for the four level atom can be derived. In this case, we will have a 4×4 density matrix and Hamiltonian, resulting in 10 independent equations for the ρ_{ij} . By calculating the matrix elements $\langle i|\hat{H}|j\rangle$ of the transitions of interest (see section 4.4.1), the equations will simplify. For the σ_1 transition, static and oscillating field will be parallel, so the entry of the transition with $\Delta m_F = 0$ is relevant, whereas for the fields being perpendicular to each other, transitions with $|\Delta m_F| = 1$ will be excited [38].

In the next section, the numerical method to solve the equations used in the simulation program will be discussed.

4.2 Solving the optical Bloch equations numerically

In order to solve the optical Bloch equations, we use the Rung-Kutta-Fehlberg method with adaptive stepsize control.

Runge-Kutta methods are a group of iterative algorithms to numerically solve ordinary differential equations:

$$\frac{dy}{dt} = f(t, y) \quad (4.21)$$

with y being an unknown function depending on t .

The most commonly used member is the Runge-Kutta method of fourth order where four evaluations of the right-hand side of the differential equation are needed in order to calculate an estimation of y_{n+1} after a step h [40]:

$$k_1 = hf(t_n, y_n) \quad (4.22)$$

$$k_2 = hf\left(t_n + \frac{1}{2}h, y_n + \frac{1}{2}k_1\right) \quad (4.23)$$

$$k_3 = hf\left(t_n + \frac{1}{2}h, y_n + \frac{1}{2}k_2\right) \quad (4.24)$$

$$k_4 = hf(t_n + h, y_n + k_3) \quad (4.25)$$

$$y_{n+1} = y_n + \frac{1}{6}k_1 + \frac{1}{3}k_2 + \frac{1}{3}k_3 + \frac{1}{6}k_4 + \mathcal{O}(h^5) \quad (4.26)$$

where the k_n denote four increments which are evaluations of the right side at certain ts and are then averaged to get y_{n+1} .

The Runge-Kutta methods treat every step in the interval of integration T the same - the information of a truncation error after one iteration is lost. In this manner, it is likely that the stepsize is chosen too large and the solution will be useless.

In order to avoid this, the Runge-Kutta method will be combined with an adaptive stepsize control. This requires that the algorithm provides an estimation of the truncation error for every step.

In case of the Runge-Kutta-Fehlberg method, six function evaluations are calculated along each step which can then be combined to get a fourth and a fifth order solution. The difference between the two solutions gives an estimation of the truncation error and is used as an indicator whether the stepsize is too large or too small. In general, the fifth order method is [40]:

$$k_1 = hf(t_n, y_n) \quad (4.27)$$

$$k_2 = hf(t_n + c_2, y_n + a_{21}k_1) \quad (4.28)$$

$$\dots \quad (4.29)$$

$$k_6 = hf(t_n + c_6h, y_n + a_{61}k_1 + \dots + a_{65}k_5) \quad (4.30)$$

$$y_{n+1}^5 = y_n + b_1k_1 + b_2k_2 + b_3k_3 + b_4k_4 + b_5k_5 + b_6k_6 + \mathcal{O}(h^6) \quad (4.31)$$

$$y_{n+1}^4 = y_n + b_1^*k_1 + b_2^*k_2 + b_3^*k_3 + b_4^*k_4 + b_5^*k_5 + b_6^*k_6 + \mathcal{O}(h^5) \quad (4.32)$$

where the constants a_{ij} , b_i and c_i we are using are determined by Dormand and Prince [40].

The estimated truncation error is thus given by:

$$\Delta = y_{n+1}^5 - y_{n+1}^4 \quad (4.33)$$

Because we are solving a set of 16 equations, Δ will actually be a vector with 16 entries. In the program, we use the norm of this vector as an error estimate err .

In order to keep Δ in certain boundaries during the computation ($|\Delta| \leq \text{bound}$), we will now need to introduce an absolute and a relative error tolerance for Δ which should be considered by the algorithm:

$$\text{bound} = \text{atol} + |y| \text{rtol} \quad (4.34)$$

The error err will then be given by [40][39]:

$$\text{err} = \sqrt{\frac{1}{N} \sum_{i=0}^{N-1} \left(\frac{\Delta_i}{\text{bound}_i} \right)^2} \quad (4.35)$$

and the calculated step will only be accepted if $\text{err} \leq 1$, otherwise it will be recalculated. If the stepsize is now too large, how can a "better" value for the recalculation be predicted?

Since Δ scales with h^5 (4.27), err will too and the relation between two different stepsizes h_0 and h_1 is given by:

$$h_0 = h_1 \left| \frac{\text{err}_0}{\text{err}_1} \right|^{1/5} \quad (4.36)$$

The strategy will now be to assume h_0 is the "ideal" stepsize resulting in $\text{err}_0 = 1$, then eq. 4.36 tells us how much the stepsize needs to be decreased or how much we are allowed to increase it.

Since the error estimation is not exact and experience has shown that increasing/decreasing the stepsize too dramatically is not wise [40], we will use a safety factor S which is a few percent smaller than 1. We get [40]:

$$h_{n+1} = S h_n \left(\frac{1}{\text{err}_n} \right)^{1/5} \quad (4.37)$$

This stepsize control can be further improved when turning to control theory. Using the so called PI (proportional and integral feedback) controller, we get:

$$h_{n+1} = Sh_n \text{err}_n^{-\alpha} \text{err}_{n-1}^\beta \quad (4.38)$$

For values of $\beta = 0$ and $\alpha = 1/k$ with k being the order of the method we will arrive at equation 4.38 again. A nonzero β will lead to a higher stability but will decrease the speed of the algorithm. We will use $\beta = 0.4/k$ and $\alpha = 1/k - 0.75\beta$ which turned out to be a good compromise [41].

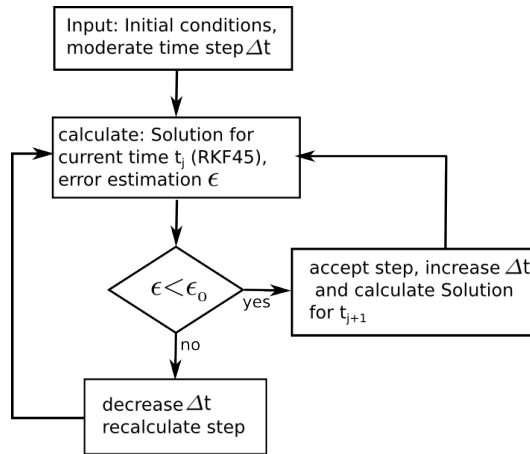


Figure 4.2: Flow diagram of the Runge-Kutta-Fehlberg algorithm.

4.3 Geometry and Setup Implementation

The `hbar_gshfs` simulation program is based on the particle physics toolkit Geant4 (**GE**ometry **ANd** **T**racking) which was developed at CERN [42].

However, since Geant4 is mainly designed for high energy physics, we had to implement processes which are important to us but are neglected in Geant4. These are for example: the tracking of neutral particles in magnetic fields,

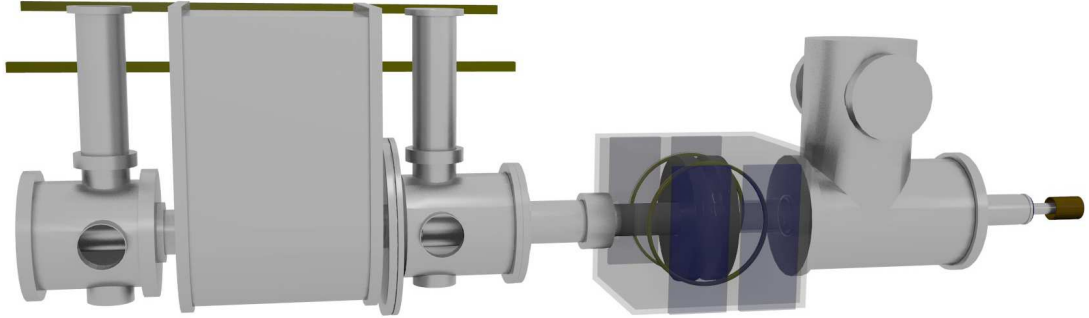


Figure 4.3: Rendered geometry of the whole setup implemented in Geant4. From left to right: cusp trap, cavity inside see-through shielding and scintillators (blue plates) for beam normalisation, sextupole magnet and detector (yellow).

higher excited states and their deexcitation processes and atomic transitions in a radiofrequency field which are discussed in this work.

In figure 4.3, one can see a picture of the geometry of the setup currently implemented in the simulation program. Technical drawings were used for dimensions. Figure 4.4 shows a close-up of the cavity in the setup.

The geometry of the cavity alone is shown in figure 4.5, the front flange removed, so the inside of the cavity is visible. One can see the resonator plates and wings, as well as the beam blockers at the back and front entrance. The static magnetic field is provided by the Helmholtz coils (inside yellow support structure).

In table 4.1 an overview of all geometry parameters used in the following simulations is shown.

In order to obtain a resonance scan, the frequency of the oscillating field inside the cavity is varied around the expected transition frequency. For a certain number of scan points N_0 particles per point are shot through the setup.

Beam and source settings are summarized in table 4.2. The source center

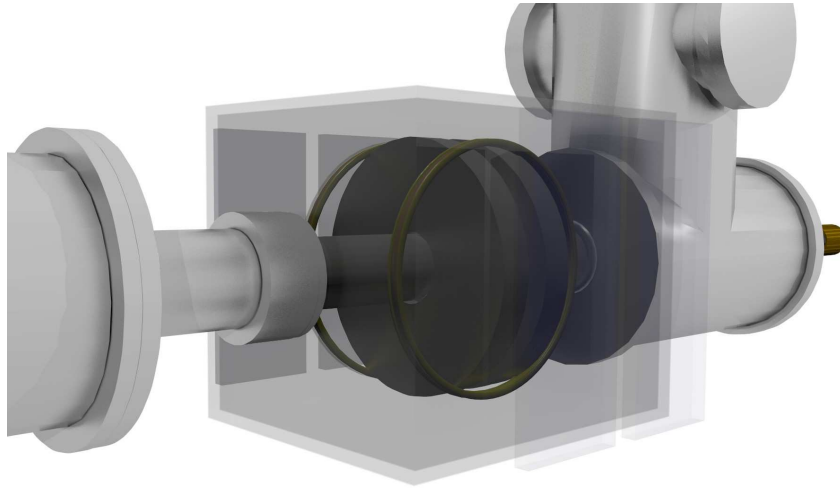


Figure 4.4: Rendered geometry of the spin-flip cavity inside the setup. Shielding and scintillator counters are see-through.

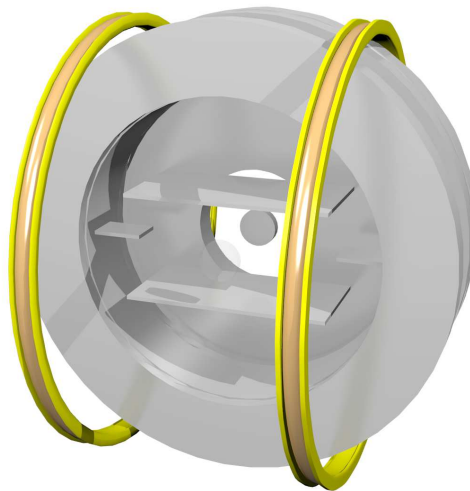


Figure 4.5: Rendered geometry of the spin-flip cavity as implemented in the Geant4 program. Dimensions were obtained from technical drawings.

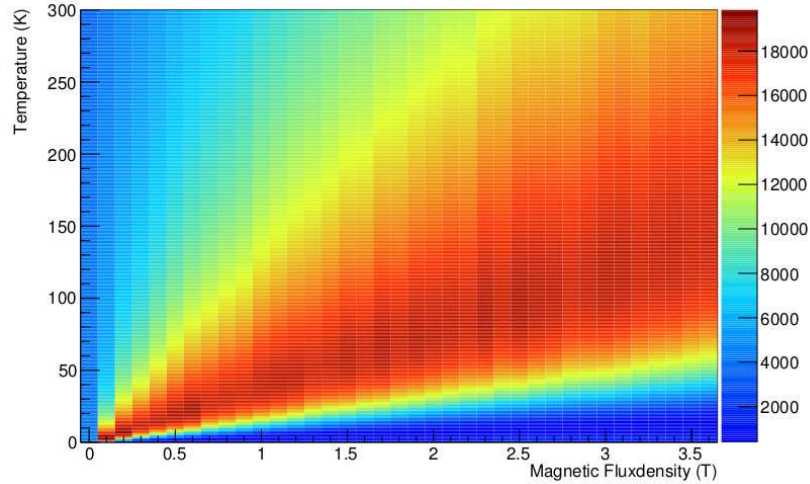


Figure 4.6: Detector counts for different temperatures (K) and magnetic fluxdensity (T) of the sextupole magnet.

is set to the point $(0, 0, -0.5\text{m})$ which has a distance of 44.75 cm from the cavity entrance. Coordinates used are with respect to cavity center.

The beam is shot in z -direction and has a FWHM of 10 cm - N_0 is then the number of particles inside the 10 cm. The distribution in the xy -plane is gaussian and the beam is set to be parallel without divergence.

Every particle has a random initial state (one of the four groundstates) depending on the beam polarization. For all the following resonance scans, a polarization of 70% LFS and 30% HFS has been chosen since this is the expected polarization of the CUSP trap [25].

Resonance scans for different initial polarizations are shown in figure 4.7. For an unpolarized beam (50% LFS, 50% HFS) of course, the transition cannot be seen. With increasing percentage of LFS, the amplitude of the two peaks increases linearly.

The beam energy can be chosen to be fixed or obtained from beam temperature resulting in an beam velocity which is Maxwell-Boltzmann distributed.

Before and after the cavity, two beam blockers are placed in order to cut out the central part of the beam. This is necessary since the sextupole field is 0 at its center and therefore cannot analyze the spins of particles passing

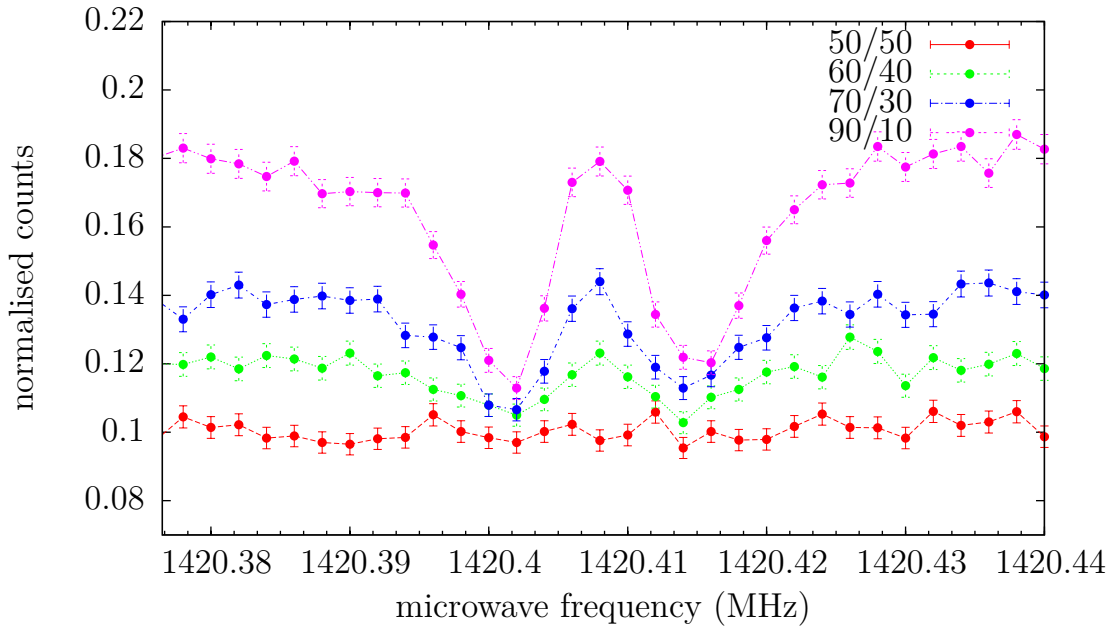


Figure 4.7: Scans with different initial polarization: red: 50% LFS, 50% HFS (unpolarized beam), green: 60% LFS, 40% HFS, blue: 70% LFS, 30% HFS, magenta: 90% LFS, 10% HFS.

through the center.

At a distance of 53.75 cm after the cavity, the beam enters the sextupole magnet which analyzes the spin state of the antihydrogen atoms, defocusing the HFS and focusing the LFS on the detector. Depending on the beam energy, the strength of the sextupole field needs to be adjusted. Figure 4.6 shows particles counted by the dummy detector depending on different temperatures and B-field strength of the sextupole magnet.

In order to detect the antihydrogen atoms at the end of the beamline a dummy detector is used which is a stainless steel disc with a diameter of 12 cm and distance of 71 cm from the sextupole. Here all antihydrogen atoms hitting the disc will simply be counted (N_{det}). The background events will be ignored for now, this results in a detection efficiency of 100%.

4 Simulation of the GSHFS Transitions of H/\bar{H}

| Parameter | Value (m) | Comment |
|---|---------------|---|
| Cavity dimensions | | |
| Center of cavity | (0,0,0) | coordinates w.r.t. world volume of cylindrical tank |
| Inner diameter | 0.317 | |
| Outer diameter | 0.460 | |
| Cavity length | 0.105 | |
| Flange diameter | 0.459 | before and after cavity |
| Flange hole diameter | 0.1302 | |
| Resonator thickness | 0.004 | |
| Resonator width | 0.21005 | |
| Resonator separation | 0.104 | |
| Helmholtz coil outer diameter | 0.454 | |
| Helmholtz coil thickness | 0.016 | |
| Helmholtz coil distance | 0.212 | |
| Shielding thickness | 0.001 | |
| Inner shielding length | 0.531 | |
| Inner shielding height | 0.606 | |
| Outer shielding length | 0.561 | |
| Outer shielding height | 0.636 | |
| Shielding hole diameter | 0.14 | |
| Wings length | 0.053 | |
| Wings width | 0.036 | |
| Wings thickness | 0.004 | |
| Beam Stopper | | |
| Position 1 | (0,0,-0.056) | beam stopper before cavity |
| Position 2 | (0,0,-0.0525) | beam stopper after cavity |
| Thickness | 0.0035 | |
| Diameter | 0.04 | |
| Sextupole Magnet | | |
| Position | (0,0,0.59) | |
| Length | 0.22 | |
| Inner diameter | 0.10 | |
| Outer diameter | 0.16 | |
| Dummy detector stainless steel disc | | |
| Position | (0,0,1.52) | |
| Thickness | 0.01 | |
| Diameter | 0.12 | |

Table 4.1: Geometry parameters used in the Geant4 simulations.

| Beam and source settings | | |
|----------------------------|----------------------|---|
| Source position | (0 m,0 m,-0.5 m) | in front of the cavity |
| Source FWHM _X | 0.1 m | |
| Source FWHM _Y | 0.1 m | |
| Source FWHM _Z | 0.0 m | |
| Polarization | 70% LFS, 30% HFS | |
| Particles shot | N_0 | per scan point |
| Detector hits | N_{det} | per scan point |
| Normalised counts | N_{det}/N_0 | y-axis of scan plots |
| Error bars | $\sqrt{N_{det}/N_0}$ | |
| Fit parameters | | |
| baseline | b | |
| Amplitude | A | amplitude of the two gaussian peaks |
| Central frequency | ν_i | i denoting the transition i.e. 0, σ or π |
| Peak separation | s | peak to peak sep. of the two gaussian |
| Standard deviation | σ | |
| Full width at half maximum | f | 2.355σ |
| Degrees of freedom | N_f | |

Table 4.2: Beam and source settings used in the simulations. Overview of fit parameters as discussed in section 4.5.1.

4.4 Implementation of the Magnetic Fields

4.4.1 The Oscillating Magnetic Field

The strength of the B-field inside the cavity depends on the power the cavity is operated with. The input power of the cavity is given by [43]:

$$P = \frac{\omega_0 W}{Q} \quad (4.39)$$

with the resonance frequency ω_0 , the stored energy W in the volume and the quality factor of the cavity Q (in all following power calculations a Q factor of 100 was used). The stored energy corresponding to a certain field amplitude was determined by simulations [43], with the following result: 1 Joule stored

energy corresponds to a H-field amplitude of 2.7×10^4 A/m. Using $H = \frac{B}{\mu_0}$ this gives a B-field of 340 T.

The stored energy w per unit volume is given by:

$$w = \frac{B_a^2}{2\mu_0} \quad (4.40)$$

With the ingredients above, one can calculate the input power for the field amplitude of interest.

In order to calculate the optimum oscillating field strength inside the cavity, we consider the probability of a two-state atom being in the second state if the system was certainly in state 1 at the beginning [44]:

$$|C_2(t)|^2 \propto \sin^2(\Omega t/2) \quad (4.41)$$

with the Rabi frequency Ω between the two states. The atoms spend the average time t inside the oscillating field of the cavity, which is calculated by $t = L_c/\bar{v}$ where L_c denotes the length of the cavity in beam direction and \bar{v} the most probable velocity of the atoms (Maxwell-Boltzmann distributed velocities assumed):

$$v = \sqrt{\frac{2kT}{m}} \quad (4.42)$$

If now the Rabi frequency fulfills the condition:

$$\Omega = \pi/t \quad (4.43)$$

the probability in equation 4.41 has a maximum and spin flips occur.

The strength of the oscillating field is linked to the interaction Hamiltonian which is related to the Rabi frequency by [45]:

$$\hbar\Omega_{ij} = H_{ij} \quad (4.44)$$

To calculate Ω_{ij} for the transitions of interest we need to determine the corresponding matrix elements H_{ij} .

The σ_1 transition

To excite the transition between (1,0) and (0,0), an oscillating magnetic field parallel to the static magnetic field is necessary, assuming:

$$\vec{B} = B_a \vec{z} \sin \omega t \quad (4.45)$$

with the field strength B_a . The Hamiltonian $\hat{H} = -\vec{\mu}\vec{B}$ with $\vec{\mu} = \vec{\mu}_S + \vec{\mu}_I = \mu_{BGS}\vec{S}/\hbar + \mu_{NGI}\vec{I}/\hbar$ is then given by:

$$\hat{H} = \frac{B_a}{\hbar} \sin \omega t (\mu_{BGS}\vec{S}_z + \mu_{NGI}\vec{I}_z) \quad (4.46)$$

The matrix elements of \hat{H} for the σ_1 transition is then given by:

$$H_{\sigma_1} = \langle 00 | \hat{H} | 10 \rangle \quad (4.47)$$

Since the quantization axis is z as defined by the static magnetic field, the base $|S_z, I_z\rangle$ is used and we have:

$$\begin{aligned} |00\rangle &= \frac{1}{\sqrt{2}} (|\uparrow\downarrow\rangle - |\downarrow\uparrow\rangle) \\ |11\rangle &= |\uparrow\uparrow\rangle \\ |10\rangle &= \frac{1}{\sqrt{2}} (|\uparrow\downarrow\rangle + |\downarrow\uparrow\rangle) \\ |1-1\rangle &= |\downarrow\downarrow\rangle \end{aligned}$$

Thus, for the matrix element we get:

$$H_{\sigma_1} = -\frac{B_a}{4} \sin \omega t (\mu_{BGS} - \mu_{NGI}) \quad (4.48)$$

and with equation 4.44, we can calculate the Rabi frequency for the σ_1 transition:

$$\Omega_{\sigma_1} = \frac{B_a}{2\hbar} (\mu_{BGS} - \mu_{NGI}) \quad (4.49)$$

and together with equation 4.43 and the approximation $\mu_{BGS} - \mu_{NGI} \approx \mu_{BGS}$ because of $\mu_N = m_e/m_p\mu_B$, for the optimum oscillating magnetic field strength, we get:

$$B_a = \frac{2\pi\hbar}{t\mu_B} \quad (4.50)$$

In order to test the above estimation of the oscillating field strength and power, the spin flip probability for the σ_1 transition was calculated for different velocities.

Using equation 4.42 we get a most probable velocity for 50 K of about 900 m/s which gives us a power estimation of ≈ 0.03 W with the above calculation.

The power in the cavity was therefore set to 0.03 W and a beam of 4000 atoms all in the state (1,0) and with an equally distributed velocity ranging from 0 zu 1500 m/s was shot through the cavity. The static magnetic field in the cavity was set to 0. Figure 4.8 shows the probability of the atoms being in state (0,0) after the cavity i.e. the probability for the σ_1 transition. One can nicely see the maxima of the probability at about 900 m/s.

The oscillations of probability at lower velocities can be understood by taking a look at the probability in equation 4.41 which has a $\sin^2(t)$ dependence on time. Substituting the time t by the velocity, we get a probability with a $\sin^2(1/v)$ dependence which can be nicely seen in figure 4.8.

The π_1 transition

In order to excite the transitions with $\Delta m_F = \pm 1$, in particular from (1,-1) to (0,0), static and oscillating field need to be perpendicular to each other, we may assume without loss of generality:

$$\vec{B} = B_a \vec{x} \sin \omega t \quad (4.51)$$

The Hamiltonian takes the form: $\hat{H} = \frac{B_a}{\hbar} \sin \omega t (\mu_{BGS} \vec{S}_x + \mu_{NGI} \vec{I}_x)$. The determination of B_a for the π_1 transition is then analogue to the above calculation and we get a Rabi frequency of:

$$\Omega_{\pi_1} = \frac{B_a}{2\sqrt{2}\hbar} (\mu_{BGS} - \mu_{NGI}) \quad (4.52)$$

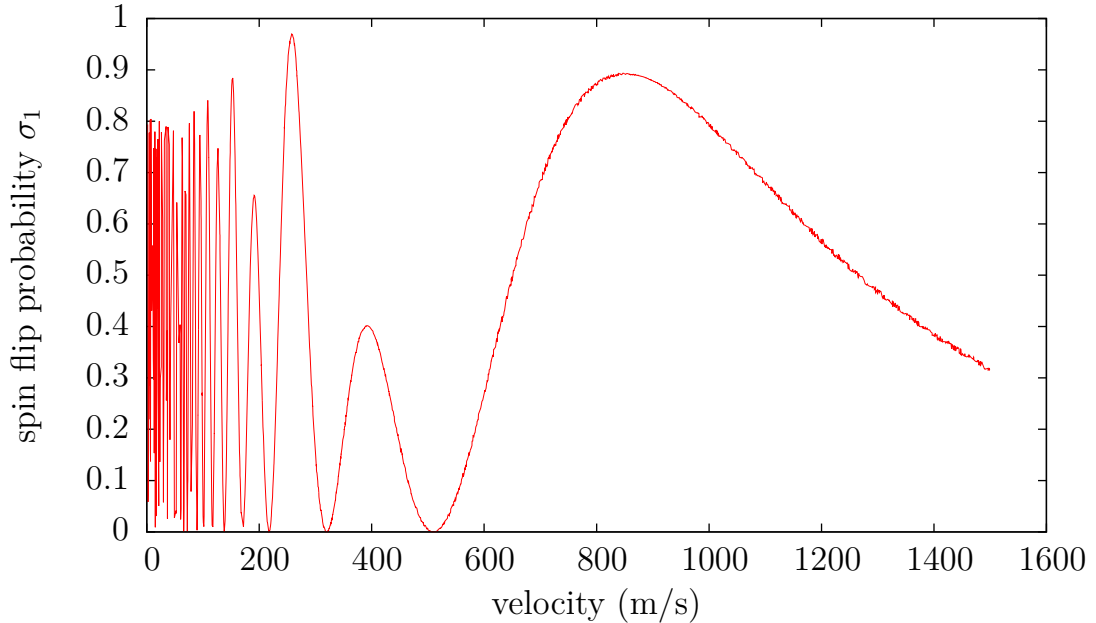


Figure 4.8: Probability of the atoms being in state $(0,0)$ after the cavity i.e. the probability for the σ_1 transition. A beam of 4000 antihydrogen atoms all in the state $(1,0)$ and with an equally distributed velocity ranging from 0 zu 1500 m/s was used.

and for the amplitude of the oscillating field:

$$B_a = \frac{\sqrt{2}\pi\hbar}{t\mu_B} \quad (4.53)$$

The same test as for the σ_1 transition was also done for the π_1 transition. Again a beam of 4000 atoms this time all in the state $(1,-1)$ and with an equally distributed velocity ranging from 0 zu 1500 m/s was shot through the cavity. Figure 4.9 shows the probability of the atoms being in state $(0,0)$ after the cavity i.e. the probability for the π_1 transition.

Here, the maxima is at 1100 m/s. Note also, that the probability at the maxima is about 0.3. For the σ_1 transition, the probability at this point is about 0.9. A possible explanation could be, that at an angle of 90° between static and oscillating field all transitions with $|\Delta m_F| = 1$ might be excited

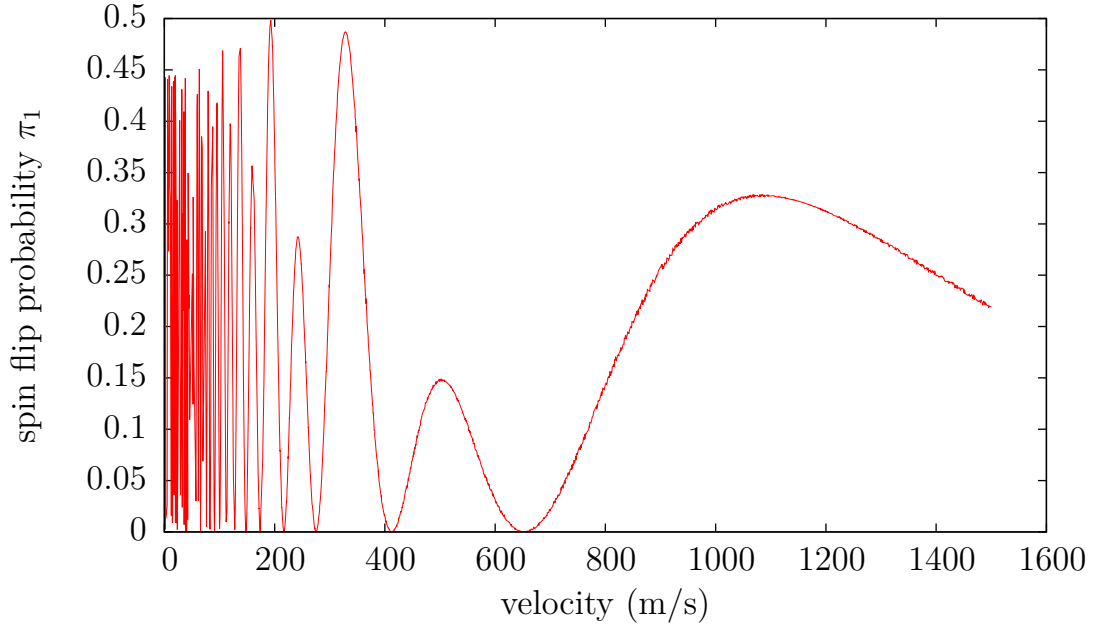


Figure 4.9: Probability of the atoms being in state (0,0) after the cavity i.e. the probability for the σ_1 transition. A beam of 4000 antihydrogen atoms all in the state (1,-1) and with an equally distributed velocity ranging from 0 zu 1500 m/s was used.

whereas at an angle of 0° , only one transition with $|\Delta m_F| = 0$ is possible.

4.4.2 The Static Magnetic Field

For the static magnetic field inside the cavity, one can choose between two ways of realisation:

1. The B-field is equally distributed and set to a constant value and for every particle entering the cavity. This might seem crude at first glance, but is still useful when studying effects of e.g. beam temperature and keeping the B-field completely homogeneous while doing so, see section 4.5.2.
2. Measured or simulated fieldmaps of the B-field inside the cavity volume

can be used to gain more realistic results. To obtain accuracy, the fieldmaps are cubic spline interpolated in an extra program before they are used in the simulations. The data files will be read in by the `hbar_gshfs` program and will then be ordered in a 3-dimensional binary tree in order to speed up the search for the nearest neighbours.

Histograms of measured and computationally generated fieldmaps are shown in figures 4.29 and 4.28.

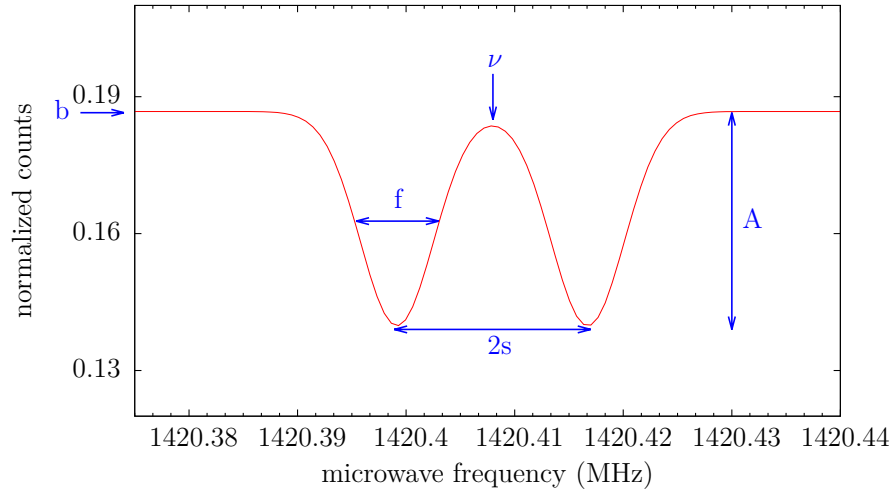


Figure 4.10: Graphical illustration of the fit function and fit parameters.

4.5 Simulation Results

4.5.1 Fitting the Scans

In order to analyze the simulated data, the following function is used to fit the resonance scans:

$$\mathcal{G}(x) = b - Af(x, \nu_i - s, \sigma) - Af(x, \nu_i + s, \sigma) \quad (4.54)$$

with the baseline b , the amplitude A , the mean value ν_i , the peak separation s and the standard deviation σ . f is given by:

$$f(x, \nu_i, \sigma) = \frac{1}{\sigma\sqrt{2\pi}} \exp^{-\frac{1}{2}\left(\frac{x-\nu_i}{\sigma}\right)^2} \quad (4.55)$$

An overview of the fit parameters is shown in table 4.2 and a graphical illustration can be seen in figure 4.10.

Note, that this fit function is used for reasons of simplicity and does not describe the side maxima and also the central peak not too well.

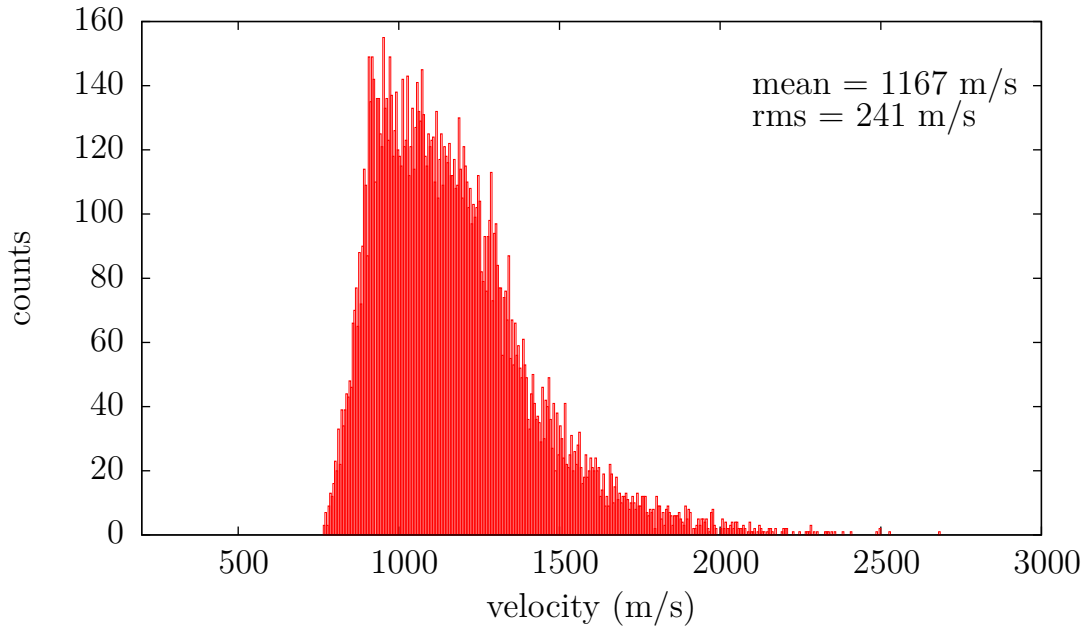


Figure 4.11: Velocity distribution at the detector using $N_0 = 10^5$ and a temperature of 50 K.

4.5.2 Dependence on Beam Temperature

For all the following scans high statistics ($N_0 = 10^5$ antihydrogens) and a completely homogeneous static magnetic field were used in order to study the effect of different velocity distributions of the beam on the scans. In figure 4.11 the velocity distribution at the detector for atoms with a Maxwell-Boltzmann distributed velocity obtained from simulations is shown. When comparing to monovelocity beam, the mean velocity of the histograms is used.

Figures 4.12, 4.13 and 4.14 show resonance scans of the σ_1 transition at different temperatures. 20 K, 50 K and 90 K were chosen. Note the offset of the baseline between monovelocity simulated scans and scans with Maxwell-Boltzmann distributed velocity which is a result of the sextupole whose strength is set to focus the most probable velocity of the beam.

Also for the MB beam, the side maxima wash out completely.

In figure 4.15, the peak amplitude for scans of the gaussian peaks is plotted

4 Simulation of the GSHFS Transitions of H/\bar{H}

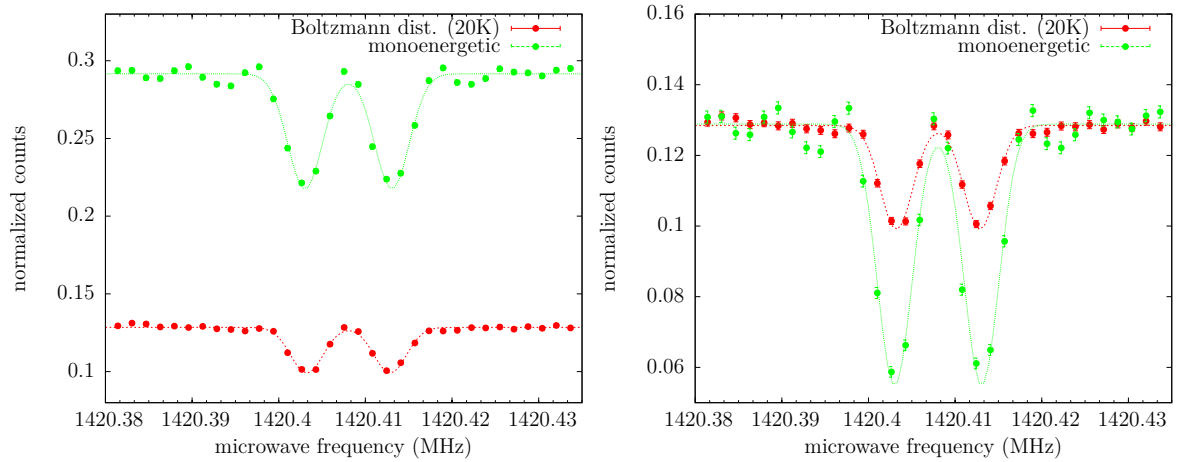


Figure 4.12: Scans of the σ_1 transition at 20 K. *Left*: σ_1 transition for a monoenergetic beam (green) and a beam with Boltzmann distributed velocity (red). *Right*: Same as left, only with an downward shift of the baseline for the green scan in order to allow better comparison. 10^5 antihydrogen atoms per scan point were used and a polarization of 70 % LFS and 30 % HFS.

depending on the beam temperature. Resonance scans with temperatures ranging from 20 K to 90 K with steps of 10 K were done. For the scans with the monoenergetic beam the velocity was set to the mean velocity of the Maxwell-Boltzmann distribution.

Comparing green and red curves, one can see a clear offset in amplitude which stays approximately constant for the different temperatures. Note that in the right scan plots a downward shift was applied to the monovelocity scan in order to allow better comparison.

The FWHM of the gaussians of the fit in dependence of temperature is shown in figure 4.16. With higher temperature (or velocity, in case of the monoenergetic beam) the peaks get broader. Also, comparing the green and red points, one can not see a big difference.

Figure 4.17 shows the error of the central peak position for varying temperatures. Again one notices an offset between results of the monoenergetic beam and the results using a Maxwell-Boltzmann distributed velocity, the latter one having a higher error of ≈ 42 %. As expected, the error obtained by fit

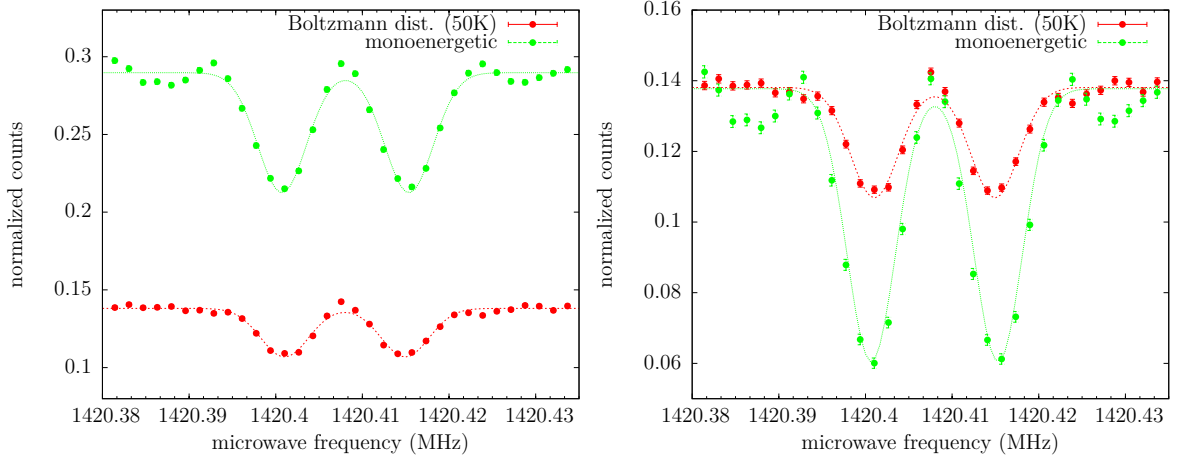


Figure 4.13: Scans of the σ_1 transition at 50 K. *Left*: σ_1 transition for a monoenergetic beam (green) and a beam with Boltzmann distributed velocity (red). *Right*: Same as left, only with an downward shift of the baseline for the green scan in order to allow better comparison. 10^5 antihydrogen atoms per scan point were used and a polarization of 70 % LFS and 30 % HFS.

increases with higher velocity.

In figure 4.18 the peak separation for different temperatures is shown. It increases with temperature and the difference between the monovelocity simulations and the MB beam simulations is marginal.

Since we use a beam with Maxwell-Boltzmann distributed velocity, the most probable velocity of the particles is proportional to \sqrt{T} . Therefore Figure 4.19 shows peak separation and FWHM of the gaussian peaks in dependence of \sqrt{T} in order to investigate the velocity dependence of the structure of the resonance spectra. It can be seen that simulation results of peak separation and FWHM increase with similar form with temperature.

The plots in figure 4.20 show a comparison between calculated FWHM using equations 3.1 and 3.2 and simulated FWHM in dependence of temperature. One can see that the peak width for the B-field configuration of the ASACUSA cavity is much narrower than with the constant B-field assumed for the calculation.

All fit results plotted in this section can be found in the Appendix, see 6.1.

4 Simulation of the GSHFS Transitions of H/\bar{H}

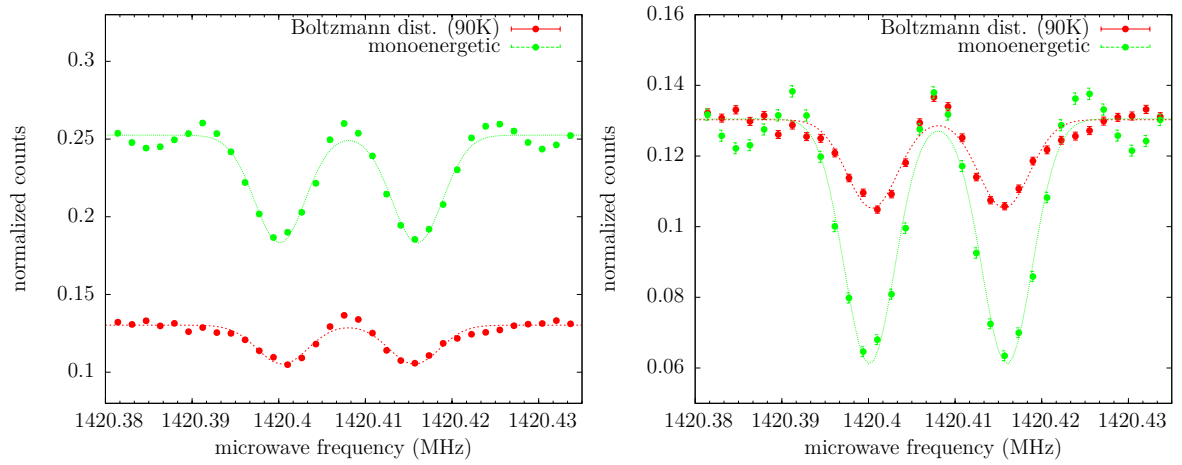


Figure 4.14: Scans of the σ_1 transition at 90 K. *Left*: σ_1 transition for a monoenergetic beam (green) and a beam with Boltzmann distributed velocity (red). *Right*: Same as left, only with an downward shift of the baseline for the green scan in order to allow better comparison. 10^5 antihydrogen atoms per scan point were used and a polarization of 70 % LFS and 30 % HFS.

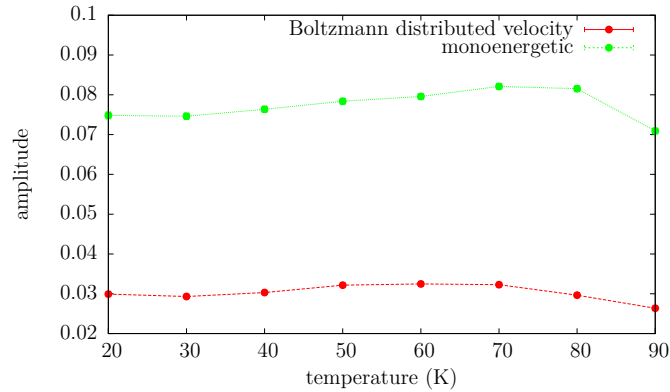


Figure 4.15: Amplitude of the two gaussians in dependence of the temperature for the monoenergetic beam (green) and the beam with Boltzmann distributed velocity (red).

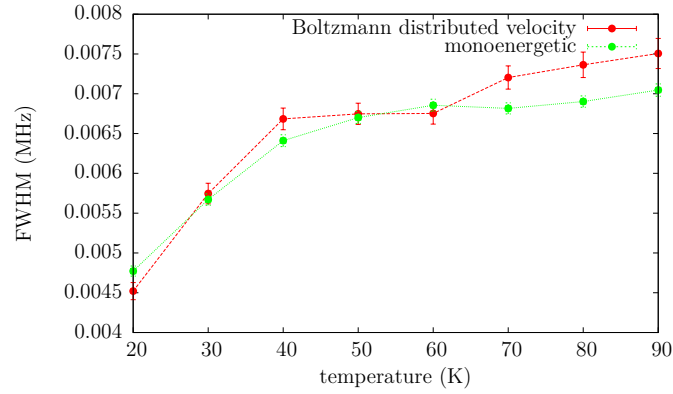


Figure 4.16: Peak width of the two gaussians in dependence of the temperature for the monoenergetic beam (green) and the beam with Boltzmann distributed velocity (red).

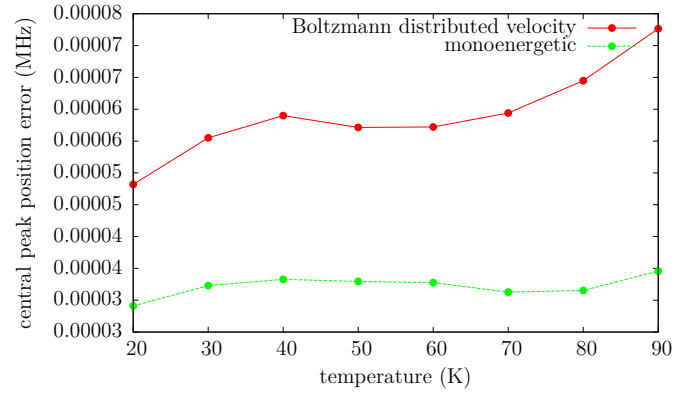


Figure 4.17: Error of the central peak position in dependence of the temperature for the monoenergetic beam (green) and the beam with Boltzmann distributed velocity (red).

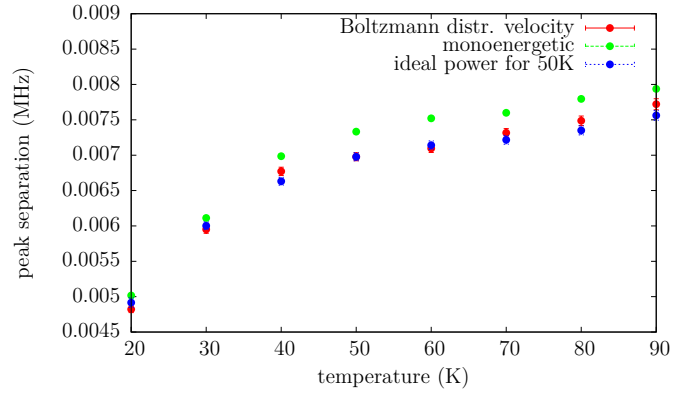


Figure 4.18: Peak Separation of the two gaussians in dependence of temperature.

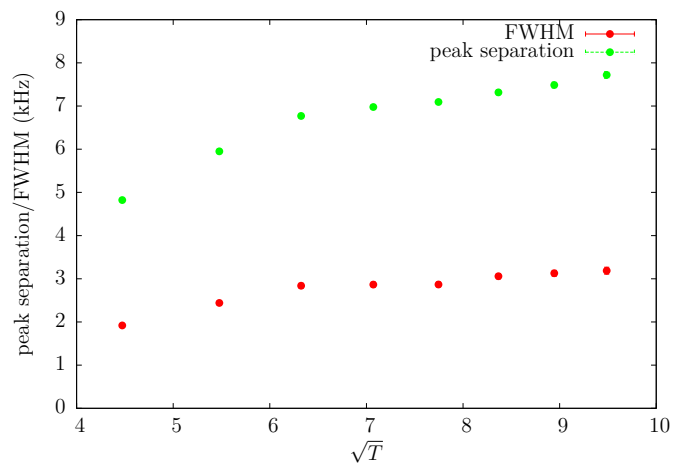


Figure 4.19: Peak Separation and FWHM of the two gaussians in dependence of \sqrt{T} with T being the temperature.

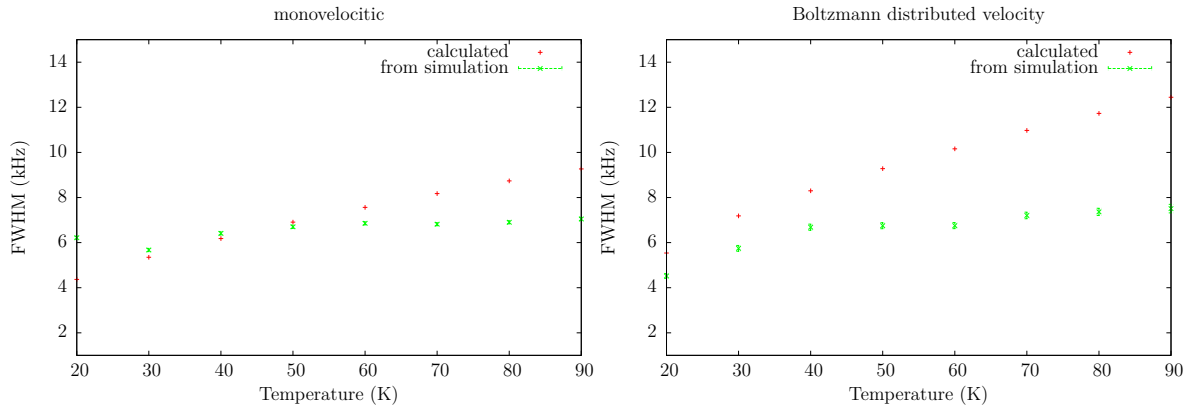


Figure 4.20: FWHM (kHz) in dependence of beam temperature (K). *Left*: FWHM for a monovelocity beam. Red points symbolize the calculated values for the FWHM using equation 3.1. In case of the simulation results (green points), the beam velocity is set to the most probable velocity of the corresponding Maxwell-Boltzmann distribution. *Right*: FWHM for a beam with Maxwell-Boltzmann distributed velocity. Red points symbolize calculated results, using equation 3.2. Green points stand for the FWHM of simulation results.

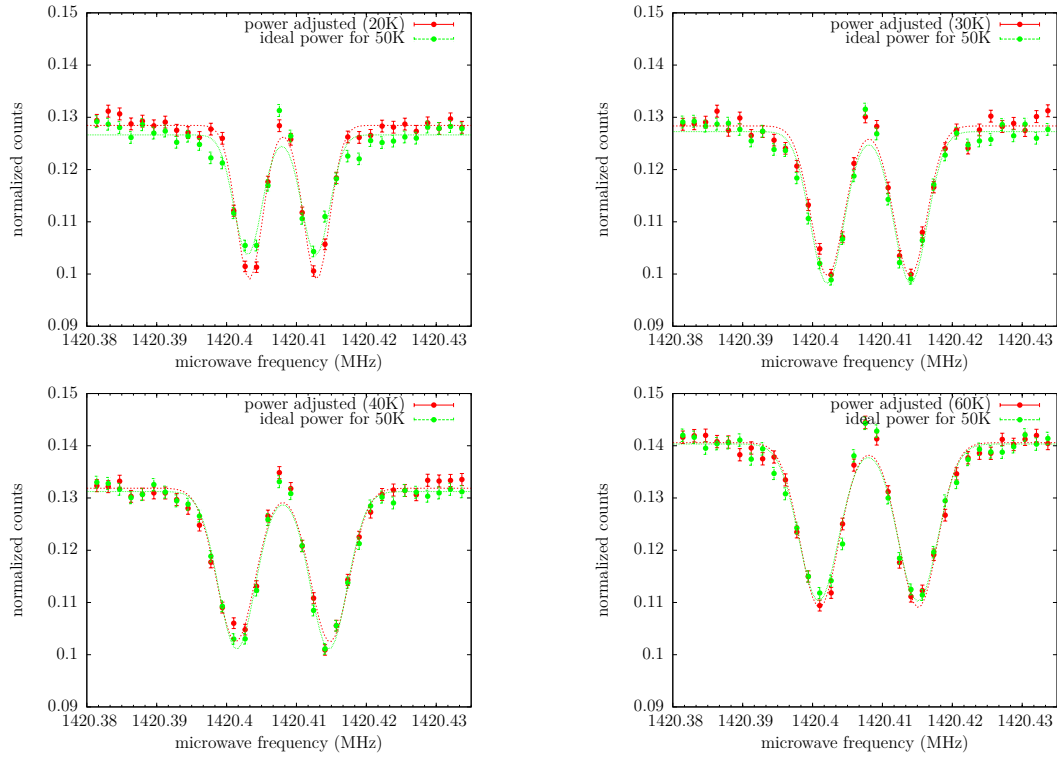


Figure 4.21: σ_1 scans for different temperatures. Red points represent simulations with power adjusted to the temperature, green points show results with power kept constant at power for 50 K (0.0374 W). 10^5 antihydrogen atoms per scan point were used and a polarization of 70 % LFS and 30 % HFS.

4.5.3 Dependence on Cavity Power

The effect of the cavity power on the resonance scans was studied and the resulting scans are shown in figure 4.21, 4.22 (σ_1) and 4.23 (π_1). Fit results can be found in the Appendix, see 6.2.

The power calculated for 50 K (≈ 0.03 W) via equations 4.39 and 4.50 was used for all temperatures (green points) and compared with simulation results using the adjusted power (red points). The static magnetic field was kept constant and without inhomogeneities.

The difference between these two results is barely visible. The peak width,

4 Simulation of the GSHFS Transitions of H/\bar{H}

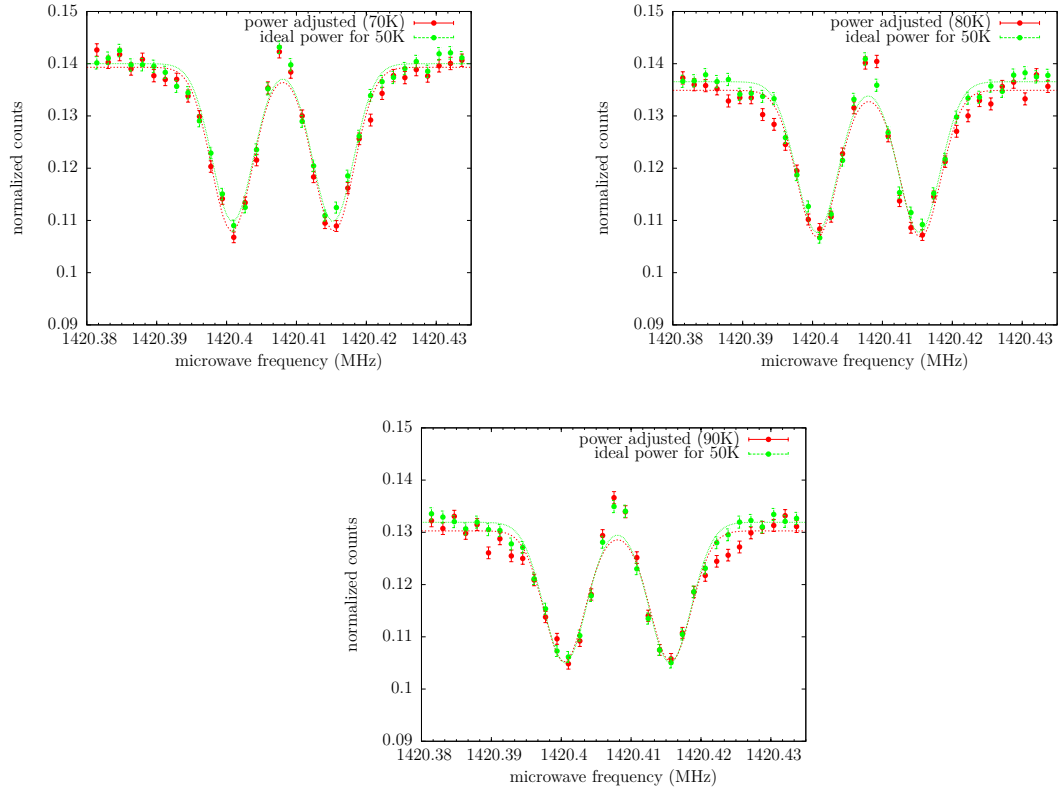


Figure 4.22: σ_1 scans for different temperatures. Red points represent simulations with power adjusted to the temperature, green points show results with power kept constant at power for 50 K. 10^5 anti hydrogen atoms per scan point were used and a polarization of 70 % LFS and 30 % HFS.

4 Simulation of the GSHFS Transitions of H/\bar{H}

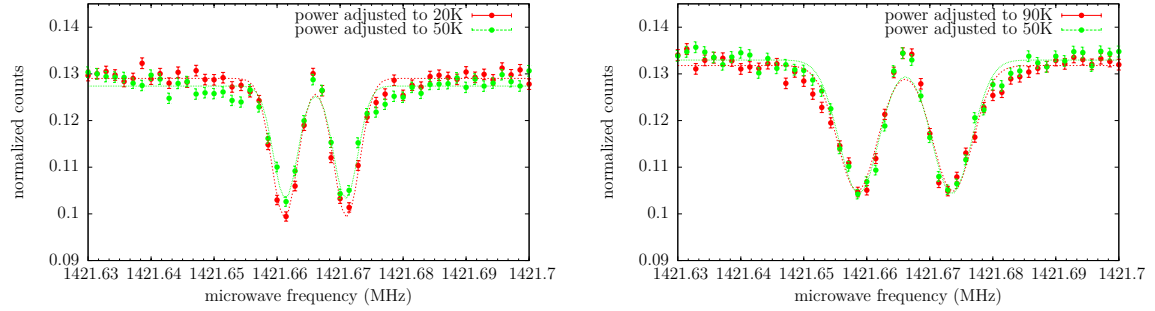


Figure 4.23: π_1 scans for different temperatures. Red points represent simulations with power adjusted to the temperature, green points show results with power kept at power for 50 K. 10^5 anti hydrogen atoms per scan point were used and a polarization of 70 % LFS and 30 % HFS.

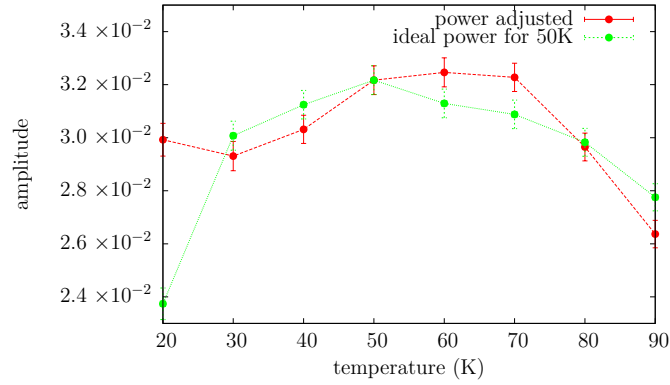


Figure 4.24: Peak amplitude of the two gaussians in dependence of the temperature for σ_1 scans with power kept constant (green) and power adjusted (red).

see figure 4.25, seems not to be very affected by the difference in power. Only for 20 K which is the lowest temperature used and the farthest away from 50 K a difference in peak amplitude (see figure 4.24) and fitting error of the central peak position (see figure 4.26) is noticeable. The same behaviour was found for simulation results of the π_1 transition, see for example resonance scans in figure 4.23.

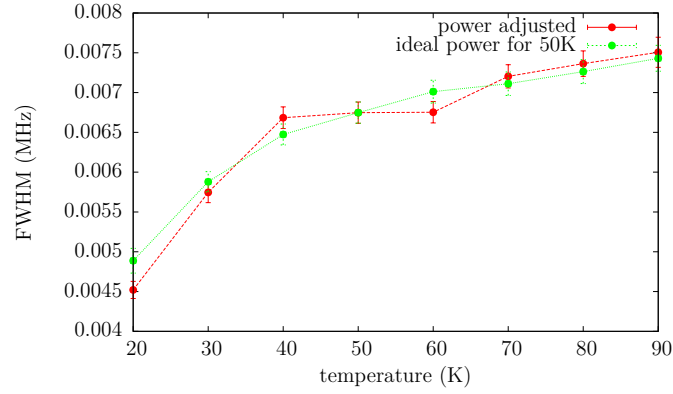


Figure 4.25: Peak width of the two gaussians in dependence of the temperature for σ_1 scans with power kept constant (green) and power adjusted (red).

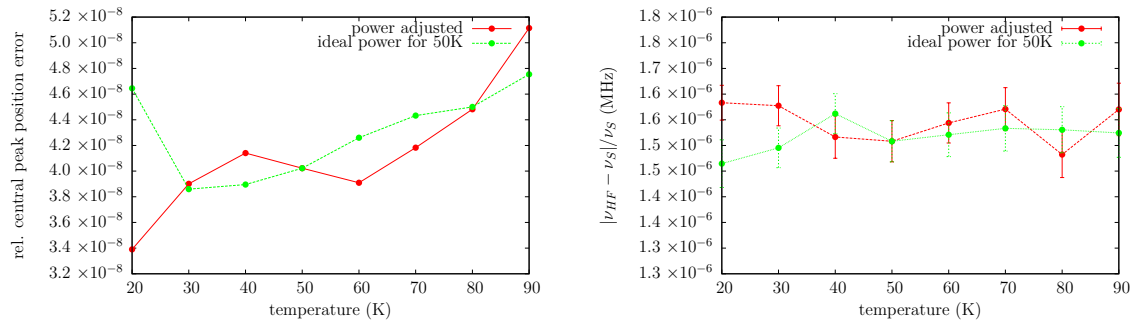


Figure 4.26: *Left*: Relative error of the central peak position in dependence of the temperature for the scans with power kept constant (green) and power adjusted (red). *Right*: Relative deviation of the simulated ν_S (obtained from simulated scans see e.g. figure 4.22) and the input frequency ν_{HF} (see equation 2.1). Errorbars are calculated by gaussian error propagation.

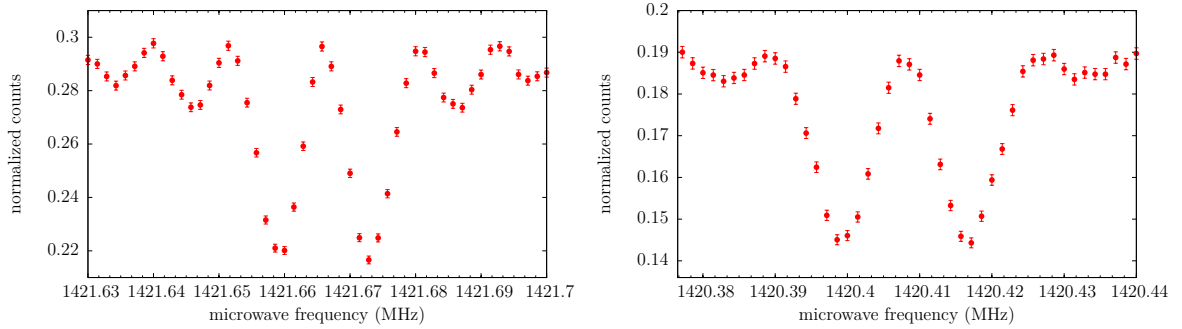


Figure 4.27: Scans of the π_1 (left) and the σ_1 (right) transition with a field of zero inhomogeneity with a beam of 10^5 monoenergetic (0.01 eV) antihydrogen atoms and a polarization of 70 % LFS and 30 % HFS.

4.5.4 Dependence on Inhomogeneity of the Static Magnetic Field

In the following the effect of inhomogeneities of the static magnetic field on the resonance scans of both transitions will be studied. The focus will be on the π_1 transition which is very sensitive to homogeneities. All plotted fit results can be found in the Appendix, see 6.3.

Again, high statistics will be used and a monoenergetic beam as well as a beam with Maxwell-Boltzmann distributed velocity. Measured and simulated fieldmaps will be used, their histograms are shown in figures 4.29 and 4.28. For comparison, scans with a completely homogeneous field are displayed in figure 4.27.

The scans in figure 4.30 show the simulation results of the π_1 transition using gaussian distributed fieldmaps for the static magnetic field with different standard deviation σ (expressed as a percentage of the mean value), for histograms with different σ see figure 4.28.

The label at the bottom right represents the σ used with respect to the mean value. For comparison, the last plot on the right shows the π_1 scan using a measured fieldmap. Red points symbolize results using antihydrogen atoms with Maxwell-Boltzmann distributed velocity and green points results with a monovelocity beam. Note again, that in all scan plots a downward shift was applied to the monovelocity scan in order to allow better comparison.

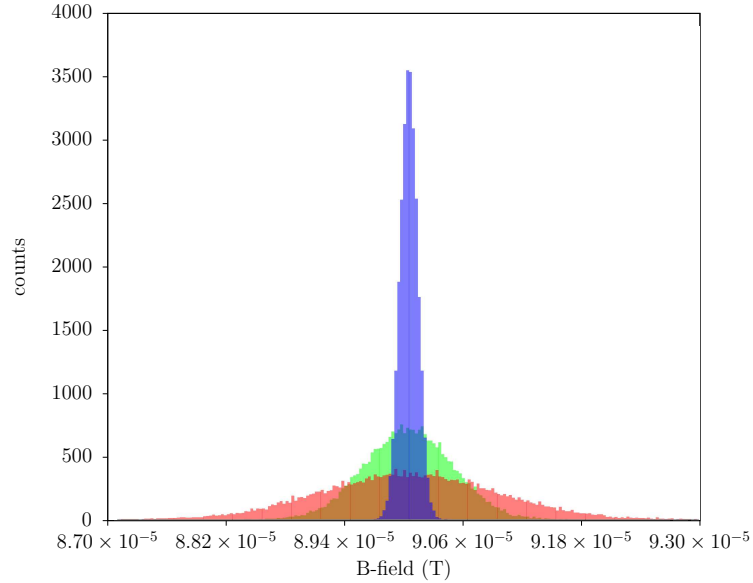


Figure 4.28: Histograms of the gaussian distributed fieldmaps with different σ used to study the influence of inhomogeneity on the resonance scans.

Figure 4.31 shows the same for the σ_1 transition. One can see, that the effect of the inhomogeneity on the σ_1 scans is barely visible - only the side maxima fade a little. While the π_1 scan is hardly visible at 0.5 %, one still can see side maxima of the σ_1 even at 10 %.

The parameters of the fit are analyzed in plots 4.32 to 4.34. As expected, for the π_1 transition the fitting error of the central peak position (fig. 4.32) increases with inhomogeneity. The offset of green and red points grows with inhomogeneity. The blue line represents the error of the fit using a completely homogeneous field. With increasing σ , first the side maxima and then the double peak structure wash out gradually.

For the σ_1 transitions, the fitting error of ν_{σ_1} has a small offset comparing monovelocity beam and MB beam which barely changes with increasing σ .

Regarding the FWHM of the fitted gaussian peaks for the π_1 transitions, one sees that it increases with inhomogeneity as well (figure 4.33). For decreasing σ , the FWHM approaches the zero inhomogeneity result. Also, the width seems not to be much affected by having a beam with 50 K instead of a

4 Simulation of the GSHFS Transitions of H/\bar{H}

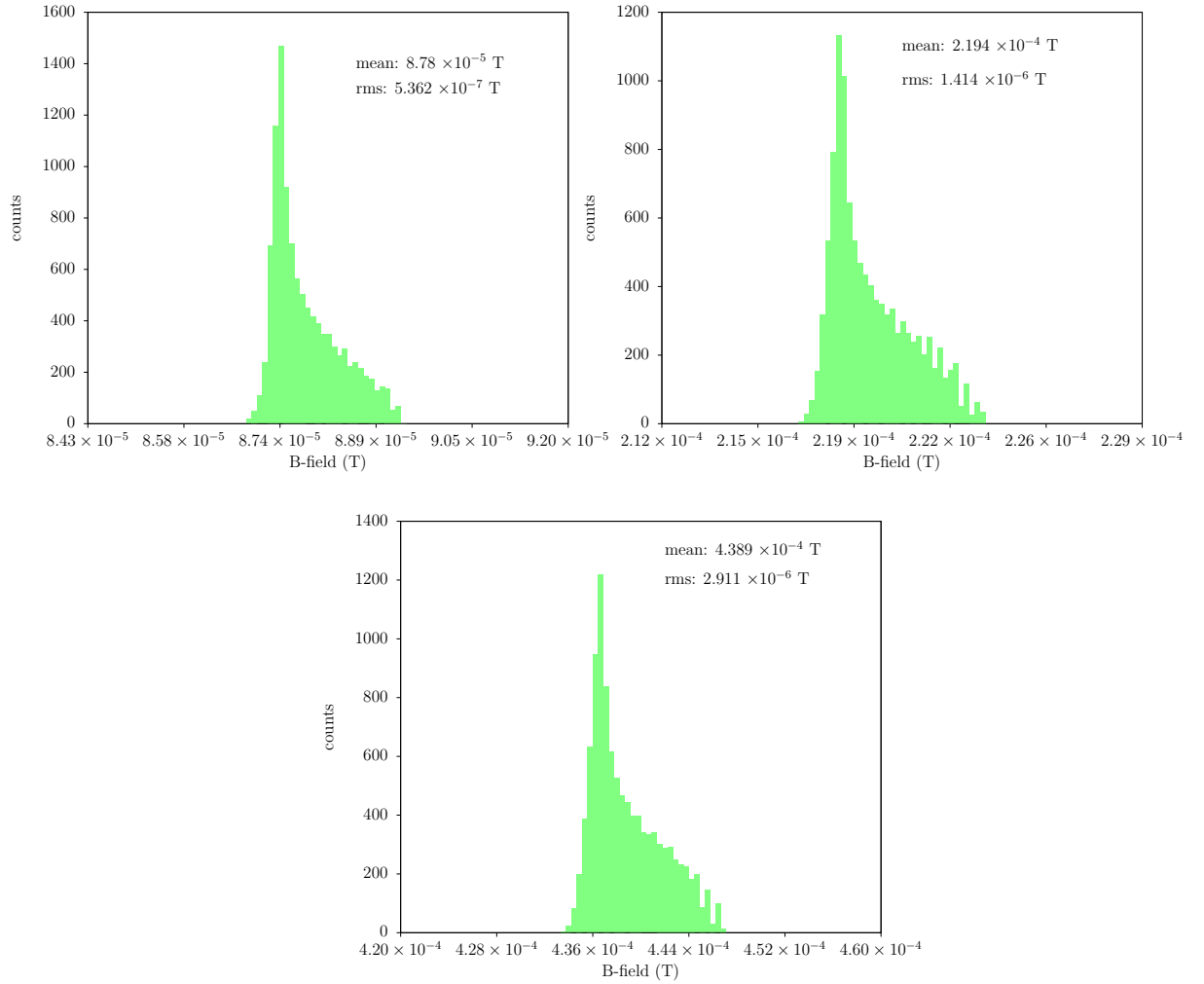


Figure 4.29: Histograms for the measured fieldmaps with different field strengths used for the simulations.

4 Simulation of the GSHFS Transitions of H/\bar{H}

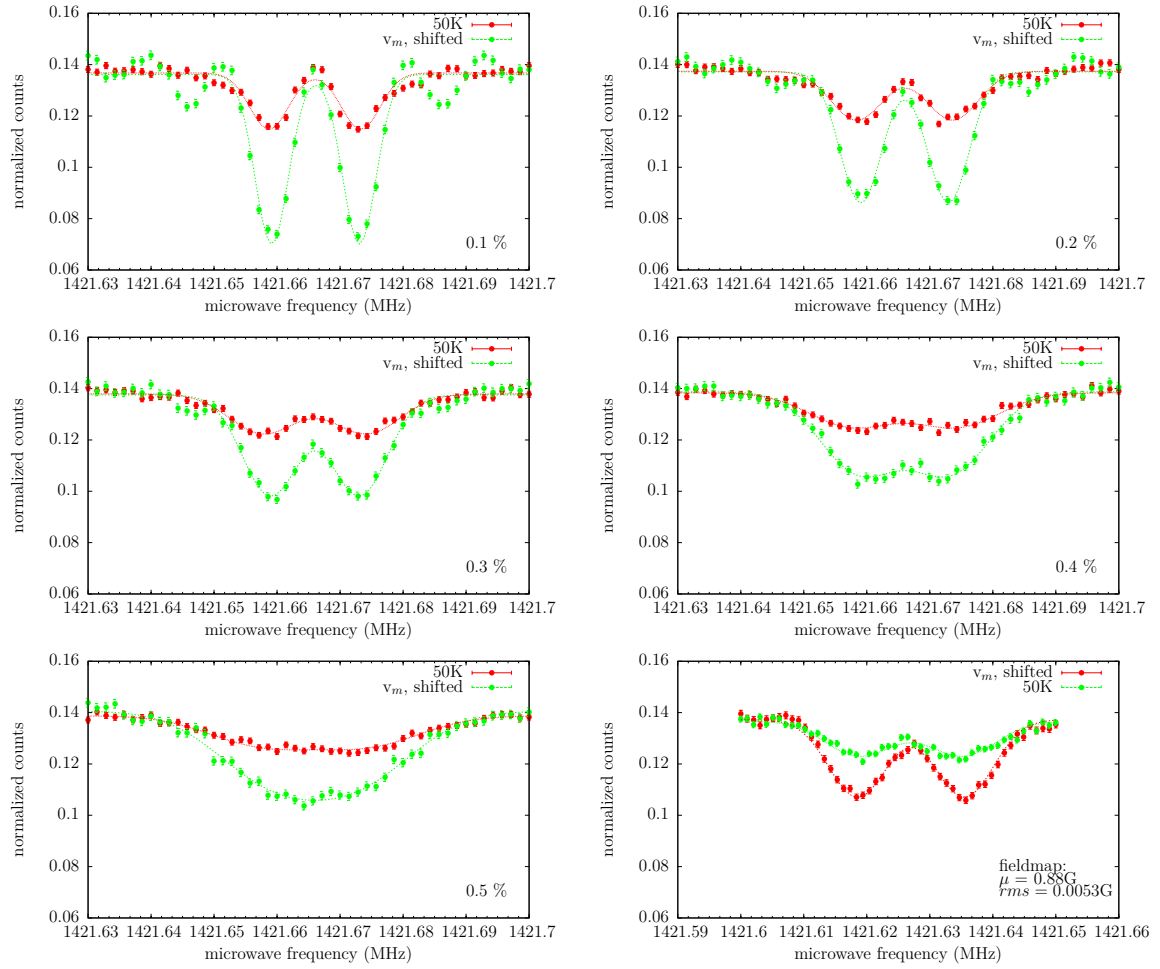


Figure 4.30: scans of the π_1 transition with a gaussian distributed static B-field with different inhomogeneities (the label at the bottom right denotes the standard deviation expressed as percentage of the mean value). Green points represent results with a beam of constant velocity and red points of a beam with Maxwell-Boltzmann distributed velocity. For better comparison, the spectra of the monovelocity beam are shifted to be on the same level with the 50 K results. A beam with 10^5 antihydrogen atoms per scan point and a polarization of 70 % LFS and 30 % HFS was used. For comparison, the plot in the bottom right shows a scans with a measured fieldmap used.

4 Simulation of the GSHFS Transitions of H/\bar{H}

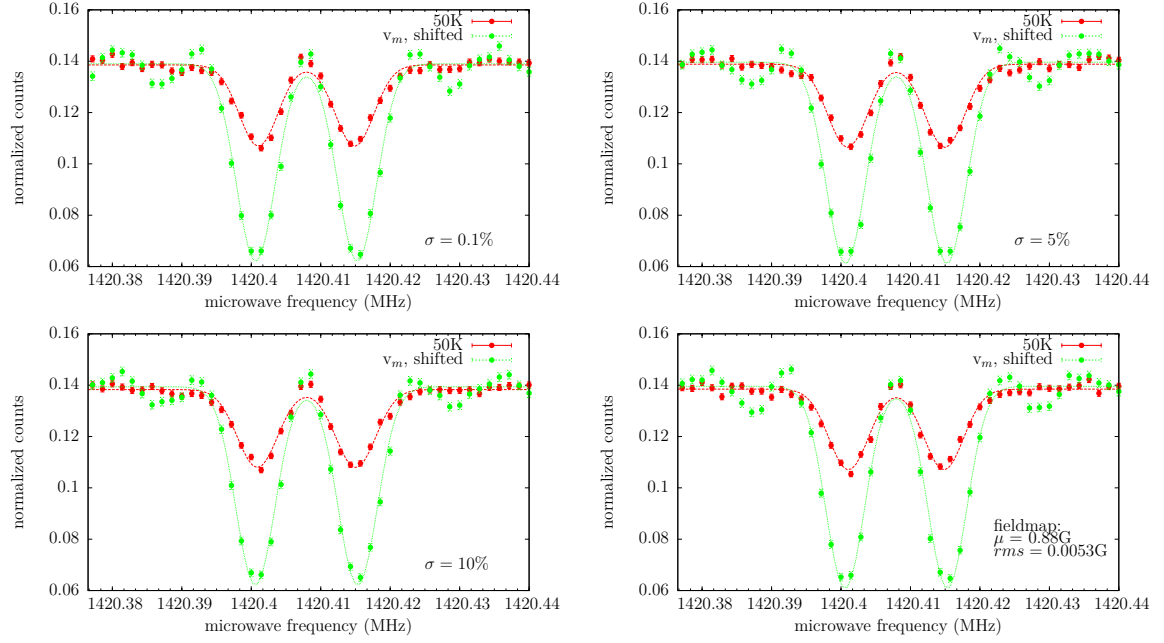


Figure 4.31: scans of the σ_1 transition with a gaussian distributed static B-field with different inhomogeneities (the label at the bottom right denotes the standard deviation expressed as a percentage of the mean value). For better comparison, the spectra of the monovelocity beam are shifted to be on the same level with the 50 K results. A beam with 10^5 anti hydrogen atoms per scan point and a polarization of 70 % LFS and 30 % HFS was used. For comparison, the plot in the bottom right shows a scans with a measured fieldmap used.

monoenergetic one.

Note that for the σ_1 for reasons of visibility the range of the y-axis is not the same as for the π_1 plot. The increasing inhomogeneity has only a very small effect on the FWHM.

In figure 4.34 the peak amplitude is shown in dependence of the inhomogeneity. Looking at the π_1 results, one observes a decrease in amplitude with increasing σ as the scan washes out. Again, one may notice the offset between the results of the 50 K beam and the monoenergetic beam which decreases with inhomogeneity.

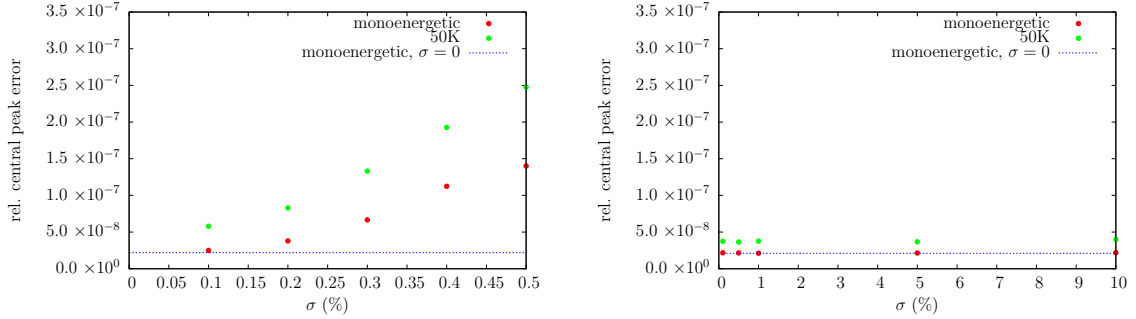


Figure 4.32: Error of the central peak position in dependence of inhomogeneity for π_1 (left) and σ_1 (right) scans with velocity v_m (red) and Boltzmann distributed velocity (red). The blue line shows the central peak error of a scan with zero inhomogeneity. The same range for the y-axis was chosen for comparison.

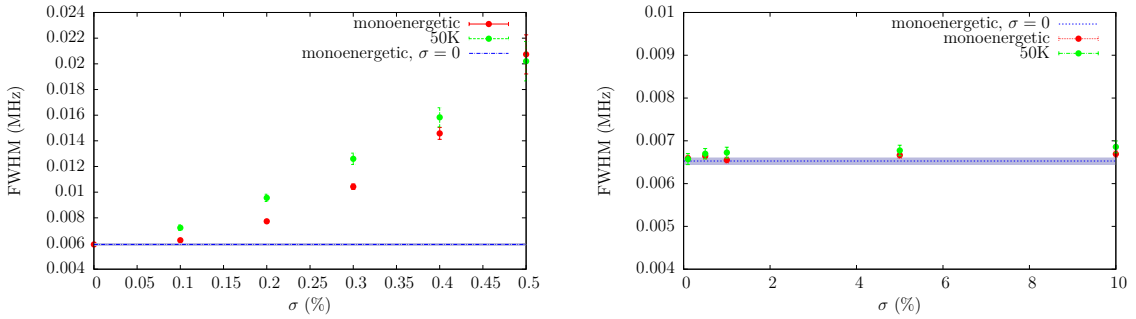


Figure 4.33: FWHM in dependence of inhomogeneity for π_1 (left) and σ_1 (right) scans with velocity v_m (red) and Maxwell-Boltzmann distributed velocity (red). The blue line shows the FWHM of a gauss peak of the scan with zero inhomogeneity.

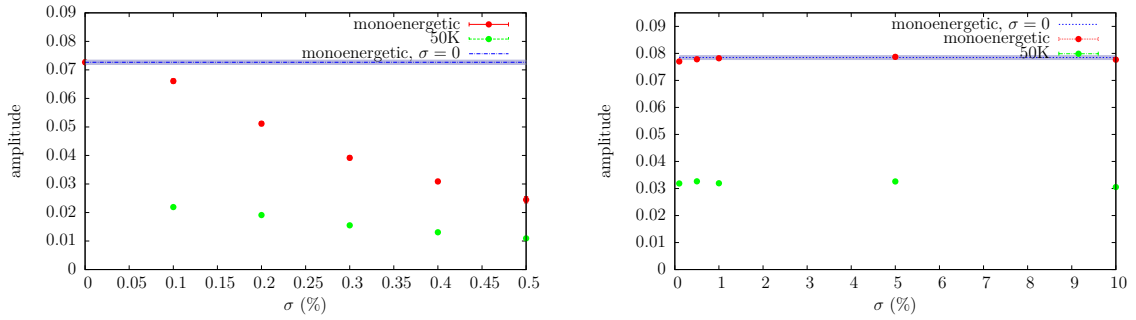


Figure 4.34: Peak amplitude in dependence of inhomogeneity for π_1 (left) and σ_1 (right) scans with velocity v_m (red) and Maxwell-Boltzmann distributed velocity (green). The blue line shows the peak fitting error of a scan with zero inhomogeneity.

For fitting results of the amplitude of the σ_1 scans also have the offset between results of monovelocity and MB beam, but it stays approximately the same for increasing inhomogeneity.

4.5.5 Dependence on Statistics

Since the production rate of antihydrogen is expected to be low, the study of scans and scan parameters in dependence of the number of antihydrogen atoms per scan point might provide insightful information.

In the following the effect of particle statistics on the σ_1 transition is investigated using a 50 K beam and different measured fieldmaps in order to allow an extrapolation to zero field for different particle numbers per scan point.

The outcoming scans are shown in figures 4.35 to 4.40 and for quantitative fit results, see Appendix 6.4.

The number of atoms per scan point N_0 ranges from 600 to 2000 in steps of 100 particles. Down to $N_0 = 900$ the resonance structure is clearly visible. Beneath that, the fitting algorithm still seems to find the two gaussian peaks but they are hardly visible to the naked eye.

In figure 4.41, the extrapolation for $N_0 = 600, 1000$ and 2000 antihydrogen atoms is shown as an example and the resulting fitting error and relative error for the transition frequency at 0 magnetic field for all statistics can be seen in figure 4.42. As expected, the error increases with decreasing N_0 . Figure 4.43 shows deviation and relative deviation from the measured hyperfine transition frequency (see 2.1).

4 Simulation of the GSHFS Transitions of H/\bar{H}

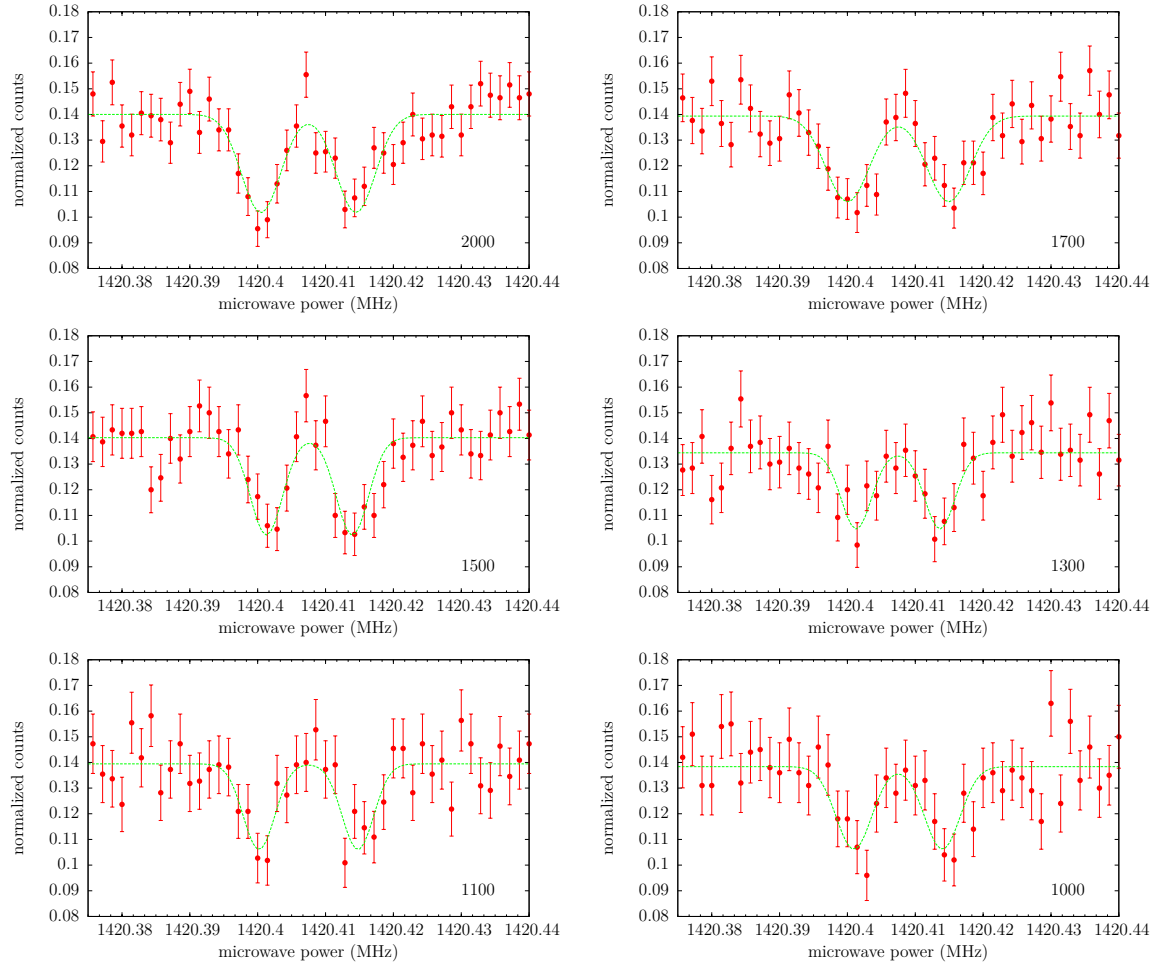


Figure 4.35: Scans of the σ_1 transition with different number of particles per scan point (see right bottom corner of plots). Green lines show the fit of the simulated data. A fieldmap with $\mu = 0.88$ G and $rms = 0.0053$ G was used, as well as a beam polarization of 70 % LFS and 30 % HFS.

4 Simulation of the GSHFS Transitions of H/\bar{H}

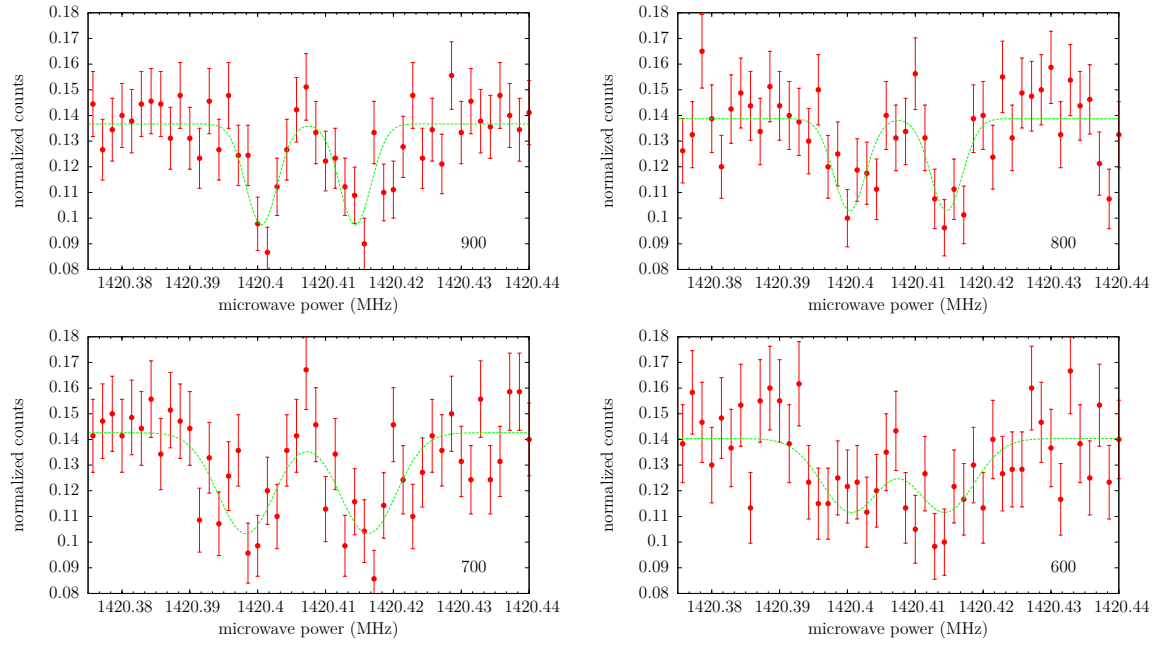


Figure 4.36: Scans of the σ_1 transition with different number of particles per scan point (see right bottom corner of plots). Green lines show the fit of the simulated data. A fieldmap with $\mu = 0.88$ G and $rms = 0.0053$ G was used, as well as a beam polarization of 70 % LFS and 30 % HFS.

4 Simulation of the GSHFS Transitions of H/\bar{H}

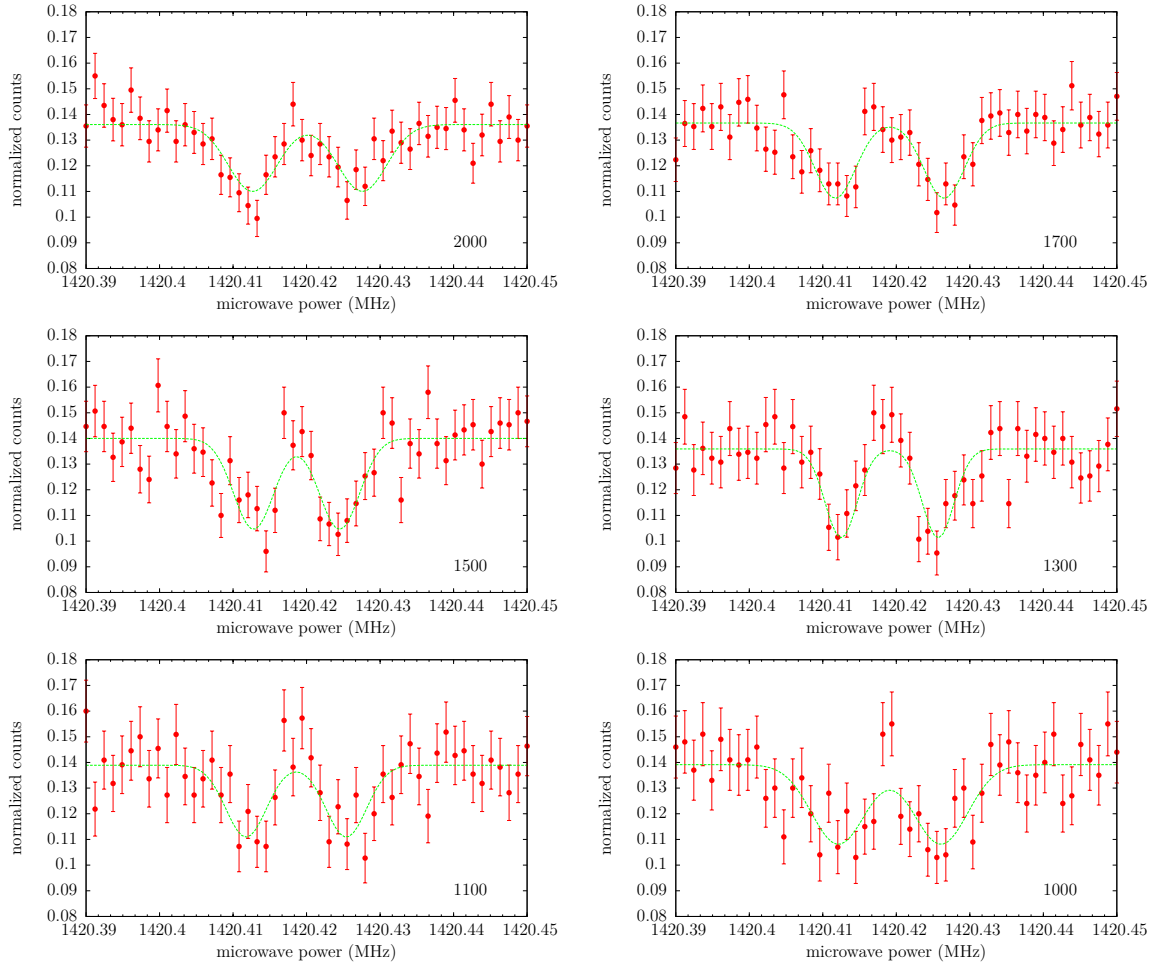


Figure 4.37: Scans of the σ_1 transition with different number of particles per scan point (see right bottom corner of plots). Green lines show the fit of the simulated data. A fieldmap with $\mu = 2.19$ G and $rms = 0.014$ G was used, as well as a beam polarization of 70 % LFS and 30 % HFS.

4 Simulation of the GSHFS Transitions of H/\bar{H}

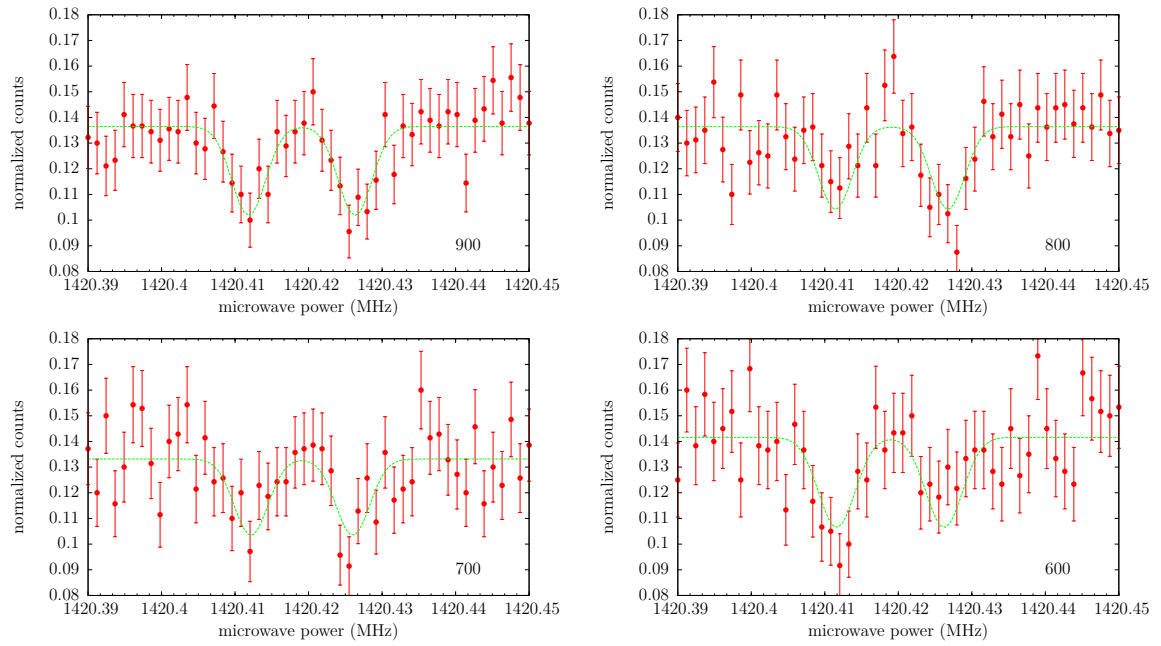


Figure 4.38: Scans of the σ_1 transition with different number of particles per scan point (see right bottom corner of plots). Green lines show the fit of the simulated data. A fieldmap with $\mu = 2.19$ G and $rms = 0.014$ G was used, as well as a beam polarization of 70 % LFS and 30 % HFS.

4 Simulation of the GSHFS Transitions of H/\bar{H}

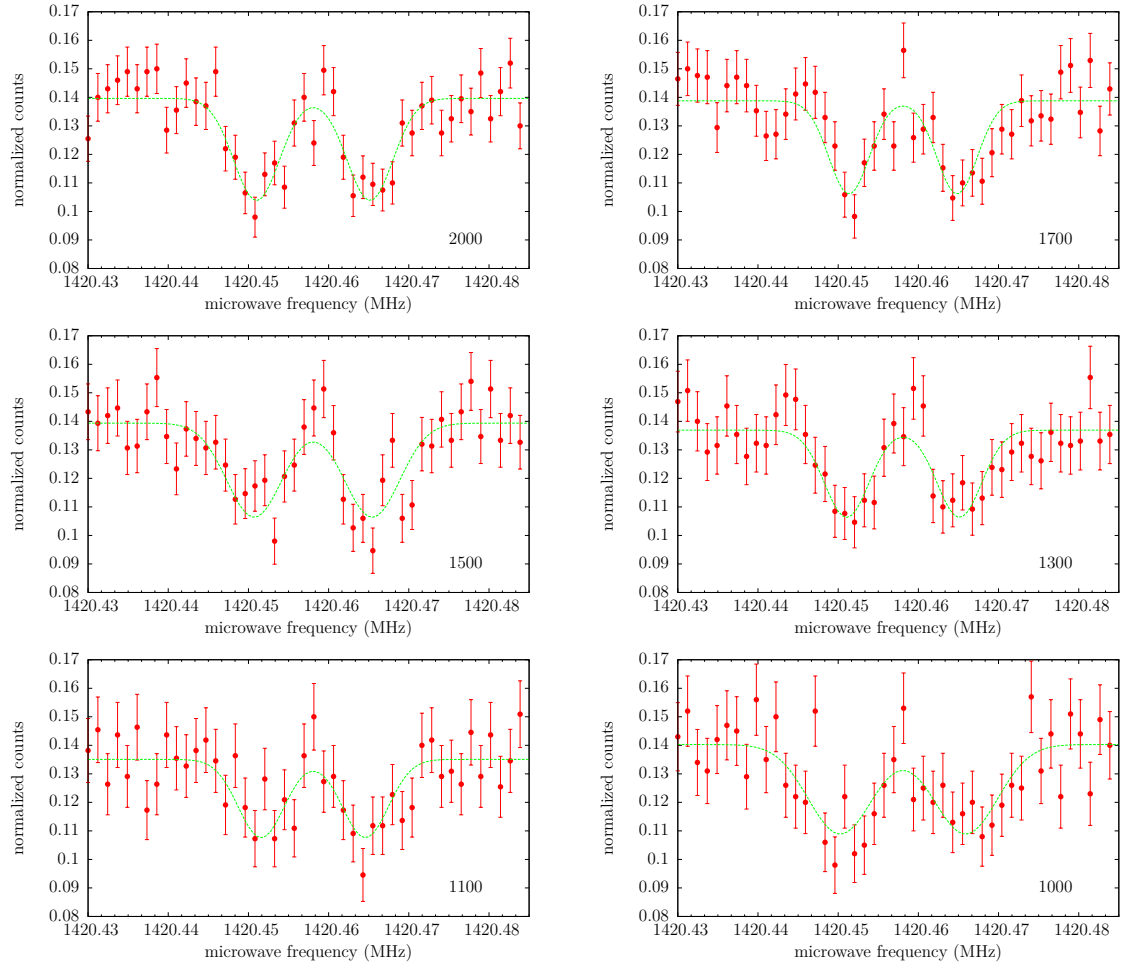


Figure 4.39: Scans of the σ_1 transition with different number of particles per scan point (see right bottom corner of plots). Green lines show the fit of the simulated data. A fieldmap with $\mu = 4.39$ G and $rms = 0.029$ G was used, as well as a beam polarization of 70 % LFS and 30 % HFS.

4 Simulation of the GSHFS Transitions of H/\bar{H}

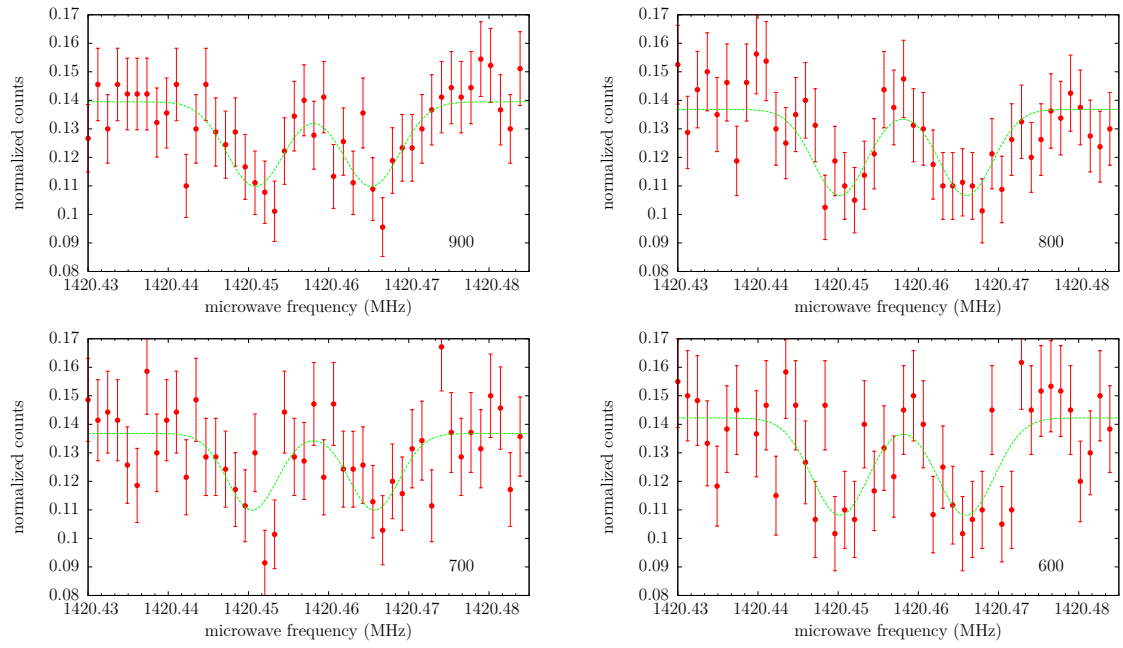


Figure 4.40: Scans of the σ_1 transition with different number of particles per scan point (see right bottom corner of plots). Green lines show the fit of the simulated data. A fieldmap with $\mu = 4.39$ G and $rms = 0.029$ G was used, as well as a beam polarization of 70 % LFS and 30 % HFS.

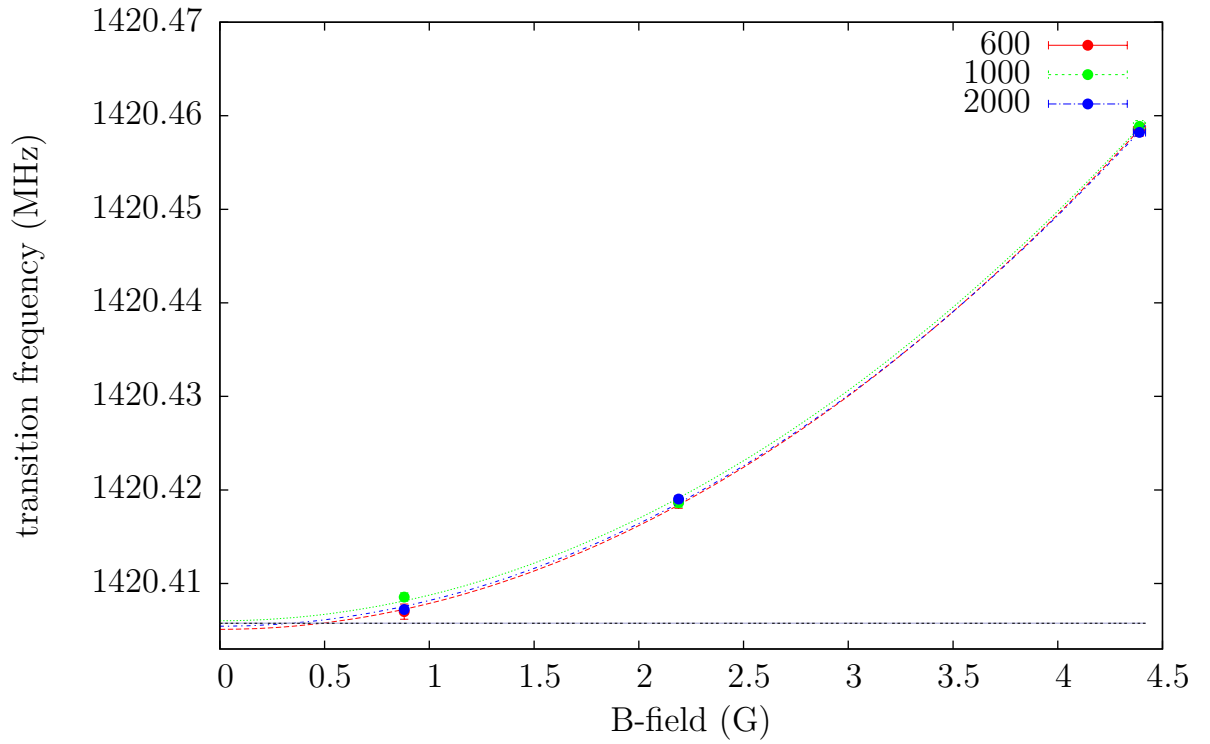


Figure 4.41: Zero field extrapolation for different numbers of antihydrogen atoms per scan point: 600 \bar{H} (red), 1000 \bar{H} (green), 2000 \bar{H} (blue). Equation 4.61 was used to fit the simulated data.

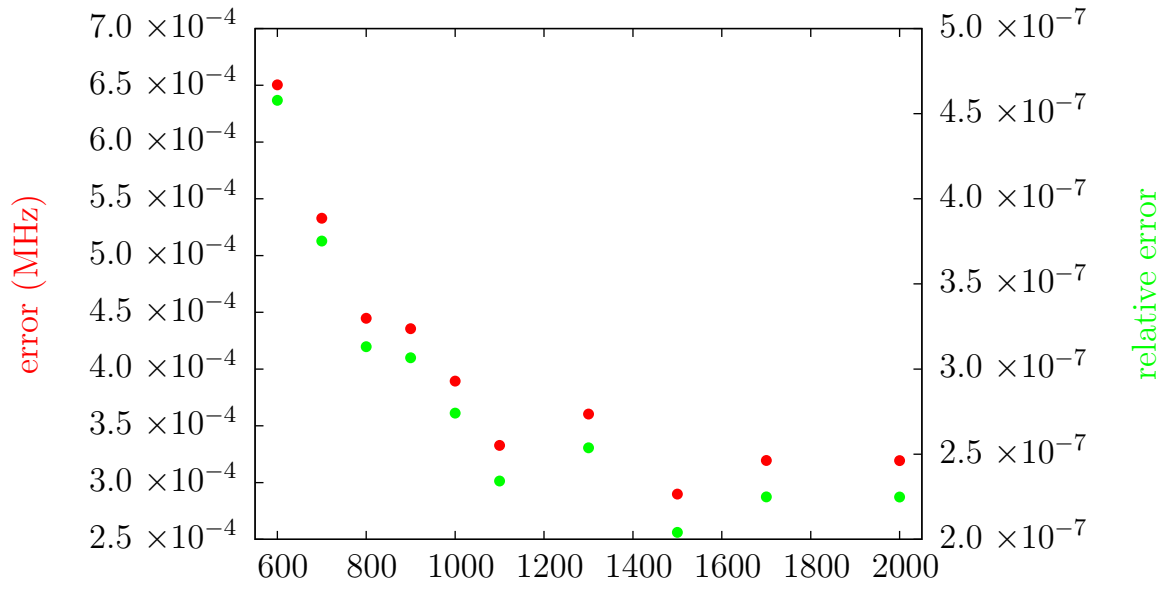


Figure 4.42: Error and relative error of ν_0 determined by extrapolation to zero B-field in dependence of number of particles per scan point used.

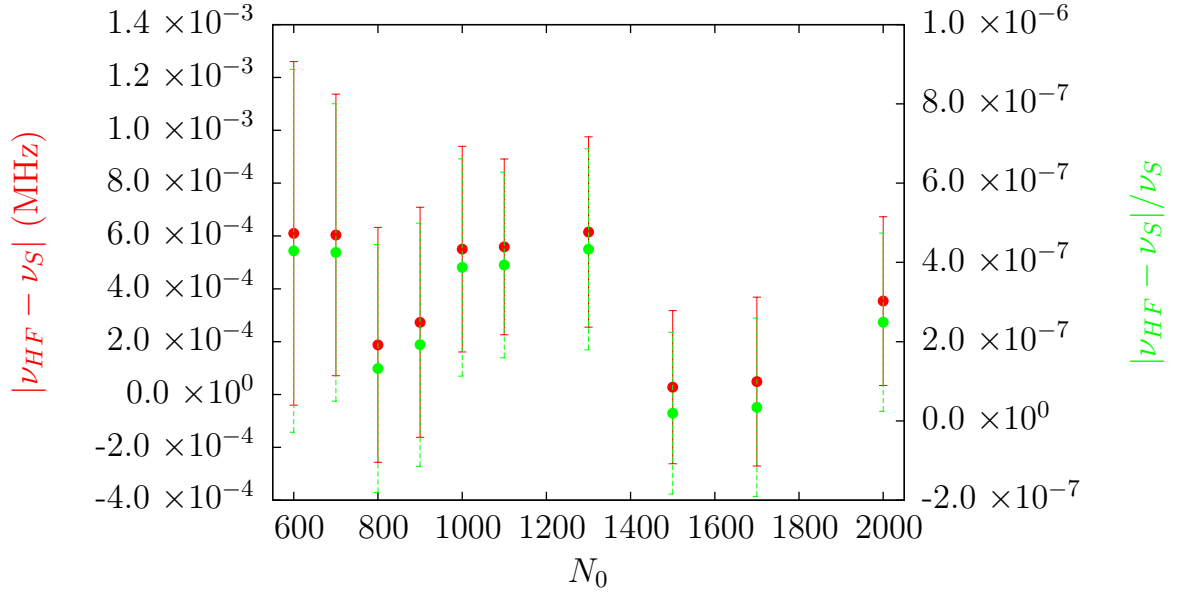


Figure 4.43: Deviation (red dots) and relative deviation (green dots) of ν_0 determined by extrapolation to zero B-field in dependence of number of particles per scan point used. The frequency ν_{HF} denotes the input frequency and ν_S the simulated hyperfine transition frequency obtained by fits. Errorbars are obtained by gaussian error propagation.

| transition | transition frequency (MHz) | error (MHz) |
|------------|----------------------------|---------------------------|
| σ_1 | 1420.407847499 | 5.372197×10^{-5} |
| π_1 | 1421.627406724 | 1.93374×10^{-4} |

Table 4.3: Transition frequencies and errors obtained from fit for: $\mu_B = 0.88$ G and $rms_B = 0.0053$ G, $N_{\bar{H}} = 10^5$, angle between fields of 0° and 90° , polarisation of 70% LFS, 30% HFS and Maxwell-Boltzmann distributed beam with 50 K.

4.5.6 Transition Frequency at Zero Magnetic Field

In the following section, the two different methods to obtain the transition frequency at zero static magnetic field will be discussed and compared.

... using σ_1 and π_1 transition at the same B-field

In order to determine the σ_1 and π_1 transition frequency and study the effect of different Helmholtz coil configurations, the following resonance scans were done.

First of all, a beam with Maxwell-Boltzmann distributed velocity at 50 K and a field angle of 0° for the σ_1 and 90° for the π_1 transition was used which resulted in the scans shown in figure 4.44. The transition frequencies obtained by fit are listed in table 4.3. Using the following equation, the transition frequency at zero field was obtained:

$$\nu_0 = \frac{g_+ \sqrt{g_+ \nu_\sigma^2 - 4g_-^2 \nu_\pi^2 + 4g_- \nu_\pi \nu_\sigma} + g_-^2 (2\nu_\pi - \nu_\sigma)}{g_+^2 + g_-^2} \quad (4.56)$$

where $g_\pm = g_I \pm g_J$. This formula was obtained using the Breit-Rabi formulae for the two transitions. One gets for ν_0 :

$$\nu_0 = 1420.405\,762\,404\,2 \text{ MHz} \pm 5.3910 \times 10^{-5} \text{ MHz} \quad (4.57)$$

and a deviation from the measured value (see 2.1) of $1.063\,75 \times 10^{-5}$ MHz. The relative error is:

$$e_r = 3.795\,39 \times 10^{-8} \quad (4.58)$$

4 Simulation of the GSHFS Transitions of H/\bar{H}

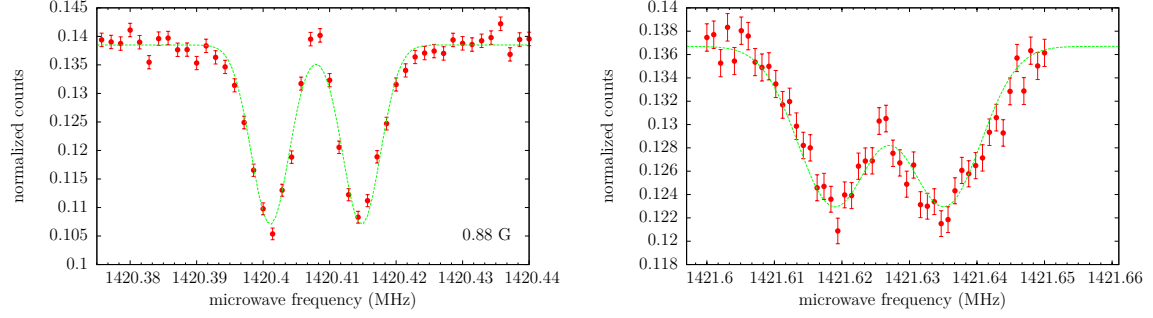


Figure 4.44: The σ_1 and π_1 transitions with an angle of 0° and 90° respectively between static and oscillating magnetic field, a B-field with $\mu = 0.88$ G and $\sigma = 0.0053$ G (fieldmap), a beam with boltzmann distributed velocities and 50K, a polarization of 70% LFS and 30% HFS.

| transition | transition frequency (MHz) | error (MHz) |
|------------|----------------------------|--------------------------|
| σ_1 | 1420.407849839 | 7.52806×10^{-5} |
| π_1 | 1421.627295345 | 1.49478×10^{-4} |

Table 4.4: Transition frequencies and errors obtained from fit for: $\mu_B = 0.88$ G and $\sigma_B = 0.0053$ G, $N_{\bar{H}} = 10^5$, angle between fields of 45° for both, polarisation of 70% LFS, 30% HFS and Boltzmann distributed beam with 50K.

and the relative deviation 7.48906×10^{-9} .

Using a coil configuration of 45° for both transitions and a 50 K beam, one gets for ν_0 :

$$\nu_0 = 1420.405765133 \text{ MHz} \pm 7.5540 \times 10^{-5} \text{ MHz} \quad (4.59)$$

a deviation from the measured value (see 2.1) of 1.33663×10^{-5} MHz and a relative error of:

$$e_r = 5.31820 \times 10^{-8} \quad (4.60)$$

The relative deviation is 9.41020×10^{-9} .

Plots of the scans and frequencies are shown in figure 4.45 and table 4.4.

4 Simulation of the GSHFS Transitions of H/\bar{H}

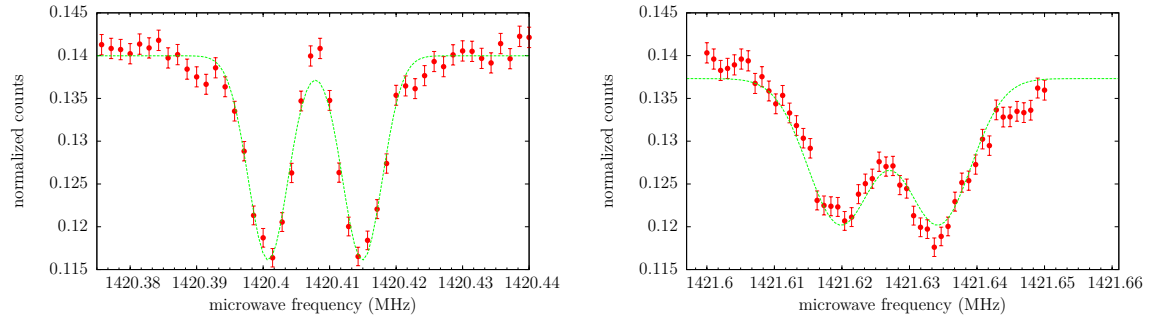


Figure 4.45: The σ_1 and π_1 transitions with an angle of 45° between static and oscillating magnetic field, a B-field with $\mu = 0.88$ G and $rms = 0.0053$ G (fieldmap), a beam with boltzmann distributed velocities and 50 K, a polarization of 70% LFS and 30% HFS.

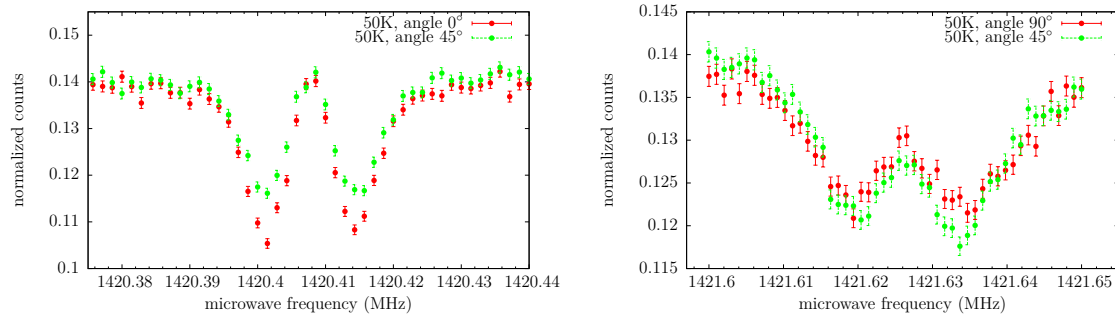


Figure 4.46: Comparison of the σ_1 (left) and π_1 (right) transition scans from figures 4.44 and 4.45.

In order to better compare the scans, figure 4.46 shows the above scans in one plot. Switching from an angle of 0° to 45° between static and oscillating field, the peak amplitude decreases slightly. This effect seems to affect the σ_1 transition more than the π_1 transition. It might be a consequence of the additional transitions with $\Delta m_F = \pm 1$ which will not be excited using a 0° configuration.

Furhtermore, a peak asymmetry for the π_1 transtion seems to arise when switching from 90° to 45° angle. At the moment, this cannot be explained.

... using the σ_1 transition at different B-fields

The simulated resonance scans of the σ_1 transition at different static magnetic field strength can be found in figure 4.47. An angle of 0° between oscillating and static B-field was used and otherwise the same conditions as for results in figure 4.45 in order to allow comparison.

The extrapolation formula (Breit-Rabi formula):

$$\nu_{\sigma_1} = \nu_0 \sqrt{1 + x^2} \quad (4.61)$$

was used in order to determine the zero field transition frequency. The plot can be seen in figure 4.48 and for ν_0 one gets:

$$\nu_0 = 1420.405\,727\,132 \text{ MHz} \pm 6.7691 \times 10^{-5} \text{ MHz} \quad (4.62)$$

a deviation from the measured value (see 2.1) of $2.463\,47 \times 10^{-5}$ MHz and a relative error of:

$$e_r = 4.765\,61 \times 10^{-8} \quad (4.63)$$

The relative deviation is $1.734\,34 \times 10^{-8}$.

Comparing now the results of the two methods to determine ν_0 , the error of the second one is higher by a factor of 1.12.

The question arises which N_0 for the two methods is needed in order to reach approximately the same error. In order to persue this question, scans for the σ_1 and π_1 transition have been done using $N_0 = 6000$ which is the number of particles per scan point where the sensitive π_1 transition becomes clear. A calculation yields:

$$\nu_0 = 1420.405\,988\,741 \text{ MHz} \pm 3.099\,85 \times 10^{-4} \text{ MHz} \quad (4.64)$$

a deviation from the measured value (see 2.1) of $2.369\,743 \times 10^{-4}$ MHz and a relative error of:

$$e_r = 2.182\,37 \times 10^{-7} \quad (4.65)$$

The relative deviation is $1.668\,356 \times 10^{-7}$.

4 Simulation of the GSHFS Transitions of H/\bar{H}

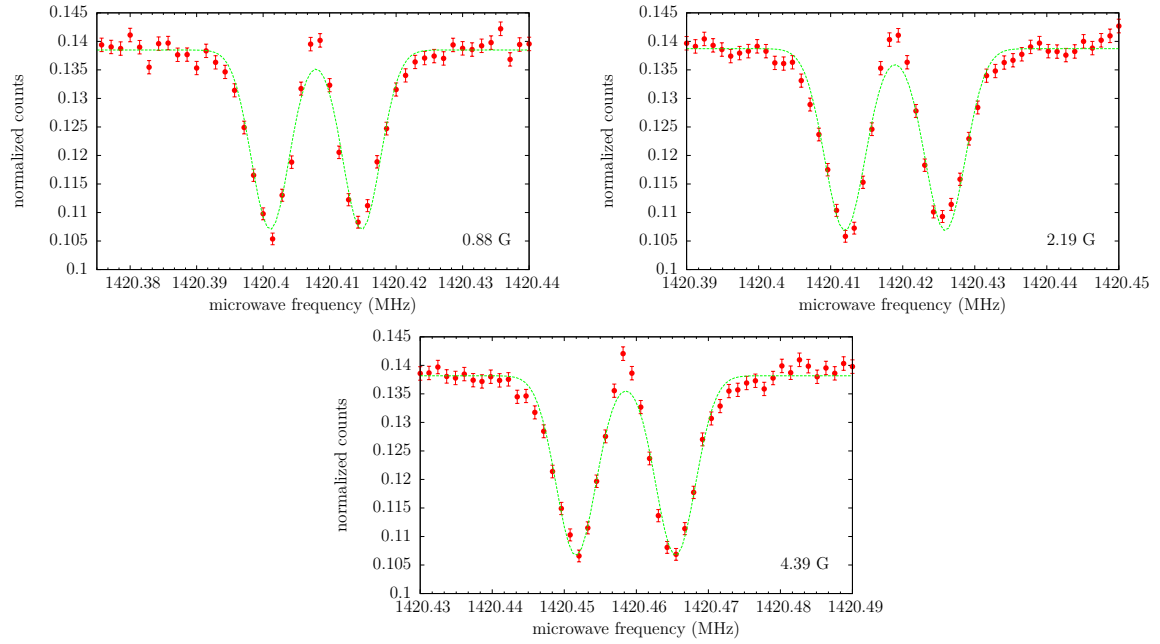


Figure 4.47: σ_1 scans at different magnetic field strength, an angle between fields of 0° , polarisation of 70% LFS, 30% HFS, 10^5 particles per scan point and a Boltzmann distributed beam with 50K.

When trying to compare this method with the extrapolation to zero field using only the σ_1 transition, the influence of the inhomogeneity of the static magnetic field on the π_1 transition shows. Using a N_0 of 6000 as well, we get a result of:

$$\nu_0 = 1420.405\,674\,332\text{ MHz} \pm 2.253\,98 \times 10^{-4}\text{ MHz} \quad (4.66)$$

a deviation from the measured value (see 2.1) of $7.743\,47 \times 10^{-5}$ MHz and a relative error of:

$$e_r = 1.586\,86 \times 10^{-7} \quad (4.67)$$

The relative deviation is $5.451\,59 \times 10^{-8}$.

So using $N_0 = 6000$ and the current fieldmaps, the second method shows a lower error which at first glance seems to be in disagreement with the result

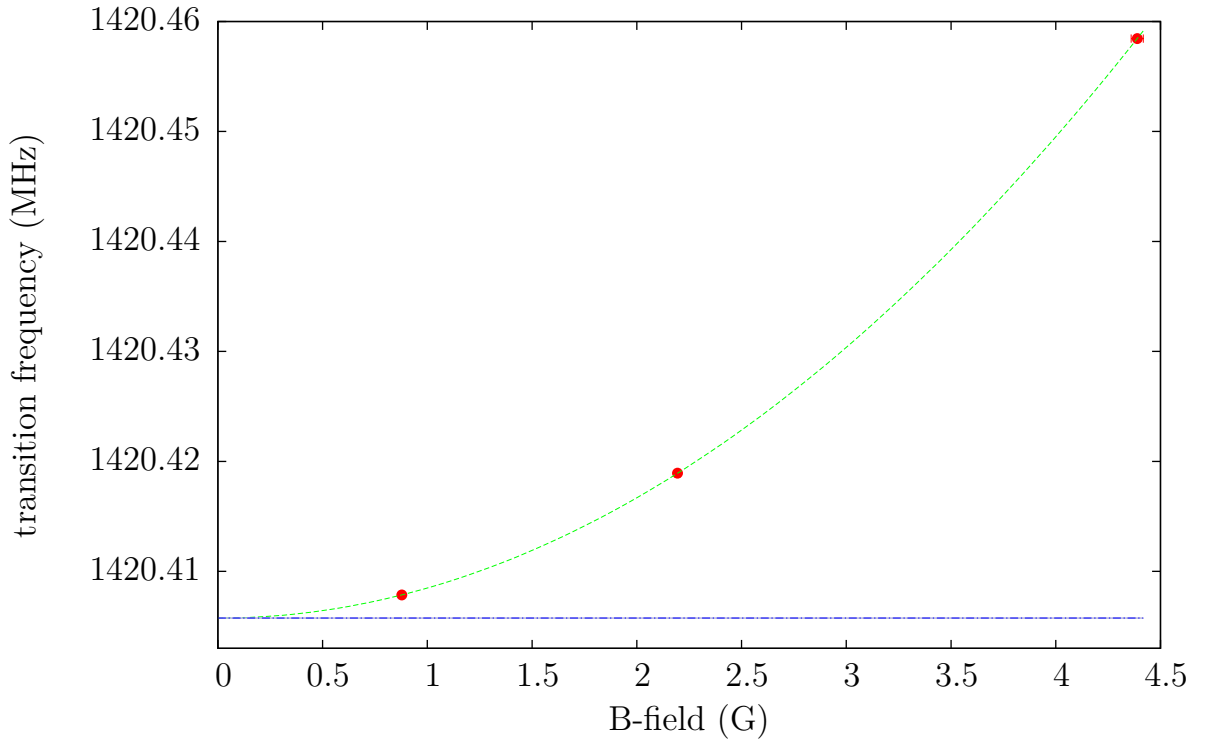


Figure 4.48: Extrapolation to zero B-field using the σ_1 scans from figure 4.47. Errorbars for both B-field and transition frequency are plotted, though barely visible due to the small size.

at higher statistics.

Considering the effect of field inhomogenieties on the π_1 transition, the most likely explanation is that in order to reach lower errors the static magnetic field needs to be more homogeneous. Otherwise the error of ν_π is too large and the method using both transitions becomes superior only for higher statistics and/or a more homogeneous magnetic field.

5 Summary and Outlook

The results and implementation of numerical simulations of hyperfine transitions of antihydrogen within the Geant4 framework using the ASACUSA setup has been discussed.

An estimation of the power for the σ_1 and π_1 transitions has been calculated and tested using the spin flip algorithm and good agreement has been found.

The influence of particle velocity within the beam on the resonance scans has been examined. Comparing a monovelocity beam to a beam with Maxwell-Boltzmann distributed velocity showed that with the monovelocity beam the particle number reaching the detector was about 2.3 times higher which is a result of the focusing effect of the sextupole magnet. Also, the amplitude was about 2.5 times higher, whereas the FWHM was not affected by the MB distribution of velocity.

The study of the effect of cavity power on the scans yields that small changes of power do not affect the scans, which is probably because of the broad peak around the velocity of choice in figures 4.8 and 4.9.

An investigation of the impact of inhomogeneities of the static magnetic field inside the cavity has been done. The π_1 transition which is very sensitive due to its linear dependence on the magnetic field strength shows that over 0.4%, the double peak structure is totally washed out. For the σ_1 transition on the other hand is not very influenced by increasing inhomogeneity - even up to 10%.

The number of particles per scan point has been varied in order to study the effect of statistics on the resonance scans. This has been done for different magnetic field strength in order to allow an extrapolation to zero magnetic field for every particle number. Down to 900 particles per point the resonance structure is visible. Beneath that, the fitting algorithm still seems to find the two gaussian peaks down to 600 particles per point but they are not really visible to the naked eye. According to this simulations, the reachable precision ($N_0 = 600$) is 5×10^{-7} . For comparison the precision for $N_0 = 1200$ is 2.5×10^{-7} and for $N_0 = 10^5$ simulations show 5×10^{-8} .

The two possible ways of determination of the zero field transition frequency have been compared. Using high statistics, the method using only the σ_1

transition has a higher error of a factor of about 1.12. Although, when using lower statistics due to the sensitivity on inhomogeneities of the π_1 transition, the method using only the σ_1 transition becomes more favorable.

One of the next steps would be to implement a setup for Ramsey spectroscopy [46], using a second cavity which would provides a much better resolution.

Also, the effect of Majorana spin flips [47] which are spin flips caused by strong variations of the magnetic field, should be investigated. This could happen for example inside the CUSP which has zero magnetic field at its center. An implementation of Majorana spin flips in the `hbar_hfs` program is currently ongoing.

Since antihydrogen atoms produced in the CUSP will not be in the ground-state [25] but will decay into lower states while traveling through the setup, scans with higher states taken into account should be done.

Finally, scans using the real detector and event analysis instead of the dummy detector would be of interest.

6 Appendix

6.1 Fit Results: Dependence on Temperature

| T (K) | v_m (m/s) | t (s) |
|-------|-------------|----------------------|
| 20 | 797 | $1.83 \cdot 10^{-4}$ |
| 30 | 974 | $1.49 \cdot 10^{-4}$ |
| 40 | 1 099 | $1.29 \cdot 10^{-4}$ |
| 50 | 1 166 | $1.16 \cdot 10^{-4}$ |
| 60 | 1 198 | $1.06 \cdot 10^{-4}$ |
| 70 | 1 225 | $9.78 \cdot 10^{-5}$ |
| 80 | 1 258 | $9.15 \cdot 10^{-5}$ |
| 90 | 1 288 | $8.62 \cdot 10^{-5}$ |

Table 6.1: Mean velocity v_m (obtained from histograms from simulations using a beam with Maxwell Boltzmann distributed velocity) and time spent in the cavity t for different temperatures. $N_0 = 10^5$.

6 Appendix

| T (K) | $f_{c,me}$ (kHz) | f_{me} (kHz) | $f_{me,e}$ (kHz) | s_{me} (kHz) | $s_{me,e}$ (kHz) |
|-------|------------------|----------------|----------------------|----------------|----------------------|
| 20 | 4.37 | 6.22 | $6.34 \cdot 10^{-2}$ | 5.02 | $2.86 \cdot 10^{-2}$ |
| 30 | 5.35 | 5.67 | $7.18 \cdot 10^{-2}$ | 6.11 | $3.13 \cdot 10^{-2}$ |
| 40 | 6.18 | 6.41 | $7.46 \cdot 10^{-2}$ | 6.99 | $3.24 \cdot 10^{-2}$ |
| 50 | 6.91 | 6.7 | $7.42 \cdot 10^{-2}$ | 7.33 | $3.22 \cdot 10^{-2}$ |
| 60 | 7.56 | 6.86 | $7.52 \cdot 10^{-2}$ | 7.52 | $3.2 \cdot 10^{-2}$ |
| 70 | 8.17 | 6.82 | $6.99 \cdot 10^{-2}$ | 7.6 | $3.22 \cdot 10^{-2}$ |
| 80 | 8.74 | 6.9 | $7.1 \cdot 10^{-2}$ | 7.8 | $3.1 \cdot 10^{-2}$ |
| 90 | 9.27 | 7.05 | $7.75 \cdot 10^{-2}$ | 7.94 | $3.4 \cdot 10^{-2}$ |

Table 6.2: Calculated ($f_{c,me}$) and simulated ($f_{me} \pm f_{me,e}$) FWHM of the monoenergetic beam and as well as peak separation obtained from simulations for different temperatures. $N_0 = 10^5$.

| T (K) | $f_{c,b}$ (kHz) | f_b (kHz) | $f_{b,e}$ (kHz) | s_b (kHz) | $s_{b,e}$ (kHz) |
|-------|-----------------|-------------|-----------------|-------------|----------------------|
| 20 | 5.54 | 4.52 | 0.11 | 4.82 | $4.74 \cdot 10^{-2}$ |
| 30 | 7.18 | 5.75 | 0.13 | 5.95 | $5.56 \cdot 10^{-2}$ |
| 40 | 8.3 | 6.68 | 0.14 | 6.77 | $5.96 \cdot 10^{-2}$ |
| 50 | 9.28 | 6.75 | 0.13 | 6.98 | $5.63 \cdot 10^{-2}$ |
| 60 | 10.16 | 6.75 | 0.13 | 7.1 | $5.74 \cdot 10^{-2}$ |
| 70 | 10.98 | 7.2 | 0.15 | 7.32 | $5.93 \cdot 10^{-2}$ |
| 80 | 11.73 | 7.36 | 0.16 | 7.49 | $6.71 \cdot 10^{-2}$ |
| 90 | 12.45 | 7.51 | 0.19 | 7.72 | $7.76 \cdot 10^{-2}$ |

Table 6.3: Calculated ($f_{c,b}$) and simulated ($f_b \pm f_{b,e}$) FWHM of the beam with Maxwell-Boltzmann distributed velocity, as well as peak separation obtained from simulations for different temperatures. $N_0 = 10^5$.

6 Appendix

| T(K) | v_m (m/s) | b | b_{err} | A | A_{err} |
|------|-----------------------|------------------------|-----------------------|-----------------------|----------------------|
| 20 | 797 | 0.2924 | $2.77 \cdot 10^{-4}$ | $7.483 \cdot 10^{-2}$ | $8.99 \cdot 10^{-4}$ |
| 30 | 974 | 0.2919 | $2.86 \cdot 10^{-4}$ | $7.461 \cdot 10^{-2}$ | $8.24 \cdot 10^{-4}$ |
| 40 | 1 099 | 0.2918 | $2.93 \cdot 10^{-4}$ | $7.637 \cdot 10^{-2}$ | $7.83 \cdot 10^{-4}$ |
| 50 | 1 166 | 0.291 | $2.96 \cdot 10^{-4}$ | $7.837 \cdot 10^{-2}$ | $7.64 \cdot 10^{-4}$ |
| 60 | 1 198 | 0.29 | $2.98 \cdot 10^{-4}$ | $7.959 \cdot 10^{-2}$ | $7.55 \cdot 10^{-4}$ |
| 70 | 1 225 | 0.2898 | $2.97 \cdot 10^{-4}$ | $8.211 \cdot 10^{-2}$ | $7.40 \cdot 10^{-4}$ |
| 80 | 1 258 | 0.2854 | $2.95 \cdot 10^{-4}$ | $8.154 \cdot 10^{-2}$ | $7.41 \cdot 10^{-4}$ |
| 90 | 1 288 | 0.2542 | $2.8 \cdot 10^{-4}$ | $7.091 \cdot 10^{-2}$ | $6.95 \cdot 10^{-4}$ |
| T(K) | ν_σ (MHz) | $\nu_{\sigma,e}$ (MHz) | s(MHz) | s_{err} (MHz) | |
| 20 | 1 420.408005 | $2.978 \cdot 10^{-5}$ | $5.017 \cdot 10^{-3}$ | $2.862 \cdot 10^{-5}$ | |
| 30 | 1 420.408033 | $3.176 \cdot 10^{-5}$ | $6.112 \cdot 10^{-3}$ | $3.134 \cdot 10^{-5}$ | |
| 40 | 1 420.408028 | $3.327 \cdot 10^{-5}$ | $6.985 \cdot 10^{-3}$ | $3.245 \cdot 10^{-5}$ | |
| 50 | 1 420.408015 | $3.295 \cdot 10^{-5}$ | $7.333 \cdot 10^{-3}$ | $3.223 \cdot 10^{-5}$ | |
| 60 | 1 420.407969 | $3.277 \cdot 10^{-5}$ | $7.521 \cdot 10^{-3}$ | $3.201 \cdot 10^{-5}$ | |
| 70 | 1 420.407967 | $3.131 \cdot 10^{-5}$ | $7.600 \cdot 10^{-3}$ | $3.217 \cdot 10^{-5}$ | |
| 80 | 1 420.407992 | $3.153 \cdot 10^{-5}$ | $7.796 \cdot 10^{-3}$ | $3.098 \cdot 10^{-5}$ | |
| 90 | 1 420.408028 | $3.463 \cdot 10^{-5}$ | $7.937 \cdot 10^{-3}$ | $3.404 \cdot 10^{-5}$ | |
| T(K) | f(MHz) | f_{err} (MHz) | χ^2 | χ^2/N_f | |
| 20 | $4.772 \cdot 10^{-3}$ | $6.341 \cdot 10^{-5}$ | 221.38 | 2.218 | |
| 30 | $5.671 \cdot 10^{-3}$ | $7.177 \cdot 10^{-5}$ | 169.03 | 1.938 | |
| 40 | $6.411 \cdot 10^{-3}$ | $7.455 \cdot 10^{-5}$ | 238.41 | 2.302 | |
| 50 | $6.701 \cdot 10^{-3}$ | $7.419 \cdot 10^{-5}$ | 315.57 | 2.648 | |
| 60 | $6.856 \cdot 10^{-3}$ | $7.521 \cdot 10^{-5}$ | 370.62 | 2.87 | |
| 70 | $6.817 \cdot 10^{-3}$ | $6.989 \cdot 10^{-5}$ | 434.21 | 3.106 | |
| 80 | $6.902 \cdot 10^{-3}$ | $7.097 \cdot 10^{-5}$ | 483.25 | 3.277 | |
| 90 | $7.047 \cdot 10^{-3}$ | $7.745 \cdot 10^{-5}$ | 462.09 | 3.204 | |

Table 6.4: Fit parameters with errors as well as χ^2 value for simulated scans using a monovelocity beam with different v_m . $N_0 = 10^5$.

6 Appendix

| T(K) | power(W) | b | b_{err} | A | A_{err} |
|------|----------------------|--------|----------------------|-----------------------|----------------------|
| 20 | $1.5 \cdot 10^{-2}$ | 0.1291 | $1.92 \cdot 10^{-4}$ | $2.993 \cdot 10^{-2}$ | $6.01 \cdot 10^{-4}$ |
| 30 | $2.24 \cdot 10^{-2}$ | 0.1291 | $1.94 \cdot 10^{-4}$ | $2.931 \cdot 10^{-2}$ | $5.48 \cdot 10^{-4}$ |
| 40 | $2.99 \cdot 10^{-2}$ | 0.133 | $2.03 \cdot 10^{-4}$ | $3.032 \cdot 10^{-2}$ | $5.34 \cdot 10^{-4}$ |
| 50 | $3.74 \cdot 10^{-2}$ | 0.1392 | $2.06 \cdot 10^{-4}$ | $3.217 \cdot 10^{-2}$ | $5.42 \cdot 10^{-4}$ |
| 60 | $4.49 \cdot 10^{-2}$ | 0.1417 | $2.09 \cdot 10^{-4}$ | $3.246 \cdot 10^{-2}$ | $5.47 \cdot 10^{-4}$ |
| 70 | $5.24 \cdot 10^{-2}$ | 0.1404 | $2.13 \cdot 10^{-4}$ | $3.228 \cdot 10^{-2}$ | $5.32 \cdot 10^{-4}$ |
| 80 | $5.98 \cdot 10^{-2}$ | 0.1368 | $2.12 \cdot 10^{-4}$ | $2.965 \cdot 10^{-2}$ | $5.21 \cdot 10^{-4}$ |
| 90 | $6.73 \cdot 10^{-2}$ | 0.132 | $2.11 \cdot 10^{-4}$ | $2.637 \cdot 10^{-2}$ | $5.18 \cdot 10^{-4}$ |

| T(K) | $\nu_{\sigma}(MHz)$ | $\nu_{\sigma,e}(MHz)$ | s(MHz) | $s_{err}(MHz)$ |
|------|---------------------|-----------------------|-----------------------|-----------------------|
| 20 | 1 420.408072 | $4.815 \cdot 10^{-5}$ | $4.822 \cdot 10^{-3}$ | $4.738 \cdot 10^{-5}$ |
| 30 | 1 420.408063 | $5.541 \cdot 10^{-5}$ | $5.951 \cdot 10^{-3}$ | $5.557 \cdot 10^{-5}$ |
| 40 | 1 420.407977 | $5.881 \cdot 10^{-5}$ | $6.771 \cdot 10^{-3}$ | $5.957 \cdot 10^{-5}$ |
| 50 | 1 420.407965 | $5.714 \cdot 10^{-5}$ | $6.978 \cdot 10^{-3}$ | $5.631 \cdot 10^{-5}$ |
| 60 | 1 420.408016 | $5.552 \cdot 10^{-5}$ | $7.095 \cdot 10^{-3}$ | $5.740 \cdot 10^{-5}$ |
| 70 | 1 420.408054 | $5.941 \cdot 10^{-5}$ | $7.317 \cdot 10^{-3}$ | $5.934 \cdot 10^{-5}$ |
| 80 | 1 420.407928 | $6.366 \cdot 10^{-5}$ | $7.487 \cdot 10^{-3}$ | $6.706 \cdot 10^{-5}$ |
| 90 | 1 420.408053 | $7.264 \cdot 10^{-5}$ | $7.720 \cdot 10^{-3}$ | $7.761 \cdot 10^{-5}$ |

| T(K) | f(MHz) | $f_{err}(MHz)$ | χ^2 | χ^2/N_f |
|------|-----------------------|-----------------------|----------|--------------|
| 20 | $4.520 \cdot 10^{-3}$ | $1.073 \cdot 10^{-4}$ | 81.81 | 1.348 |
| 30 | $5.746 \cdot 10^{-3}$ | $1.292 \cdot 10^{-4}$ | 137 | 1.745 |
| 40 | $6.684 \cdot 10^{-3}$ | $1.361 \cdot 10^{-4}$ | 139.45 | 1.76 |
| 50 | $6.748 \cdot 10^{-3}$ | $1.335 \cdot 10^{-4}$ | 150.59 | 1.829 |
| 60 | $6.753 \cdot 10^{-3}$ | $1.347 \cdot 10^{-4}$ | 136.89 | 1.744 |
| 70 | $7.204 \cdot 10^{-3}$ | $1.459 \cdot 10^{-4}$ | 151.91 | 1.837 |
| 80 | $7.364 \cdot 10^{-3}$ | $1.600 \cdot 10^{-4}$ | 280.26 | 2.496 |
| 90 | $7.506 \cdot 10^{-3}$ | $1.893 \cdot 10^{-4}$ | 278.11 | 2.486 |

Table 6.5: Fit parameters with errors, χ^2 value and calculated optimum power for simulated scans using a beam with Maxwell-Boltzmann distributed velocity with different temperatures. $N_0 = 10^5$.

6.2 Fit Results: Dependence on Cavity Power

| T(K) | b | b_{err} | A | A_{err} | ν_{σ} (MHz) | $\nu_{\sigma,e}$ (MHz) |
|------|--------|----------------------|-----------------------|----------------------|----------------------|------------------------|
| 20 | 0.1276 | $1.85 \cdot 10^{-4}$ | $2.374 \cdot 10^{-2}$ | $6.26 \cdot 10^{-4}$ | 1420.407903 | $6.598 \cdot 10^{-5}$ |
| 30 | 0.1285 | $1.92 \cdot 10^{-4}$ | $3.008 \cdot 10^{-2}$ | $5.53 \cdot 10^{-4}$ | 1420.407947 | $5.482 \cdot 10^{-5}$ |
| 40 | 0.1325 | $1.99 \cdot 10^{-4}$ | $3.124 \cdot 10^{-2}$ | $5.34 \cdot 10^{-4}$ | 1420.408041 | $5.533 \cdot 10^{-5}$ |
| 50 | 0.1392 | $2.06 \cdot 10^{-4}$ | $3.217 \cdot 10^{-2}$ | $5.42 \cdot 10^{-4}$ | 1420.407965 | $5.714 \cdot 10^{-5}$ |
| 60 | 0.1418 | $2.11 \cdot 10^{-4}$ | $3.129 \cdot 10^{-2}$ | $5.41 \cdot 10^{-4}$ | 1420.407983 | $6.051 \cdot 10^{-5}$ |
| 70 | 0.1408 | $2.23 \cdot 10^{-4}$ | $3.088 \cdot 10^{-2}$ | $5.49 \cdot 10^{-4}$ | 1420.408001 | $6.296 \cdot 10^{-5}$ |
| 80 | 0.1377 | $2.09 \cdot 10^{-4}$ | $2.983 \cdot 10^{-2}$ | $5.26 \cdot 10^{-4}$ | 1420.407997 | $6.392 \cdot 10^{-5}$ |
| 90 | 0.1329 | $2.08 \cdot 10^{-4}$ | $2.775 \cdot 10^{-2}$ | $5.11 \cdot 10^{-4}$ | 1420.407988 | $6.753 \cdot 10^{-5}$ |

| T(K) | s(MHz) | s_{err} (MHz) | f(MHz) | f_{err} (MHz) | χ^2 | χ^2/N_f |
|------|-----------------------|-----------------------|-----------------------|-----------------------|----------|--------------|
| 20 | $4.917 \cdot 10^{-3}$ | $6.767 \cdot 10^{-5}$ | $4.887 \cdot 10^{-3}$ | $1.557 \cdot 10^{-4}$ | 186.21 | 2.034 |
| 30 | $6.002 \cdot 10^{-3}$ | $5.452 \cdot 10^{-5}$ | $5.879 \cdot 10^{-3}$ | $1.280 \cdot 10^{-4}$ | 154.77 | 1.855 |
| 40 | $6.632 \cdot 10^{-3}$ | $5.537 \cdot 10^{-5}$ | $6.474 \cdot 10^{-3}$ | $1.313 \cdot 10^{-4}$ | 117.75 | 1.618 |
| 50 | $6.978 \cdot 10^{-3}$ | $5.631 \cdot 10^{-5}$ | $6.748 \cdot 10^{-3}$ | $1.335 \cdot 10^{-4}$ | 150.59 | 1.829 |
| 60 | $7.141 \cdot 10^{-3}$ | $6.106 \cdot 10^{-5}$ | $7.012 \cdot 10^{-3}$ | $1.431 \cdot 10^{-4}$ | 191.18 | 2.061 |
| 70 | $7.217 \cdot 10^{-3}$ | $6.264 \cdot 10^{-5}$ | $7.112 \cdot 10^{-3}$ | $1.479 \cdot 10^{-4}$ | 133.39 | 1.722 |
| 80 | $7.351 \cdot 10^{-3}$ | $6.375 \cdot 10^{-5}$ | $7.264 \cdot 10^{-3}$ | $1.499 \cdot 10^{-4}$ | 151.98 | 1.838 |
| 90 | $7.562 \cdot 10^{-3}$ | $6.832 \cdot 10^{-5}$ | $7.431 \cdot 10^{-3}$ | $1.625 \cdot 10^{-4}$ | 118.69 | 1.624 |

Table 6.6: Fit parameters with errors, χ^2 value as well as calculated power for simulated scans using a beam with Maxwell-Boltzmann distributed velocity for different temperatures T, the optimum power for 50 K and $N_0 = 10^5$.

6.3 Fit Results: Dependence on Inhomogeneity

| σ (%) | b | b_{err} | A | A_{err} | $\nu_{\pi}(MHz)$ | $\nu_{\pi,e}(MHz)$ |
|--------------|--------|----------------------|-----------------------|----------------------|------------------|-----------------------|
| 0 | 0.2871 | $2.94 \cdot 10^{-4}$ | $7.266 \cdot 10^{-2}$ | $7.60 \cdot 10^{-4}$ | 1421.666098 | $3.116 \cdot 10^{-5}$ |
| 0.1 | 0.2862 | $2.99 \cdot 10^{-4}$ | $6.609 \cdot 10^{-2}$ | $7.52 \cdot 10^{-4}$ | 1421.666083 | $3.547 \cdot 10^{-5}$ |
| 0.2 | 0.2861 | $3.17 \cdot 10^{-4}$ | $5.116 \cdot 10^{-2}$ | $7.18 \cdot 10^{-4}$ | 1421.666192 | $5.394 \cdot 10^{-5}$ |
| 0.3 | 0.2865 | $3.5 \cdot 10^{-4}$ | $3.917 \cdot 10^{-2}$ | $6.90 \cdot 10^{-4}$ | 1421.666119 | $9.475 \cdot 10^{-5}$ |
| 0.4 | 0.2878 | $4.24 \cdot 10^{-4}$ | $3.089 \cdot 10^{-2}$ | $7.32 \cdot 10^{-4}$ | 1421.666264 | $1.598 \cdot 10^{-4}$ |
| 0.5 | 0.2896 | $7.07 \cdot 10^{-4}$ | $2.448 \cdot 10^{-2}$ | $1.10 \cdot 10^{-3}$ | 1421.666053 | $1.993 \cdot 10^{-4}$ |

| σ (%) | s(MHz) | s_{err} (MHz) | f(MHz) | f_{err} (MHz) | χ^2 | χ^2/N_f |
|--------------|-----------------------|-----------------------|-----------------------|-----------------------|----------|--------------|
| 0 | $6.954 \cdot 10^{-3}$ | $3.060 \cdot 10^{-5}$ | $5.925 \cdot 10^{-3}$ | $6.843 \cdot 10^{-5}$ | 736.72 | 4.046 |
| 0.1 | $6.966 \cdot 10^{-3}$ | $3.466 \cdot 10^{-5}$ | $6.254 \cdot 10^{-3}$ | $7.980 \cdot 10^{-5}$ | 486.08 | 3.287 |
| 0.2 | $6.954 \cdot 10^{-3}$ | $4.977 \cdot 10^{-5}$ | $7.730 \cdot 10^{-3}$ | $1.200 \cdot 10^{-4}$ | 166.01 | 1.921 |
| 0.3 | $7.078 \cdot 10^{-3}$ | $7.752 \cdot 10^{-5}$ | $1.043 \cdot 10^{-2}$ | $2.139 \cdot 10^{-4}$ | 117.53 | 1.616 |
| 0.4 | $7.329 \cdot 10^{-3}$ | $1.167 \cdot 10^{-4}$ | $1.458 \cdot 10^{-2}$ | $4.612 \cdot 10^{-4}$ | 55.45 | 1.11 |
| 0.5 | $7.298 \cdot 10^{-3}$ | $2.623 \cdot 10^{-4}$ | $2.073 \cdot 10^{-2}$ | $1.526 \cdot 10^{-3}$ | 61.38 | 1.168 |

Table 6.7: Fit parameters with errors as well as χ^2 for different inhomogeneities σ for simulated scans using $N_0 = 10^5$ and a monovelocity beam with v_m , the mean velocity of a MB distributed beam of 50 K.

6 Appendix

| σ (%) | b | b_{err} | A | A_{err} | $\nu_{\pi}(MHz)$ | $\nu_{\pi,e}(MHz)$ |
|--------------|--------|----------------------|-----------------------|----------------------|------------------|-----------------------|
| 0.1 | 0.1368 | $2.31 \cdot 10^{-4}$ | $2.190 \cdot 10^{-2}$ | $5.30 \cdot 10^{-4}$ | 1421.665976 | $8.217 \cdot 10^{-5}$ |
| 0.2 | 0.1374 | $2.45 \cdot 10^{-4}$ | $1.909 \cdot 10^{-2}$ | $4.71 \cdot 10^{-4}$ | 1421.66606 | $1.179 \cdot 10^{-4}$ |
| 0.3 | 0.1379 | $2.74 \cdot 10^{-4}$ | $1.549 \cdot 10^{-2}$ | $4.58 \cdot 10^{-4}$ | 1421.66583 | $1.892 \cdot 10^{-4}$ |
| 0.4 | 0.1383 | $3.26 \cdot 10^{-4}$ | $1.307 \cdot 10^{-2}$ | $4.68 \cdot 10^{-4}$ | 1421.665769 | $2.738 \cdot 10^{-4}$ |
| 0.5 | 0.1388 | $4.49 \cdot 10^{-4}$ | $1.095 \cdot 10^{-2}$ | $5.32 \cdot 10^{-4}$ | 1421.666695 | $3.523 \cdot 10^{-4}$ |

| σ (%) | s(MHz) | s_{err} (MHz) | f(MHz) | f_{err} (MHz) | χ^2 | χ^2/N_f |
|--------------|-----------------------|-----------------------|-----------------------|-----------------------|----------|--------------|
| 0.1 | $7.283 \cdot 10^{-3}$ | $8.751 \cdot 10^{-5}$ | $7.228 \cdot 10^{-3}$ | $2.158 \cdot 10^{-4}$ | 179.1 | 1.995 |
| 0.2 | $7.609 \cdot 10^{-3}$ | $1.148 \cdot 10^{-4}$ | $9.558 \cdot 10^{-3}$ | $2.846 \cdot 10^{-4}$ | 123.45 | 1.656 |
| 0.3 | $8.194 \cdot 10^{-3}$ | $1.537 \cdot 10^{-4}$ | $1.260 \cdot 10^{-2}$ | $4.422 \cdot 10^{-4}$ | 54.27 | 1.098 |
| 0.4 | $8.419 \cdot 10^{-3}$ | $2.076 \cdot 10^{-4}$ | $1.583 \cdot 10^{-2}$ | $7.461 \cdot 10^{-4}$ | 42.84 | 0.976 |
| 0.5 | $8.495 \cdot 10^{-3}$ | $3.046 \cdot 10^{-4}$ | $2.020 \cdot 10^{-2}$ | $1.535 \cdot 10^{-3}$ | 32.04 | 0.844 |

Table 6.8: Fit parameters with errors as well as χ^2 for different inhomogeneities σ for simulated scans using $N_0 = 10^5$ and a MB beam with 50 K.

| σ (%) | b | b_{err} | A | A_{err} | $\nu_{\sigma}(MHz)$ | $\nu_{\sigma,e}(MHz)$ |
|--------------|--------|----------------------|-----------------------|----------------------|---------------------|-----------------------|
| 0.1 | 0.1873 | $2.63 \cdot 10^{-4}$ | $4.394 \cdot 10^{-2}$ | $5.46 \cdot 10^{-4}$ | 1420.408011 | $4.814 \cdot 10^{-5}$ |
| 0.5 | 0.1874 | $2.63 \cdot 10^{-4}$ | $4.398 \cdot 10^{-2}$ | $5.54 \cdot 10^{-4}$ | 1420.407975 | $4.839 \cdot 10^{-5}$ |
| 1 | 0.1869 | $2.63 \cdot 10^{-4}$ | $4.314 \cdot 10^{-2}$ | $5.53 \cdot 10^{-4}$ | 1420.408075 | $4.948 \cdot 10^{-5}$ |
| 5 | 0.1872 | $2.64 \cdot 10^{-4}$ | $4.240 \cdot 10^{-2}$ | $5.50 \cdot 10^{-4}$ | 1420.407949 | $5.043 \cdot 10^{-5}$ |
| 10 | 0.1873 | $2.65 \cdot 10^{-4}$ | $4.314 \cdot 10^{-2}$ | $5.53 \cdot 10^{-4}$ | 1420.407996 | $2.788 \cdot 10^{-5}$ |

| σ (%) | s(MHz) | s_{err} (MHz) | f(MHz) | f_{err} (MHz) | χ^2 | χ^2/N_f |
|--------------|-----------------------|-----------------------|-----------------------|-----------------------|----------|--------------|
| 0.1 | $8.852 \cdot 10^{-3}$ | $4.762 \cdot 10^{-5}$ | $7.911 \cdot 10^{-3}$ | $1.145 \cdot 10^{-4}$ | 191.62 | 2.064 |
| 0.5 | $8.907 \cdot 10^{-3}$ | $4.755 \cdot 10^{-5}$ | $7.946 \cdot 10^{-3}$ | $1.132 \cdot 10^{-4}$ | 173.09 | 1.961 |
| 1 | $8.804 \cdot 10^{-3}$ | $4.871 \cdot 10^{-5}$ | $7.985 \cdot 10^{-3}$ | $1.171 \cdot 10^{-4}$ | 157.66 | 1.872 |
| 5 | $8.782 \cdot 10^{-3}$ | $5.003 \cdot 10^{-5}$ | $8.092 \cdot 10^{-3}$ | $1.181 \cdot 10^{-4}$ | 181.57 | 2.009 |
| 10 | $8.847 \cdot 10^{-3}$ | $5.291 \cdot 10^{-5}$ | $8.070 \cdot 10^{-3}$ | $1.179 \cdot 10^{-4}$ | 132.23 | 1.714 |

Table 6.9: Fit parameters b, A and ν_{σ} with errors for different inhomogeneities σ for simulated scans using $N_0 = 10^5$ and a beam monovelocity beam with v_m , the mean velocity of a MB distributed beam of 50 K.

6.4 Fit Results: Dependence on Statistics

| N_0 | b | b_{err} | A | A_{err} | ν_σ (MHz) | $\nu_{\sigma,e}$ (MHz) |
|-------|--------|----------------------|-----------------------|----------------------|--------------------|------------------------|
| 600 | 0.1408 | $3.06 \cdot 10^{-3}$ | $2.991 \cdot 10^{-2}$ | $6.09 \cdot 10^{-3}$ | 1420.40699 | $1.181 \cdot 10^{-3}$ |
| 700 | 0.1437 | $3.12 \cdot 10^{-3}$ | $4.027 \cdot 10^{-2}$ | $5.34 \cdot 10^{-3}$ | 1420.40726 | $6.345 \cdot 10^{-4}$ |
| 800 | 0.1377 | $2.23 \cdot 10^{-3}$ | $3.521 \cdot 10^{-2}$ | $5.92 \cdot 10^{-3}$ | 1420.408002 | $5.059 \cdot 10^{-4}$ |
| 900 | 0.1358 | $2.4 \cdot 10^{-3}$ | $3.997 \cdot 10^{-2}$ | $6.95 \cdot 10^{-3}$ | 1420.408147 | $5.287 \cdot 10^{-4}$ |
| 1000 | 0.1373 | $2.07 \cdot 10^{-3}$ | $3.467 \cdot 10^{-2}$ | $5.58 \cdot 10^{-3}$ | 1420.408549 | $4.263 \cdot 10^{-4}$ |
| 1100 | 0.1383 | $2.06 \cdot 10^{-3}$ | $2.993 \cdot 10^{-2}$ | $5.01 \cdot 10^{-3}$ | 1420.408271 | $3.749 \cdot 10^{-4}$ |
| 1300 | 0.1376 | $1.9 \cdot 10^{-3}$ | $3.250 \cdot 10^{-2}$ | $4.84 \cdot 10^{-3}$ | 1420.408306 | $4.826 \cdot 10^{-4}$ |
| 1500 | 0.1411 | $1.68 \cdot 10^{-3}$ | $3.893 \cdot 10^{-2}$ | $4.36 \cdot 10^{-3}$ | 1420.408066 | $3.244 \cdot 10^{-4}$ |
| 1700 | 0.1374 | $1.58 \cdot 10^{-3}$ | $3.584 \cdot 10^{-2}$ | $4.09 \cdot 10^{-3}$ | 1420.408009 | $3.386 \cdot 10^{-4}$ |
| 2000 | 0.1363 | $1.52 \cdot 10^{-3}$ | $3.130 \cdot 10^{-2}$ | $3.75 \cdot 10^{-3}$ | 1420.408268 | $3.776 \cdot 10^{-4}$ |

| N_0 | s(MHz) | s_{err} (MHz) | f(MHz) | f_{err} (MHz) | χ^2 | χ^2/N_f |
|-------|-----------------------|-----------------------|-----------------------|-----------------------|----------|--------------|
| 600 | $6.989 \cdot 10^{-3}$ | $8.353 \cdot 10^{-4}$ | $9.829 \cdot 10^{-3}$ | $2.256 \cdot 10^{-3}$ | 36.21 | 0.897 |
| 700 | $9.080 \cdot 10^{-3}$ | $6.845 \cdot 10^{-4}$ | $1.003 \cdot 10^{-2}$ | $1.606 \cdot 10^{-3}$ | 45.91 | 1.01 |
| 800 | $6.985 \cdot 10^{-3}$ | $4.935 \cdot 10^{-4}$ | $5.461 \cdot 10^{-3}$ | $1.044 \cdot 10^{-3}$ | 43.04 | 0.978 |
| 900 | $7.118 \cdot 10^{-3}$ | $5.175 \cdot 10^{-4}$ | $5.060 \cdot 10^{-3}$ | $1.761 \cdot 10^{-3}$ | 32.93 | 0.855 |
| 1000 | $6.581 \cdot 10^{-3}$ | $4.325 \cdot 10^{-4}$ | $5.209 \cdot 10^{-3}$ | $1.213 \cdot 10^{-3}$ | 32.55 | 0.85 |
| 1100 | $7.435 \cdot 10^{-3}$ | $5.170 \cdot 10^{-4}$ | $6.329 \cdot 10^{-3}$ | $1.417 \cdot 10^{-3}$ | 36.24 | 0.897 |
| 1300 | $7.176 \cdot 10^{-3}$ | $4.959 \cdot 10^{-4}$ | $6.063 \cdot 10^{-3}$ | $1.344 \cdot 10^{-3}$ | 51.48 | 1.07 |
| 1500 | $6.375 \cdot 10^{-3}$ | $3.395 \cdot 10^{-4}$ | $5.719 \cdot 10^{-3}$ | $7.187 \cdot 10^{-4}$ | 35.49 | 0.888 |
| 1700 | $6.686 \cdot 10^{-3}$ | $3.293 \cdot 10^{-4}$ | $5.924 \cdot 10^{-3}$ | $8.314 \cdot 10^{-4}$ | 35.55 | 0.889 |
| 2000 | $7.854 \cdot 10^{-3}$ | $4.022 \cdot 10^{-4}$ | $6.306 \cdot 10^{-3}$ | $1.043 \cdot 10^{-3}$ | 59.61 | 1.151 |

Table 6.10: Fit parameters and their errors for scans using different number of particles per scan point N_0 . A fieldmap with $\mu = 0.88$ G and $rms = 0.0053$ G was used.

6 Appendix

| N_0 | b | b_{err} | A | A_{err} | $\nu_\sigma(MHz)$ | $\nu_{\sigma,e}(MHz)$ |
|-------|--------|----------------------|-----------------------|----------------------|-------------------|-----------------------|
| 600 | 0.1414 | $2.93 \cdot 10^{-3}$ | $3.539 \cdot 10^{-2}$ | $7.02 \cdot 10^{-3}$ | 1420.418722 | $6.828 \cdot 10^{-4}$ |
| 700 | 0.1347 | $2.76 \cdot 10^{-3}$ | $3.022 \cdot 10^{-2}$ | $6.51 \cdot 10^{-3}$ | 1420.418632 | $6.057 \cdot 10^{-4}$ |
| 800 | 0.1364 | $2.35 \cdot 10^{-3}$ | $3.218 \cdot 10^{-2}$ | $5.71 \cdot 10^{-3}$ | 1420.419168 | $5.218 \cdot 10^{-4}$ |
| 900 | 0.1365 | $2.23 \cdot 10^{-3}$ | $3.459 \cdot 10^{-2}$ | $5.51 \cdot 10^{-3}$ | 1420.419181 | $4.417 \cdot 10^{-4}$ |
| 1000 | 0.1395 | $2.61 \cdot 10^{-3}$ | $3.097 \cdot 10^{-2}$ | $4.48 \cdot 10^{-3}$ | 1420.41862 | $4.300 \cdot 10^{-4}$ |
| 1100 | 0.1349 | $2.15 \cdot 10^{-3}$ | $3.120 \cdot 10^{-2}$ | $4.78 \cdot 10^{-3}$ | 1420.419498 | $4.664 \cdot 10^{-4}$ |
| 1300 | 0.1355 | $1.77 \cdot 10^{-3}$ | $3.654 \cdot 10^{-2}$ | $4.70 \cdot 10^{-3}$ | 1420.418533 | $3.086 \cdot 10^{-4}$ |
| 1500 | 0.1401 | $1.86 \cdot 10^{-3}$ | $3.537 \cdot 10^{-2}$ | $3.97 \cdot 10^{-3}$ | 1420.418592 | $2.774 \cdot 10^{-4}$ |
| 1700 | 0.1362 | $1.61 \cdot 10^{-3}$ | $3.078 \cdot 10^{-2}$ | $3.81 \cdot 10^{-3}$ | 1420.418538 | $3.580 \cdot 10^{-4}$ |
| 2000 | 0.1382 | $1.55 \cdot 10^{-3}$ | $3.585 \cdot 10^{-2}$ | $3.41 \cdot 10^{-3}$ | 1420.419029 | $3.012 \cdot 10^{-4}$ |

| N_0 | s(MHz) | s_{err} (MHz) | f(MHz) | f_{err} (MHz) | χ^2 | χ^2/N_f |
|-------|-----------------------|-----------------------|-----------------------|-----------------------|----------|--------------|
| 600 | $7.180 \cdot 10^{-3}$ | $7.040 \cdot 10^{-4}$ | $5.692 \cdot 10^{-3}$ | $1.688 \cdot 10^{-3}$ | 36.91 | 0.906 |
| 700 | $6.916 \cdot 10^{-3}$ | $5.833 \cdot 10^{-4}$ | $5.572 \cdot 10^{-3}$ | $2.038 \cdot 10^{-3}$ | 32.52 | 0.85 |
| 800 | $7.634 \cdot 10^{-3}$ | $5.323 \cdot 10^{-4}$ | $5.326 \cdot 10^{-3}$ | $1.147 \cdot 10^{-3}$ | 35.16 | 0.884 |
| 900 | $7.234 \cdot 10^{-3}$ | $4.174 \cdot 10^{-4}$ | $5.435 \cdot 10^{-3}$ | $1.110 \cdot 10^{-3}$ | 23.99 | 0.73 |
| 1000 | $7.129 \cdot 10^{-3}$ | $6.736 \cdot 10^{-4}$ | $8.929 \cdot 10^{-3}$ | $1.612 \cdot 10^{-3}$ | 41.3 | 0.958 |
| 1100 | $6.266 \cdot 10^{-3}$ | $5.181 \cdot 10^{-4}$ | $6.184 \cdot 10^{-3}$ | $1.342 \cdot 10^{-3}$ | 40.95 | 0.954 |
| 1300 | $6.501 \cdot 10^{-3}$ | $3.088 \cdot 10^{-4}$ | $4.507 \cdot 10^{-3}$ | $7.795 \cdot 10^{-4}$ | 36.22 | 0.897 |
| 1500 | $5.871 \cdot 10^{-3}$ | $4.213 \cdot 10^{-4}$ | $6.472 \cdot 10^{-3}$ | $9.408 \cdot 10^{-4}$ | 54.84 | 1.104 |
| 1700 | $6.656 \cdot 10^{-3}$ | $3.532 \cdot 10^{-4}$ | $5.660 \cdot 10^{-3}$ | $7.834 \cdot 10^{-4}$ | 47.31 | 1.025 |
| 2000 | $6.835 \cdot 10^{-3}$ | $2.937 \cdot 10^{-4}$ | $5.970 \cdot 10^{-3}$ | $7.092 \cdot 10^{-4}$ | 49.08 | 1.044 |

Table 6.11: Fit parameters and their errors for scans using different number of particles per scan point N_0 . A fieldmap with $\mu = 2.19$ G and $rms = 0.014$ G was used.

6 Appendix

| N_0 | b | b_{err} | A | A_{err} | $\nu_\sigma(MHz)$ | $\nu_{\sigma,e}(MHz)$ |
|-------|-----------------------|-----------------------|-----------------------|-----------------------|-------------------|-----------------------|
| 600 | 0.1413 | $3.1 \cdot 10^{-3}$ | $3.342 \cdot 10^{-2}$ | $5.87 \cdot 10^{-3}$ | 1420.458454 | $6.773 \cdot 10^{-4}$ |
| 700 | 0.1383 | $2.99 \cdot 10^{-3}$ | $2.986 \cdot 10^{-2}$ | $5.75 \cdot 10^{-3}$ | 1420.459027 | $6.553 \cdot 10^{-4}$ |
| 800 | 0.137 | $2.7 \cdot 10^{-3}$ | $3.063 \cdot 10^{-2}$ | $5.14 \cdot 10^{-3}$ | 1420.458672 | $6.319 \cdot 10^{-4}$ |
| 900 | 0.1375 | $2.6 \cdot 10^{-3}$ | $2.959 \cdot 10^{-2}$ | $4.94 \cdot 10^{-3}$ | 1420.458868 | $6.149 \cdot 10^{-4}$ |
| 1000 | 0.1413 | $2.63 \cdot 10^{-3}$ | $3.292 \cdot 10^{-2}$ | $4.43 \cdot 10^{-3}$ | 1420.458872 | $6.027 \cdot 10^{-4}$ |
| 1100 | 0.1361 | $2.12 \cdot 10^{-3}$ | $2.864 \cdot 10^{-2}$ | $4.55 \cdot 10^{-3}$ | 1420.458659 | $5.531 \cdot 10^{-4}$ |
| 1300 | 0.1381 | $1.96 \cdot 10^{-3}$ | $3.174 \cdot 10^{-2}$ | $4.09 \cdot 10^{-3}$ | 1420.458695 | $4.576 \cdot 10^{-4}$ |
| 1500 | 0.139 | $1.97 \cdot 10^{-3}$ | $3.286 \cdot 10^{-2}$ | $3.72 \cdot 10^{-3}$ | 1420.458448 | $4.313 \cdot 10^{-4}$ |
| 1700 | 0.1376 | $1.68 \cdot 10^{-3}$ | $3.252 \cdot 10^{-2}$ | $3.85 \cdot 10^{-3}$ | 1420.458867 | $3.512 \cdot 10^{-4}$ |
| 2000 | 0.14 | $1.61 \cdot 10^{-3}$ | $3.605 \cdot 10^{-2}$ | $3.30 \cdot 10^{-3}$ | 1420.458387 | $3.118 \cdot 10^{-4}$ |
| N_0 | s(MHz) | s_{err} (MHz) | f(MHz) | f_{err} (MHz) | χ^2 | χ^2/N_f |
| 600 | $7.799 \cdot 10^{-3}$ | $6.482 \cdot 10^{-4}$ | $8.061 \cdot 10^{-3}$ | $1.443 \cdot 10^{-3}$ | 45.61 | 1.007 |
| 700 | $7.728 \cdot 10^{-3}$ | $6.614 \cdot 10^{-4}$ | $7.097 \cdot 10^{-3}$ | $2.059 \cdot 10^{-3}$ | 42.25 | 0.969 |
| 800 | $7.963 \cdot 10^{-3}$ | $6.300 \cdot 10^{-4}$ | $7.805 \cdot 10^{-3}$ | $1.555 \cdot 10^{-3}$ | 26.62 | 0.769 |
| 900 | $7.148 \cdot 10^{-3}$ | $5.618 \cdot 10^{-4}$ | $7.121 \cdot 10^{-3}$ | $1.711 \cdot 10^{-3}$ | 33.42 | 0.862 |
| 1000 | $7.953 \cdot 10^{-3}$ | $5.535 \cdot 10^{-4}$ | $9.398 \cdot 10^{-3}$ | $1.397 \cdot 10^{-3}$ | 41.63 | 0.962 |
| 1100 | $6.431 \cdot 10^{-3}$ | $5.495 \cdot 10^{-4}$ | $6.942 \cdot 10^{-3}$ | $1.197 \cdot 10^{-3}$ | 33.85 | 0.867 |
| 1300 | $7.192 \cdot 10^{-3}$ | $4.603 \cdot 10^{-4}$ | $6.896 \cdot 10^{-3}$ | $9.631 \cdot 10^{-4}$ | 30.64 | 0.825 |
| 1500 | $7.291 \cdot 10^{-3}$ | $4.723 \cdot 10^{-4}$ | $7.969 \cdot 10^{-3}$ | $1.002 \cdot 10^{-3}$ | 46.48 | 1.016 |
| 1700 | $6.892 \cdot 10^{-3}$ | $3.407 \cdot 10^{-4}$ | $5.643 \cdot 10^{-3}$ | $9.251 \cdot 10^{-4}$ | 50.23 | 1.057 |
| 2000 | $7.093 \cdot 10^{-3}$ | $3.009 \cdot 10^{-4}$ | $6.826 \cdot 10^{-3}$ | $7.301 \cdot 10^{-4}$ | 44.14 | 0.99 |

Table 6.12: Fit parameters and their errors for scans using different number of particles per scan point N_0 . A fieldmap with $\mu = 4.39$ G and $rms = 0.029$ G was used.

| N_0 | $\nu_0(MHz)$ | $\nu_{0,e}(MHz)$ | $\nu_{e,rel}$ | χ^2/N_f |
|-------|--------------|-----------------------|-----------------------|-------------------|
| 2 000 | 1 420.406105 | $3.194 \cdot 10^{-4}$ | $2.248 \cdot 10^{-7}$ | 0.285 |
| 1 700 | 1 420.405703 | $3.195 \cdot 10^{-4}$ | $2.249 \cdot 10^{-7}$ | 1.052 |
| 1 500 | 1 420.405779 | $2.899 \cdot 10^{-4}$ | $2.041 \cdot 10^{-7}$ | 0.959 |
| 1 300 | 1 420.405137 | $3.604 \cdot 10^{-4}$ | $2.537 \cdot 10^{-7}$ | 0.22 |
| 1 100 | 1 420.40631 | $3.327 \cdot 10^{-4}$ | $2.342 \cdot 10^{-7}$ | 0.734 |
| 1 000 | 1 420.406302 | $3.894 \cdot 10^{-4}$ | $2.741 \cdot 10^{-7}$ | 0.533 |
| 900 | 1 420.406025 | $4.356 \cdot 10^{-4}$ | $3.067 \cdot 10^{-7}$ | $2 \cdot 10^{-3}$ |
| 800 | 1 420.40594 | $4.448 \cdot 10^{-4}$ | $3.131 \cdot 10^{-7}$ | 0.205 |
| 700 | 1 420.405148 | $5.329 \cdot 10^{-4}$ | $3.752 \cdot 10^{-7}$ | 0.142 |
| 600 | 1 420.405142 | $6.504 \cdot 10^{-4}$ | $4.579 \cdot 10^{-7}$ | 0.557 |

Table 6.13: Results for ν_0 , error $\nu_{0,e}$ and relative error $\nu_{e,rel}$ as well as χ^2/N_f of the extrapolation to zero static magnetic field for different N_0 .

6.5 Fit Results: Extrapolation to Zero Field

| trans. | angle (°) | dist. | b | b_{err} | A | A_{err} |
|----------|-----------|-------|--------|----------------------|-----------------------|----------------------|
| σ | 0 | MB | 0.1387 | $2.23 \cdot 10^{-4}$ | $3.168 \cdot 10^{-2}$ | $5.31 \cdot 10^{-4}$ |
| π | 90 | MB | 0.1368 | $4.32 \cdot 10^{-4}$ | $1.367 \cdot 10^{-2}$ | $4.71 \cdot 10^{-4}$ |
| σ | 45 | MB | 0.14 | $2.18 \cdot 10^{-4}$ | $2.392 \cdot 10^{-2}$ | $5.16 \cdot 10^{-4}$ |
| π | 45 | MB | 0.1374 | $3.7 \cdot 10^{-4}$ | $1.693 \cdot 10^{-2}$ | $4.57 \cdot 10^{-4}$ |

| trans. | angle (°) | dist. | $\nu_i(MHz)$ | $\nu_{i,e}(MHz)$ | s(MHz) | $s_{err}(MHz)$ |
|----------|-----------|-------|--------------|-----------------------|-----------------------|-----------------------|
| σ | 0 | MB | 1 420.407847 | $5.390 \cdot 10^{-5}$ | $6.873 \cdot 10^{-3}$ | $5.375 \cdot 10^{-5}$ |
| π | 90 | MB | 1 421.627403 | $9.053 \cdot 10^{-5}$ | $8.222 \cdot 10^{-3}$ | $1.638 \cdot 10^{-4}$ |
| σ | 45 | MB | 1 420.40785 | $7.425 \cdot 10^{-5}$ | $7.093 \cdot 10^{-3}$ | $7.399 \cdot 10^{-5}$ |
| π | 45 | MB | 1 421.627295 | $1.497 \cdot 10^{-4}$ | $7.310 \cdot 10^{-3}$ | $1.211 \cdot 10^{-4}$ |

| trans. | angle (°) | dist. | f(MHz) | $f_{err}(MHz)$ | χ^2 | χ^2/N_f |
|----------|-----------|-------|-----------------------|-----------------------|----------|--------------|
| σ | 0 | MB | $6.724 \cdot 10^{-3}$ | $1.260 \cdot 10^{-4}$ | 139.48 | 1.761 |
| π | 90 | MB | $1.282 \cdot 10^{-2}$ | $5.147 \cdot 10^{-4}$ | 68.58 | 1.234 |
| σ | 45 | MB | $7.045 \cdot 10^{-3}$ | $1.763 \cdot 10^{-4}$ | 85.79 | 1.381 |
| π | 45 | MB | $1.150 \cdot 10^{-2}$ | $3.892 \cdot 10^{-4}$ | 110.49 | 1.567 |

Table 6.14: Fit parameters with errors for σ_1 and π_1 transition for different angles between static and oscillating magnetic field. A static magnetic field of 8.78×10^{-5} T and $N_0 = 10^5$ was used.

6 Appendix

| trans. | dist. | B(T) | B _{err} (T) | b | b _{err} | | |
|----------|-------|-----------------------|------------------------|-----------------------|------------------------|----------|--------------|
| σ | MB | $8.78 \cdot 10^{-5}$ | $5.36 \cdot 10^{-7}$ | 0.1387 | $2.23 \cdot 10^{-4}$ | | |
| σ | MB | $2.19 \cdot 10^{-4}$ | $1.41 \cdot 10^{-6}$ | 0.1387 | $2.27 \cdot 10^{-4}$ | | |
| σ | MB | $4.39 \cdot 10^{-4}$ | $2.91 \cdot 10^{-6}$ | 0.1382 | $2.24 \cdot 10^{-4}$ | | |
| trans. | dist. | A | A _{err} | ν_{σ} (MHz) | $\nu_{\sigma,e}$ (MHz) | | |
| σ | MB | $3.168 \cdot 10^{-2}$ | $5.31 \cdot 10^{-4}$ | 1420.407847 | $5.390 \cdot 10^{-5}$ | | |
| σ | MB | $3.190 \cdot 10^{-2}$ | $4.76 \cdot 10^{-4}$ | 1420.418926 | $4.861 \cdot 10^{-5}$ | | |
| σ | MB | $3.151 \cdot 10^{-2}$ | $4.86 \cdot 10^{-4}$ | 1420.458442 | $4.843 \cdot 10^{-5}$ | | |
| trans. | dist. | s(MHz) | s _{err} (MHz) | f(MHz) | f _{err} (MHz) | χ^2 | χ^2/N_f |
| σ | MB | $6.873 \cdot 10^{-3}$ | $5.375 \cdot 10^{-5}$ | $6.724 \cdot 10^{-3}$ | $1.260 \cdot 10^{-4}$ | 139.48 | 1.761 |
| σ | MB | $6.967 \cdot 10^{-3}$ | $4.990 \cdot 10^{-5}$ | $6.559 \cdot 10^{-3}$ | $1.217 \cdot 10^{-4}$ | 147.44 | 1.81 |
| σ | MB | $6.922 \cdot 10^{-3}$ | $4.897 \cdot 10^{-5}$ | $6.474 \cdot 10^{-3}$ | $1.215 \cdot 10^{-4}$ | 122.86 | 1.652 |

Table 6.15: Summary of fit parameters and errors for the σ_1 transition using a beam with Maxwell-Boltzmann distributed velocity (50 K), $N_0 = 10^5$.

Bibliography

- [1] P. a. M. Dirac. “The Quantum Theory of the Electron”. In: *Proceedings of the Royal Society A: Mathematical, Physical and Engineering Sciences* 117.778 (Feb. 1928), pp. 610–624. DOI: [10.1098/rspa.1928.0023](https://doi.org/10.1098/rspa.1928.0023). URL: <http://rspa.royalsocietypublishing.org/cgi/doi/10.1098/rspa.1928.0023>.
- [2] P. a. M. Dirac. “The Quantum Theory of the Electron. Part II”. In: *Proceedings of the Royal Society A: Mathematical, Physical and Engineering Sciences* 118.779 (Mar. 1928), pp. 351–361. DOI: [10.1098/rspa.1928.0056](https://doi.org/10.1098/rspa.1928.0056). URL: <http://rspa.royalsocietypublishing.org/cgi/doi/10.1098/rspa.1928.0056>.
- [3] S. G. Karshenboim, F. S. Pavone, and F. Bassini. *The Hydrogen Atom - Precision Physics of Simple Atomic Systems*. Berlin Heidelberg New York: Springer Verlag, 2001.
- [4] G Baur et al. “Production of antihydrogen”. In: *Physics Letters B* 368.3 (Feb. 1996), pp. 251–258. DOI: [10.1016/0370-2693\(96\)00005-6](https://doi.org/10.1016/0370-2693(96)00005-6). URL: <http://www.sciencedirect.com/science/article/pii/0370269396000056><http://linkinghub.elsevier.com/retrieve/pii/0370269396000056>.
- [5] M Amoretti et al. “Production and detection of cold antihydrogen atoms.” In: *Nature* 419.6906 (Oct. 2002), pp. 456–9. DOI: [10.1038/nature01096](https://doi.org/10.1038/nature01096). URL: <http://www.ncbi.nlm.nih.gov/pubmed/12368849>.
- [6] Norman F. Ramsey. *Nobel Lecture: Experiments with separated oscillatory fields and hydrogen masers*. July 1989. DOI: [10.1103/RevModPhys.62.541](https://doi.org/10.1103/RevModPhys.62.541). URL: <http://link.aps.org/doi/10.1103/RevModPhys.62.541>.
- [7] Helmut Hellwig and RFC Vessot. “Measurement of the unperturbed hydrogen hyperfine transition frequency”. In: *IEEE Transactions on Instrumentation and Measurement* 19 (1970), pp. 200–209. URL: http://ieeexplore.ieee.org/xpls/abs_all.jsp?arnumber=4313902.
- [8] R Bluhm. *Probing the Planck scale in low-energy atomic physics*. 2002. arXiv:[0111323v1](https://arxiv.org/abs/0111323v1) [[arXiv:hep-ph](https://arxiv.org/abs/0111323v1)].

- [9] Robert Bluhm, V. Alan Kostelecký, and Neil Russell. *Hydrogen and Antihydrogen Spectroscopy for Studies of CPT and Lorentz Symmetry*. 1998. arXiv:[9810327v1](#) [[arXiv:hep-ph](#)].
- [10] Robert Bluhm, V. Alan Kostelecký, and Neil Russell. *CPT and Lorentz Tests in Hydrogen and Antihydrogen*. 1998. arXiv:[9810269v1](#) [[arXiv:hep-ph](#)].
- [11] A Variola et al. “Towards cold antihydrogen spectroscopy”. In: *Frontier objects in astrophysics and particle physics: Vulcano workshop 2004: conference proceedings*. 2005.
- [12] Norman F. Ramsey. “Experiments with trapped hydrogen atoms and neutrons”. In: *Physica Scripta* 81.1-4 (1995), pp. 97–103. DOI: [10.1007/BF00567253](#). URL: <http://link.springer.com/10.1007/BF00567253><http://iopscience.iop.org/1402-4896/1995/T59/044>.
- [13] B Juhász. *Measurement of the ground-state hyperfine splitting of antihydrogen. talk LEAP 08*. 2008.
- [14] Robert Bluhm. *Low-Energy Tests of Lorentz and CPT Symmetry*. 2003. URL: <http://extras.springer.com/2004/978-3-0348-7907-1/talks/pdf/bluhm.pdf>.
- [15] Neil Russell. *Investigating Lorentz and CPT Symmetry with Antihydrogen*. 2002. arXiv:[0209251v1](#) [[arXiv:hep-ph](#)].
- [16] D Colladay and V. Alan Kostelecký. “Lorentz-violating extension of the standard model”. In: *Physical Review D* 58 (1998), pp. 1–23.
- [17] Asacusa Collaboration. *Atomic spectroscopy and collisions using slow antiprotons*. 2005. URL: <http://collections-r.europarchive.org/cern/20070807182828/http://asacusa.web.cern.ch/asacusa/home/spsc/asacusa2.pdf>.
- [18] Peter J Mohr, Barry N Taylor, and David B Newell. *CODATA Recommended Values of the Fundamental Physical Constants: 2010*. 2012. arXiv:[arXiv:1203.5425v1](#).
- [19] E Widmann et al. *Measurement of the antihydrogen hyperfine structure, Letter of Intent for AD*. 2003, CERN/SPSC 2003–009.

- [20] Svanberg S. *Atomic and Molecular Spectroscopy*. 4th ed. Berlin Heidelberg: Springer Verlag, 2004.
- [21] Walther Gerlach and Otto Stern. “Der experimentelle Nachweis der Richtungsquantelung im Magnetfeld”. In: *Zeitschrift für Physik A Hadrons and Nuclei* (1922), pp. 349–352. URL: <http://www.springerlink.com/index/P72218361287275G.pdf>.
- [22] Kusch P. and Hughes V. W. “Atomic and Molecular Beam Spectroscopy”. In: *Handbuch der Physik XXXVII/1*. Ed. by S. Flügge. Berlin: Springer, 1959, pp. 1–172.
- [23] B. Juhász, E. Widmann, and S. Federmann. “Measurement of the ground-state hyperfine splitting of antihydrogen”. In: *Journal of Physics: Conference Series* 335 (Dec. 2011), p. 012059. DOI: [10.1088/1742-6596/335/1/012059](https://doi.org/10.1088/1742-6596/335/1/012059). URL: <http://stacks.iop.org/1742-6596/335/i=1/a=012059?key=crossref.dcbbea129f4ed00664a295ea9d043ec0>.
- [24] Asacusa Collaboration. *ASACUSA Status Report*. 2014. URL: <http://asacusa.web.cern.ch/ASACUSA/home/spsc/spsc-jan2002.pdf>.
- [25] Y. Enomoto et al. “Synthesis of Cold Antihydrogen in a Cusp Trap”. In: *Physical Review Letters* 105.24 (Dec. 2010), p. 243401. DOI: [10.1103/PhysRevLett.105.243401](https://doi.org/10.1103/PhysRevLett.105.243401). URL: <http://link.aps.org/doi/10.1103/PhysRevLett.105.243401>.
- [26] B. Juhász and E. Widmann. “Planned measurement of the ground-state hyperfine splitting of antihydrogen”. In: *Hyperfine Interactions* 193.1-3 (Aug. 2009), pp. 305–311. DOI: [10.1007/s10751-009-0016-7](https://doi.org/10.1007/s10751-009-0016-7). URL: <http://www.springerlink.com/index/10.1007/s10751-009-0016-7>.
- [27] B. Juhász, E. Widmann, and S. Federmann. “Measurement of the ground-state hyperfine splitting of antihydrogen”. In: *Journal of Physics: Conference Series* 335 (Dec. 2011). DOI: [10.1088/1742-6596/335/1/012059](https://doi.org/10.1088/1742-6596/335/1/012059). URL: <http://stacks.iop.org/1742-6596/335/i=1/a=012059?key=crossref.dcbbea129f4ed00664a295ea9d043ec0>.

- [28] M. Charlton, J. Eades, and D. Horvath. “Antihydrogen physics”. In: *Physical Reports* 241.65 (1994). URL: [#0](http://scholar.google.com/scholar?hl=en&btnG=Search&q=intitle:Antihydrogen+physics).
- [29] C. Malbrunot et al. “Spectroscopy apparatus for the measurement of the hyperfine structure of antihydrogen”. In: *Hyperfine Interactions* (Feb. 2014). DOI: [10.1007/s10751-014-1013-z](https://doi.org/10.1007/s10751-014-1013-z). URL: <http://link.springer.com/10.1007/s10751-014-1013-z>.
- [30] W.R. Leo. *Techniques for Nuclear and Particle Physics Experiments*. Berlin Heidelberg: Springer Verlag, 1987.
- [31] Torsten Fließ bach. *Quantenmechanik, Lehrbuch zur Theoretischen Physik III*. 4th ed. München: Elsevier, 2005.
- [32] B.H. Bransden and C.J. Joachain. *Physics of atoms and molecules*. 2nd ed. London: Pearson Education Limited, 2003.
- [33] Richard Feynman, Robert Leighton, and Matthew Sands. *The Feynman Lectures on Physics - Quantum Mechanics*. New York: Basic Books, 1965.
- [34] Stephen Rand. *Lectures on Light - Nonlinear and Quantum Optics using the Density Matrix*. New York: Oxford University Press Inc., 2010.
- [35] Bruce Shore. *The Theory of Coherent Atomic Excitation, Volume 1: Simple Atoms and Fields*. New York: Wiley Interscience, 1990.
- [36] Rodney Loudon. *The Quantum Theory of Light*. 3rd ed. Oxford: Oxford University Press, 2000.
- [37] Karl Blum. *Density Matrix Theory and Applications*. 3rd ed. Vol. 64. Springer Series on Atomic, Optical, and Plasma Physics. Berlin, Heidelberg: Springer, 2012. DOI: [10.1007/978-3-642-20561-3](https://doi.org/10.1007/978-3-642-20561-3). URL: <http://link.springer.com/10.1007/978-3-642-20561-3>.
- [38] P. A. Valberg and N. F. Ramsey. “Hydrogen-maser measurements of atomic magnetic moments”. In: *Physical Review A* 3.2 (1971), pp. 554–562. URL: http://pra.aps.org/abstract/PRA/v3/i2/p554_1.

- [39] R. Bank, R.L. Graham, and J. Stoer. *Solving Ordinary Differential Equations I*. Vol. 8. Springer Series in Computational Mathematics. Berlin, Heidelberg: Springer, 1993. DOI: [10.1007/978-3-540-78862-1](https://doi.org/10.1007/978-3-540-78862-1).
- [40] William Press et al. *Numerical Recipes - The Art of Scientific Computing*. Third Edit. Cambridge University Press, 2007.
- [41] Kjell Gustafsson. “Control theoretic techniques for stepsize selection in explicit Runge-Kutta methods”. In: *ACM Transactions on Mathematical Software (TOMS)* December (1991), pp. 533–554. URL: <http://dl.acm.org/citation.cfm?id=210242>.
- [42] <http://geant4.cern.ch/>.
- [43] Silke Federmann. “A Spin-Flip Cavity for Microwave Spectroscopy of Antihydrogen”. PhD thesis. University of Vienna, 2012.
- [44] Peter Atkins and Ronald Friedman. *Molecular Quantum Mechanics*. Oxford: Oxford University Press, 2005.
- [45] Claude Cohen-Tannoudji, Jaques Dupont-Roc, and Gilbert Grynberg. *Atom—Photon Interactions*. Weinheim, Germany: Wiley-VCH Verlag GmbH, Apr. 1998. DOI: [10.1002/9783527617197](https://doi.org/10.1002/9783527617197). URL: <http://doi.wiley.com/10.1002/9783527617197>.
- [46] Norman Ramsey. “A Molecular Beam Resonance Method with Separated Oscillating Fields”. In: *Physical Review* 78.6 (June 1950), pp. 695–699. DOI: [10.1103/PhysRev.78.695](https://doi.org/10.1103/PhysRev.78.695). URL: <http://link.aps.org/doi/10.1103/PhysRev.78.695>.
- [47] Ettore Majorana. *Ettore Majorana Scientific Papers*. Ed. by G. F. Basani. Pisa: Springer, 2006.

Danksagung

An dieser Stelle möchte ich mich noch bei allen bedanken, die mich auf dem Weg hierher bei meiner Masterarbeit und meinem Studium begleitet haben und mir zur Seite gestanden sind.

Ich möchte Eberhard danken, dass er mir die Möglichkeit gegeben hat am Stefan-Meyer Institut meine Masterarbeit zu machen - ich habe nicht nur sehr viel gelernt, ich hatte auch sehr viel Spaß dabei.

Mein Dank geht auch an Clemens, mit dem die Zusammenarbeit ein Volksfest war und von dem ich im Zuge meiner Zeit am SMI sehr viel lernen konnte - Danke Clemens, jetzt bin ich bald 'Mistress of Science'.

Auch bei meinen übrigen Kollegen der Antiwasserstoffgruppe und dem Rest des SMIs möchte ich mich bedanken. Ich habe in euch nicht nur wundervolle Kollegen sondern auch Freunde gefunden.

Besonderer Dank geht an meine Mama, von ich gelernt habe hart zu arbeiten und ohne deren Unterstützung ich niemals so weit gekommen wäre. Auch dem Rest meiner Familie möchte ich für ihre Unterstützung danken.

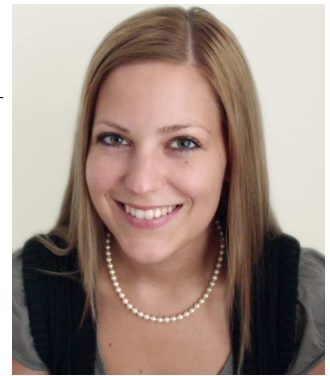
Mein Dank geht auch an meine Studienkollegen, ohne die das Rechnen für diverse Übungen nicht einmal halb so viel Spaß gemacht hätte.

Zu guter Letzt möchte ich mich noch bei meiner besten Freundin Betti und meinem Freund Oli für ihre Unterstützung bedanken.

CURRICULUM VITAE

PERSÖNLICHE ANGABEN

NAME: Bernadette Kolbinger
GEBURTSDATUM UND -ORT: 15. März 1988 | Wien
ADRESSE: Görgengasse 23b/11/15, 1190 Wien
TELEFONNUMMER: 0664 588 9444
EMAIL: bernadette.e.k@gmail.com
FAMILIENSTAND: ledig



AUSBILDUNG

| | |
|-------------------------------|--|
| SEPTEMBER 1994 - JUNI 1998 | Volksschule Volksschule des Instituts Neulandschule Grinzing, Wien |
| SEPTEMBER 1998 - JUNI 2006 | Gymnasium Gymnasium des Instituts Neulandschule Grinzing, Wien |
| OKTOBER 2007 - SEPTEMBER 2011 | Bachelorstudium Physik Bachelorarbeit: <i>Optical Properties of Metal Clusters</i> Betreuer: Prof. Markus Arndt Universität Wien |
| AB OKTOBER 2011 | Masterstudium Physik Universität Wien |
| OKTOBER 2011 - FEBRUAR 2012 | Mitbelegung: Bachelor Scientific Computing Universität Wien |
| FEBRUAR 2013 - JUNI 2014 | Masterarbeit am Stefan Meyer Institut Österreichische Akademie der Wissenschaften |

SPRACHEN

| | |
|-------------|-----------------|
| DEUTSCH | Muttersprache |
| ENGLISCH | Fließend |
| FRANZÖSISCH | Grundkenntnisse |

ZUSATZQUALIFIKATIONEN

| | |
|---------------|--|
| EDV KENTNISSE | Windows, Linux, Mac OS Office Pakete (MS Office, Libre Office), \LaTeX Programmiersprachen C und C++ ROOT, Geant4 |
|---------------|--|